
# A Comparison of Different Approaches to Image Quality Assessment in Phase-Contrast Mammography

***Author:***
**Jesse Reynolds**

***Supervisors:***
**Konstantin Pavlov**
**Timur Gureyev**

*Submitted in partial fulfillment of the requirements for the degree of Master of Science in Medical Physics*

Date: April 5, 2022

# Abstract

**Introduction:** The purpose of medical imaging in breast cancer screening is to detect and characterise pathology. In this context, image quality is best defined in relation to diagnostic performance. However, in many situations, the only practical and economical method to assess image quality is to use clinical image quality assessment performed by radiologists. Clinical image quality assessment can be expensive, time-consuming and suffers from intra and inter-observer variability. Therefore, it is useful to establish a robust, quantitative image assessment method that can accurately predict radiologists' clinical image quality assessment. Unfortunately, the variable anatomical backgrounds in clinical images significantly complicate the relationship between physical and clinical image quality. Two-dimensional digital X-ray mammography (DM) is currently the most commonly utilised screening modality in breast cancer screening. However, it has well-documented limitations. Promising alternatives to two-dimensional DM involving phase-contrast X-ray imaging are currently under investigation. Phase-contrast imaging is an X-ray imaging technique where image contrast is not only related to the X-ray attenuation properties of tissue (as is the case with conventional radiography) but also the refractive properties of the tissue. One technique currently under active research at synchrotron facilities is propagation-based phase-contrast computed tomography (PB-CT). In this work, we take advantage of the relatively simple anatomical background present in synchrotron-based, thin slice PB-CT images of breasts to formulate a simple, robust relative image assessment model.

**Methods:** The experimental data analysed in this study included PB-CT scans, which were obtained for twelve whole, intact mastectomy samples at Imaging and Medical beamline (IMBL) of the Australian Synchrotron. Eleven radiologists assessed overall clinical image quality. Physical image metrics, including contrast, signal to noise ratio, and spatial resolution, were calculated using two different methods for all PB-CT and conventional CT image sets. Weighting factors were applied to each metric, and a scaled contrast to noise (CNR) to spatial resolution (res) score (CNR/res) was calculated.

**Results:** The scaled CNR/res score for each imaging condition, averaged across all samples, was found to correlate significantly with the corresponding radiologist scores with a Pearson r value of approximately 0.96. In addition, the CNR/res score for each imaging condition, for each sample, also correlated significantly with the corresponding radiologist scores with a Spearman r value of approximately 0.89.

**Conclusion:** The scaled CNR/res criterion has been demonstrated as a quantitative image assessment model that effectively predicts the relative clinical image quality, as assessed by radiologists, in the context of PB-CT breast imaging.

# Acknowledgements

I would like to thank my supervisors Dr Konstantin Pavlov and Dr Timur Gureyev for their assistance, contributions and considerable effort proof reading this thesis and the resulting journal article. I would also like to thank Professor Patrick Brennan who provided assistance with this thesis and the journal article.

I would like to thank my wife Rebekah and my children Leah, Theo and Patrick for their support and understanding. Thank you to my parents Susan and Michael and their company Gamma Health Physics who provided valuable advice, proof reading and financial assistance.

The experimental data used in this research was collected on the Imaging and Medical beamline at the Australian Synchrotron, part of ANSTO. The following funding is acknowledged: Project Grant APP1138283 from the National Health and Medical Research Council (NHMRC), Australia. I would also like to acknowledge staff from the University of Melbourne, Monash University, Australian Synchrotron and the University of Sydney for their contribution toward the collection of the original image data and the radiological assessment.

# Contents

**Abstract** iii

**Acknowledgements** iv

**List of Figures** xv

**1 Introduction** 1

1.1 Breast Cancer . . . 1
1.2 Screening Programmes . . . 2
1.3 Screening Technologies . . . 2
1.3.1 Mammography . . . 3
1.3.2 Digital Breast Tomosynthesis . . . 6
1.3.3 Breast Ultrasound . . . 6
1.3.4 Magnetic Resonance Imaging . . . 7
1.3.5 Breast Computed Tomography . . . 7
1.3.6 Other Technologies . . . 8
1.4 X-ray Radiation . . . 9
1.4.1 Electromagnetic Radiation . . . 9
1.4.2 Wave Particle Duality . . . 10
1.4.3 Ionising Radiation . . . 10
1.5 X-ray Production . . . 11
1.5.1 X-ray Tubes . . . 11
1.5.2 Synctrotron Sources . . . 12
1.6 X-ray Propagation in Free Space . . . 13
1.6.1 Spatial and Temporal Coherence . . . 13
1.6.2 Scalar Wave Equation and the Complex Wave Function . . . 13
1.6.3 Coherent Fields . . . 14
1.6.4 Coherent Paraxial Fields . . . 14
1.7 X-ray Interactions with Matter . . . 15
1.7.1 Mechanisms of Attenuation . . . 15
1.7.2 Wave Equations in Matter . . . 18
1.7.3 The Projection Approximation, Attenuation and Refraction . . . 18
1.8 Phase-Contrast Imaging . . . 20
1.8.1 Propagation-Based Phase-Contrast Imaging . . . 21

1.8.2 Bonse-Hart X-ray Interferometry . . . 24
1.8.3 Analyser-Based Phase-Contrast Imaging . . . 26
1.8.4 Grating Interferometry . . . 26
1.8.5 Edge Illumination Methods . . . 30
1.9 X-ray Image Detection . . . 33
1.9.1 Computed Radiography . . . 33
1.9.2 Charge-Coupled Device Detectors . . . 33
1.9.3 Complementary Metal-Oxide Semiconductor Detectors . . . 34
1.9.4 Flat Panel Thin Film Transistor Array Detectors . . . 34
1.9.5 Photon Counting Detectors . . . 35
1.10 Phase Retrieval . . . 35
1.10.1 Transport of Intensity Homogeneous Phase Retrieval . . . 35
1.11 Computed Tomography . . . 37
1.11.1 Filtered Back Projection . . . 38
1.11.2 Iterative Reconstruction . . . 39
1.12 Image Quality Assessment . . . 40
1.12.1 Clinical Image Quality Assessment . . . 41
1.12.2 Physical Image Quality Assessment . . . 41
1.12.3 Relationship Between Physical and Clinical Image Quality . . . 45

**2 Experimental Methods 47**
2.1 Samples and Imaging Technique . . . 47
2.2 Subjective Radiological Assessment . . . 48
2.3 Quantitative Assessment . . . 49
2.3.1 X-TRACT Software . . . 49
2.3.2 3D Slicer Software . . . 52
2.3.3 Formulation of a Predictive Quantitative Image Assessment Metric . 60
2.3.4 Statistical Analysis . . . 62

**3 Results 64**
3.1 Subjective Radiologist Assessment . . . 64
3.2 X-TRACT Results . . . 66
3.3 3D Slicer Results . . . 70
3.4 8-bit Image Pixel Value Analysis . . . 73

**4 Discussion 78**

**5 Conclusion 82**

**Appendix A Additional Results 83**
A.1 Subjective Radiologist Assessment . . . 83
A.2 Additional X-TRACT Results . . . 83
A.2.1 X-TRACT Plots for Individual Samples . . . 85
A.3 Additional 3D Slicer Results . . . 93

**Appendix B Journal Article** **101**

**Appendix C 3D Slicer Code** **117**

C.1 "Perceived" Spatial Resolution Code . . . . . 117

C.2 "Absolute" Spatial Resolution Code . . . . . 126

# List of Figures


1.1 The Electromagnetic Spectrum [12] . . . . . 9

1.2 A diagram of an electromagnetic wave propagating at velocity, $c$ in the $x$ direction. The electric field oscillates in the $xy$ plane, and the magnetic field oscillates in the $xz$ plane [47]. . . . . 10

1.3 Graph of the Rayleigh, Compton, photoelectric, pair production and total mass attenuation coefficients for carbon as a function of photon energy [58] 17

1.4 X-ray wave field travelling from the entrance surface, through an object, to the exit surface under the projection approximation [48] . . . . . 18

1.5 Calculated differences between the real and imaginary components of the complex refractive index between glandular tissue and adipose tissue. Data sourced from [60] . . . . . 21

1.6 Geometric-optics ray based diagram showing the evolution of intensity modulations due to phase differences through free space propagation [64] . . . . 22

1.7 Wave based diagram showing the evolution of intensity modulations due to phase differences through free space propagation [63] . . . . . 22

1.8 Simulated PBPCI images of a solid carbon sphere of 0.5 mm diameter. The source to object distance is fixed at 10 cm, while the object to detector distance, $R_2$, increases from left to right. The left most image is a contact, absorption based image at $R_2 = 0$. The remaining images, from left to right have propagation distances of $R_2 = 10\,cm$, $50\,cm$ and $100\,cm$ respectively. Image adapted from [65] . . . . . 23

1.9 Crystal Interferometer Setup. [57] . . . . . 25

1.10 ABPCI setup. The rocking curve represents the reflection intensity of the main beam versus crystal angle, the peak of the curve corresponds to the Bragg angle, $\theta_B$, [75] . . . . . 27

1.11 ABPCI Images of a mouse: (a) absorption based image, (b) refraction image, (c) scattering dark field image [78] . . . . . 27

1.12 Interference pattern following X-ray diffraction due to an absorption grating (top) and phase grating (bottom) [57]. . . . . 28

1.13 Grating based interferometry setup for a synchrotron X-ray source. A grating, "Grating 0" can be added for a laboratory X-ray source such as an X-ray tube [57]. . . . . 30

1.14 The principle of phase stepping. Images of polystyrene spheres (100 and 200 $\mu$m) acquired at different positions $x_g = x_1, ..., x_4$ of the absorption grating (a-d). (e) Phase stepping curve showing intensity oscillation in two different detector pixels $i$=1,2, as a function of $x_g$. Note that due to the position of pixel 1 outside the sample, the corresponding curve (shown in solid black) is equivalent to having no sample in the interferometer. For each pixel, the oscillation phase, $\phi$, and average intensity, $a$, can be determined. (f) Image of the oscillation phase, $\phi$, for all pixels. (g) Wave front phase, $\Phi$, retrieved from $\phi$ by integration. (h) Image of the average intensity $a$ for all pixels, equivalent to a non-interferometric image. The length of the scale bar is 50 $\mu$m [80] . . . . . 31

1.15 (a) Edge illumination setup, (b) illumination function (c) laboratory X-ray source implementation [75] . . . . . 32

1.16 Propagation based phase-contrast imaging setup using a point source (not to scale). Adapted from [87] . . . . . 36

1.17 A specific projection angle (a) results in a 1D intensity image (b) which corresponds to one column in Radon space (sinogram) (c). Adapted from [12] . . . . . 38

1.18 Simple back projection reconstruction. A specific projection (a) results in a 1D intensity image (b) which is back projected across the object area at the angle of the projection (c) The sum of many back projections results in a blurred slice image (d) [12]. . . . . 39

1.19 Different filters applied during filtered back projection reconstruction. . . . 40

1.20 A plot of the MTF of an imaging system. Sinusoidal input signals are incident on the detector. The input signal with a spatial frequency of 1 cycle per millimetre (cy/mm) has diminished its input contrast to 87% by resolution losses in the imaging system. The input signals with spatial frequencies of 2 and 4 cy/mm have likewise been diminished to 56% and 13% of their input contrast, respectively. [15]. . . . . 44

1.21 The spread functions in the spatial domain are shown. [15]. . . . . 44

2.1 An example of the placement of the thick line tool in X-TRACT to measure the contrast between glandular and adipose tissue, the SNR and the spatial resolution in the image. The red/white rectangle indicates the shape of the thick line tool rectangle and the yellow square indicates the approximate location of the virtual square (not usually shown in X-TRACT). . . . . 50

2.2 An example of the measurements performed on one PB-CT slice stack for patient number 2370691 which used an X-ray energy of 32 keV, a MGD of 2 mGy and full TIE phase retrieval. Using the "Thick line" tool, a measurement is performed on every tenth slice of both the axial and sagittal reconstructions. The bottom line shows the final values for each metric averaged across all measurements of both projections. The cells shaded with yellow indicate values which are recorded from the X-TRACT Image Control dialogue, while grey cells are values that are calculated in Microsoft Excel from the values shaded in yellow. . . . . 52

2.3 A magnified area of an AB-CT reference image. The green painted segment represents glandular tissue, and the yellow painted segment represents the background adipose tissue. Similar segments were painted on every 10th image of the CT image set. . . . . 54

2.4 Comparison of a 32 keV, 4 mGy, hTIE PB-CT image (right) and the equivalent reference AB-CT image (left). The glandular/adipose interface of the PB-CT image (right) appears sharper than the equivalent AB-CT reference image (left). The X-TRACT method gives a spatial resolution ratio (PB-CT/AB-CT) of 1.02, and the "absolute" spatial resolution method (implemented in 3D Slicer) gives a ratio of 1.05, both indicating almost equivalent spatial resolution between the PB-CT and AB-CT images. The "perceived" spatial resolution method (implemented in 3D Slicer) gives a ratio of 1.80, indicating the PB-CT image has significantly sharper edges relative to the AB-CT image. This demonstrates that the "perceived" spatial resolution method potentially correlates more accurately with how the image appears to a human observer in the context of PB-CT images. . . . . 57

2.5 Segmented glandular tissue (in green) on an isolated slice image prior to calculating the "absolute" spatial resolution. . . . . 57

2.6 Ring segments resulting from the first (green), fourth (yellow) and eighth (red) iteration of the "absolute" spatial resolution measurement method. . . 58

2.7 Ring segments resulting from the first (green), eighth (yellow) and sixteenth (red) iteration of the "perceived" spatial resolution measurement method. . 58

2.8 Plots of MPV vs iteration number (left) and the derivative of the edge profile with fitted Gaussian Curve (right). . . . . 59

3.1 Plot of radiologist scores (in blue) for each imaging condition averaged across all radiologists and samples (scores shown in Table 3.4), with error bars of ± one standard deviation (also shown in Table 3.4). The radiologist score is compared to various un-scaled quantitative scores measured using X-TRACT including; CNR/res (yellow), contrast (red), SNR (grey) and spatial resolution (green). These results are tabulated in Table A.3 . . . . . 66

3.2 Plot of subjective radiologist scores (in blue) for each imaging condition averaged across all radiologists and samples (scores shown in Table 3.4), with error bars of ± one standard deviation (also shown in Table 3.4). The subjective radiologist score is compared to various scaled quantitative scores measured using X-TRACT including; CNR/res (yellow), contrast (red), SNR (grey) and spatial resolution (green). . . . . 68

3.3 Plot of subjective radiologist scores (in blue) for each imaging condition averaged across all radiologists and samples (scores shown in Table 3.4), with error bars of ± one standard deviation (also shown in Table 3.4). The subjective radiologist score is compared to various scaled and offset quantitative scores measured using X-TRACT including; CNR/res (yellow), contrast or contrast (red), SNR (grey) and spatial resolution (green). The CNR/res scores have had an offset factor of 0.55 added to all values so that the height of the plot closely matches the radiologist scores. . . . . 69

3.4 Plot of radiologist scores (in blue) for each imaging condition averaged across all radiologists and samples (scores shown in Table 3.4), with error bars of ± one standard deviation (also shown in Table 3.4). The radiologist score is compared to various un-scaled quantitative scores measured using 3D Slicer including; CNR/res (perc) (yellow), contrast (red), SNR (grey), "absolute" spatial resolution (green dotted) and "perceived" spatial resolution (green dashed). These results are tabulated in Table A.8. The CNR/res (perc) score shown in yellow was calculated using the "perceived" spatial resolution ratio in Equation 2.3. . . . . 70

3.5 Plot of subjective radiologist scores (in blue) for each imaging condition averaged across all radiologists and samples (scores shown in Table 3.4), with error bars of ± one standard deviation (also shown in Table 3.4). The subjective radiologist score is compared to various scaled quantitative scores measured using 3D Slicer including; CNR/res (yellow), contrast (red), SNR (grey) and spatial resolution (green). . . . . 72

3.6 Comparison of the MPVs within glandular and adipose regions between a 32keV-2mGy-hTIE 8-bit image (left) and a 32keV-4mGy-hTIE 8-bit image (right) of sample 4247239. Considerable variations between MPVs were found between the images. . . . . 74

3.7 Comparison of the MPVs within glandular and adipose regions between a 32keV-2mGy-hTIE 32-bit image (left) and a 32keV-4mGy-hTIE 32-bit image (right) of sample 4247239. No considerable differences between MPVs were found between the images. . . . . 75

3.8 Microsoft Excel spreadsheet showing X-ray energy dependent 32-bit windows which are used to convert greyscale images from 32-bit to 8-bit greyscale. The windows are chosen so that the average of the MPVs in the glandular and adipose regions is maintained between the resultant 8-bit 32 keV and 34 keV images (at a pixel value of 146.4). The conversion windows are additionally chosen such that the ratio of the glandular/adipose contrast (or visibility) between the original 32-bit 32 keV image and 32-bit 34keV images (of 1.072) is maintained throughout the conversion. This is intended to ensure that any contrast differences between the 8-bit 32 keV and 34 keV images are due to physical differences between X-ray energies rather than inconsistent image display. . . . . 76

3.9 8-bit DICOM images converted from original 32-bit images using the proposed window for a 32 keV image which is shown in Figure 3.8. The 32keV-2mGy-hTIE image is shown on the left and the 32keV-4mGy-hTIE image is shown on the right. The MPVs in the glandular and adipose regions remain relatively constant between the two images. . . . . 77

A.1 Plot of subjective radiologist scores (in blue) for each imaging condition for sample 2370691 (shown in Table 3.2), with error bars of ± one standard deviation (shown in Table A.1). The subjective radiologist score is compared to various scaled quantitative scores measured using X-TRACT including; CNR/res (yellow), contrast (red), SNR (grey) and spatial resolution (green) for sample 2370691. . . . . 85

A.2 Plot of subjective radiologist scores (in blue) for each imaging condition for sample 4247239 (shown in Table 3.2), with error bars of ± one standard deviation (shown in Table A.1). The subjective radiologist score is compared to various scaled quantitative scores measured using X-TRACT including; CNR/res (yellow), contrast (red), SNR (grey) and spatial resolution (green) for sample 4247239. . . . . 86

A.3 Plot of subjective radiologist scores (in blue) for each imaging condition for sample 4638975 (shown in Table 3.2), with error bars of ± one standard deviation (shown in Table A.1). The subjective radiologist score is compared to various scaled quantitative scores measured using X-TRACT including; CNR/res (yellow), contrast (red), SNR (grey) and spatial resolution (green) for sample 4638975. . . . . 86

A.4 Plot of subjective radiologist scores (in blue) for each imaging condition for sample 4704628 (shown in Table 3.2), with error bars of ± one standard deviation (shown in Table A.1). The subjective radiologist score is compared to various scaled quantitative scores measured using X-TRACT including; CNR/res (yellow), contrast (red), SNR (grey) and spatial resolution (green) for sample 4704628. . . . . 87

A.5 Plot of subjective radiologist scores (in blue) for each imaging condition for sample 7096050L (shown in Table 3.2), with error bars of ± one standard deviation (shown in Table A.1). The subjective radiologist score is compared to various scaled quantitative scores measured using X-TRACT including; CNR/res (yellow), contrast (red), SNR (grey) and spatial resolution (green) for sample 7096050L. . . . . 88

A.6 Plot of subjective radiologist scores (in blue) for each imaging condition for sample 7096050R (shown in Table 3.2), with error bars of ± one standard deviation (shown in Table A.1). The subjective radiologist score is compared to various scaled quantitative scores measured using X-TRACT including; CNR/res (yellow), contrast (red), SNR (grey) and spatial resolution (green) for sample 7096050R. . . . . 88

A.7 Plot of subjective radiologist scores (in blue) for each imaging condition for sample 7104092 (shown in Table 3.2), with error bars of ± one standard deviation (shown in Table A.1). The subjective radiologist score is compared to various scaled quantitative scores measured using X-TRACT including; CNR/res (yellow), contrast (red), SNR (grey) and spatial resolution (green) for sample 7104092. . . . . 89

A.8 Plot of subjective radiologist scores (in blue) for each imaging condition for sample 7949430 (shown in Table 3.2), with error bars of ± one standard deviation (shown in Table A.1). The subjective radiologist score is compared to various scaled quantitative scores measured using X-TRACT including; CNR/res (yellow), contrast (red), SNR (grey) and spatial resolution (green) for sample 7949430. . . . . 89

A.9 Plot of subjective radiologist scores (in blue) for each imaging condition for sample 8283541L (shown in Table 3.2), with error bars of ± one standard deviation (shown in Table A.1). The subjective radiologist score is compared to various scaled quantitative scores measured using X-TRACT including; CNR/res (yellow), contrast (red), SNR (grey) and spatial resolution (green) for sample 8283541L. . . . . 90

A.10 Plot of subjective radiologist scores (in blue) for each imaging condition for sample 8283541R (shown in Table 3.2), with error bars of ± one standard deviation (shown in Table A.1). The subjective radiologist score is compared to various scaled quantitative scores measured using X-TRACT including; CNR/res (yellow), contrast (red), SNR (grey) and spatial resolution (green) for sample 8283541R. . . . . 90

A.11 Plot of subjective radiologist scores (in blue) for each imaging condition for sample 8413420 (shown in Table 3.2), with error bars of ± one standard deviation (shown in Table A.1). The subjective radiologist score is compared to various scaled quantitative scores measured using X-TRACT including; CNR/res (yellow), contrast (red), SNR (grey) and spatial resolution (green) for sample 8413420. . . . . 91

A.12 Plot of subjective radiologist scores (in blue) for each imaging condition for sample 8423990 (shown in Table 3.2), with error bars of ± one standard deviation (shown in Table A.1). The subjective radiologist score is compared to various scaled quantitative scores measured using X-TRACT including; CNR/res (yellow), contrast (red), SNR (grey) and spatial resolution (green) for sample 8423990. . . . . 91

A.13 Plot of subjective radiologist scores (in blue) for each imaging condition for sample 2370691 (shown in Table 3.2), with error bars of ± one standard deviation (shown in Table A.1). The subjective radiologist score is compared to various scaled quantitative scores measured using 3D Slicer including; CNR/res (yellow), contrast (red), SNR (grey) and spatial resolution (green) for sample 2370691. . . . . 94

A.14 Plot of subjective radiologist scores (in blue) for each imaging condition for sample 4247239 (shown in Table 3.2), with error bars of ± one standard deviation (shown in Table A.1). The subjective radiologist score is compared to various scaled quantitative scores measured using 3D Slicer including; CNR/res (yellow), contrast (red), SNR (grey) and spatial resolution (green) for sample 4247239. . . . . 94

A.15 Plot of subjective radiologist scores (in blue) for each imaging condition for sample 4638975 (shown in Table 3.2), with error bars of ± one standard deviation (shown in Table A.1). The subjective radiologist score is compared to various scaled quantitative scores measured using 3D Slicer including; CNR/res (yellow), contrast (red), SNR (grey) and spatial resolution (green) for sample 4638975. . . . . 95

A.16 Plot of subjective radiologist scores (in blue) for each imaging condition for sample 4704628 (shown in Table 3.2), with error bars of ± one standard deviation (shown in Table A.1). The subjective radiologist score is compared to various scaled quantitative scores measured using 3D Slicer including; CNR/res (yellow), contrast (red), SNR (grey) and spatial resolution (green) for sample 4704628. . . . . 95

A.17 Plot of subjective radiologist scores (in blue) for each imaging condition for sample 7096050L (shown in Table 3.2), with error bars of ± one standard deviation (shown in Table A.1). The subjective radiologist score is compared to various scaled quantitative scores measured using 3D Slicer including; CNR/res (yellow), contrast (red), SNR (grey) and spatial resolution (green) for sample 7096050L. . . . . 96

A.18 Plot of subjective radiologist scores (in blue) for each imaging condition for sample 7096050R (shown in Table 3.2), with error bars of ± one standard deviation (shown in Table A.1). The subjective radiologist score is compared to various scaled quantitative scores measured using 3D Slicer including; CNR/res (yellow), contrast (red), SNR (grey) and spatial resolution (green) for sample 7096050R. . . . . 96

A.19 Plot of subjective radiologist scores (in blue) for each imaging condition for sample 7104092 (shown in Table 3.3), with error bars of ± one standard deviation (shown in Table A.2). The subjective radiologist score is compared to various scaled quantitative scores measured using 3D Slicer including; CNR/res (yellow), contrast (red), SNR (grey) and spatial resolution (green) for sample 7104092. . . . . 97
A.20 Plot of subjective radiologist scores (in blue) for each imaging condition for sample 7949430 (shown in Table 3.3), with error bars of ± one standard deviation (shown in Table A.2). The subjective radiologist score is compared to various scaled quantitative scores measured using 3D Slicer including; CNR/res (yellow), contrast (red), SNR (grey) and spatial resolution (green) for sample 7949430. . . . . 97
A.21 Plot of subjective radiologist scores (in blue) for each imaging condition for sample 8283541L (shown in Table 3.3), with error bars of ± one standard deviation (shown in Table A.2). The subjective radiologist score is compared to various scaled quantitative scores measured using 3D Slicer including; CNR/res (yellow), contrast (red), SNR (grey) and spatial resolution (green) for sample 8283541L. . . . . 98
A.22 Plot of subjective radiologist scores (in blue) for each imaging condition for sample 8283541R (shown in Table 3.3), with error bars of ± one standard deviation (shown in Table A.2). The subjective radiologist score is compared to various scaled quantitative scores measured using 3D Slicer including; CNR/res (yellow), contrast (red), SNR (grey) and spatial resolution (green) for sample 8283541R. . . . . 98
A.23 Plot of subjective radiologist scores (in blue) for each imaging condition for sample 8413420 (shown in Table 3.3), with error bars of ± one standard deviation (shown in Table A.2). The subjective radiologist score is compared to various scaled quantitative scores measured using 3D Slicer including; CNR/res (yellow), contrast (red), SNR (grey) and spatial resolution (green) for sample 8413420. . . . . 99
A.24 Plot of subjective radiologist scores (in blue) for each imaging condition for sample 8423990 (shown in Table 3.3), with error bars of ± one standard deviation (shown in Table A.2). The subjective radiologist score is compared to various scaled quantitative scores measured using 3D Slicer including; CNR/res (yellow), contrast (red), SNR (grey) and spatial resolution (green) for sample 8423990. . . . . 99

# Chapter 1

# Introduction

## 1.1 Breast Cancer

Breast cancer is a disease whereby abnormal cells in breast tissue begin to grow in an uncontrolled manner. The cancer typically begins as a pre-invasive cancer known as carcinoma in-situ. There are two types of carcinoma in-situ: Ductal Carcinoma In Situ (DCIS) and Lobular Carcinoma In Situ (LCIS) [1]. Carcinoma in-situ may progress into an invasive carcinoma by spreading into the surrounding breast tissue. Progression into an invasive carcinoma, however, cannot be predicted. An invasive carcinoma may progress further by invading blood or lymph vessels and metastasising (spreading) into other sites in the body. If this occurs there is an increased chance of patient mortality. Upon diagnosis, breast cancer is assigned a Tumour, Node, Metastasis (TNM) stage which indicates the size of the tumour and how far it has progressed. The TNM staging system comprises five stages numbered 0 to 4, where Stage 0 indicates carcinoma in-situ and Stage 4 indicates the presence of invasive carcinoma which has spread to other parts of the body [2]. Risk factors for breast cancer include having a family history of breast cancer, having never borne a child or bearing a child after age 35, previous cancer in one breast, exposure to ionising radiation, excessive alcohol intake, obesity, smoking or possessing the BRCA1 or BRCA2 gene [3]. Breast cancer is rare in women under 30 but the incidence rises rapidly following menopause. Male breast cancer can also occur but is rare.

A range of options are available for the treatment of breast cancer. A treatment plan typically involves multiple methods and is patient specific. Treatment options for breast cancer include local treatments such as surgery and radiotherapy, and systemic treatments such as chemotherapy and hormone therapy. Surgical treatment, or lumpectomy, involves removal of the tumour, including a margin of healthy tissue. In more severe cases, the entire breast is removed in a procedure called a mastectomy. Following surgery, it is usual for patients to undergo additional treatment to eliminate residual cancer cells in breast tissue including any cancer cells which may have metastasised into the lymph nodes or other regions of the body. Radiotherapy utilises various types of radiation to destroy cancer cells in the breast tissue and surrounding lymph nodes. Chemotherapy involves administration of drugs, either intravenously or orally, and is used to destroy cancer cells which may have

metastasised throughout the body. Hormone therapy may be used if the cancer cells are hormone receptor positive in order to lower the risk of breast cancer recurrence [2] [4].

In 2020 breast cancer surpassed lung cancer as the most commonly diagnosed cancer across both sexes with an estimated 2.3 million new cases worldwide [5]. Breast cancer accounts for 1 in 4 cancer diagnoses and 1 in 6 cancer deaths amongst the female population worldwide [5]. A population-based study in six OECD countries between 2000 and 2007 found that women who were first diagnosed with TNM Stage 1 breast cancer had an age-standardised net survival of 99.4% after 3 years (averaged across 5 countries), while women first diagnosed with stage 4 breast cancer had an age-standardised net survival of 35% after 3 years (averaged across 5 countries) [6]. These statistics clearly demonstrate the importance of early diagnosis in reducing mortality rates of women with breast cancer.

## 1.2 Screening Programmes

Due to the importance of early detection of breast cancer, breast screening programmes were introduced to reduce the morbidity and mortality from breast cancer within the female population [7]. Breast screening involves assessing the breasts for cancer of asymptomatic women using attenuation-based X-ray techniques. The aim of the programmes is the early detection of breast cancer when treatment is most effective at preventing mortality [8].

Breast screening programmes were established in many countries following a series of trials in the 1980s which demonstrated that mammography-based screening programmes reduced breast cancer mortality by 25-30% [9]. Screening programmes target women who are most at risk of developing breast cancer, as exposure to ionising radiation introduces a small additional risk to the general population. The programmes include older women, as well as younger women who are assessed as having an increased risk of developing breast cancer. The New Zealand screening programme, BreastScreen Aotearoa (BSA), provides a free screening service every two years to women aged between 45 and 69 years [10].

## 1.3 Screening Technologies

Several X-ray-based technologies have been incorporated into screening programmes over the years. These include screen-film mammography, digital mammography (including computed radiography) and digital tomosynthesis mammography. Non-X-ray-based techniques such as ultrasound, magnetic resonance imaging (MRI), positron emission tomography (PET), thermography and clinical breast examinations have also been investigated. Some of these techniques have been adopted into screening programmes [11].

### 1.3.1 Mammography

Mammography is an X-ray procedure which is optimised for imaging breast tissue and is designed to detect breast pathology, particularly breast cancer. A mammogram image is formed by projecting X-rays, which are produced in a specialised mammography X-ray tube, through a compressed breast. X-rays that are not absorbed by the compressed breast pass into a detector to form an attenuation-based image. Mammography is used for both screening of asymptomatic women (screening mammography) and for the diagnosis of symptomatic women (diagnostic mammography). When used for screening, two views of each breast are acquired. These views include a Craniocaudal (CC) image and a Mediolateral Oblique (MLO) image [11]. The use of two views increases the sensitivity of the screening test by providing a more complete image of the breast tissue than could be acquired with a single image. In diagnostic imaging, a larger range of views is acquired. This range includes spot compression views, magnification views, stereotactic biopsy views and several views at different angles around the breast [12]. There are four major indicators which radiologists utilise to diagnose breast cancer. These include microcalcifications, which are clusters of small calcium specks, the characteristic morphology of a tumour mass, architectural distortions of usual tissue patterns and asymmetry between corresponding regions of the left and right breast [12]. These indicators are often difficult to visualise on a mammogram. Mammogram image quality, therefore, must be optimised to ensure pathology is detected early and accurately. Excellent image quality must also be balanced with the need to reduce radiation dose to the patient, especially considering the high sensitivity of breast glandular tissue to radiation [13] [14].

Compared to standard X-ray machines, mammography machines have several unique features which are designed to optimise breast image quality. Attenuation differences between normal and cancerous tissue are subtle, necessitating the use of low energy X-rays to maximise differential attenuation between tissue types in the breast. X-ray tubes with molybdenum, rhodium or tungsten anodes with a range of filters are used with tube voltages below 40 kVp to provide a low energy X-ray spectrum. The output spectrum is typically dominated by the characteristic rays of the anode which are 17.5 and 19.6 keV for molybdenum and 20.2 and 22.7 keV for rhodium [15]. These energies are favourably placed for mammography. The use of a low energy X-ray spectrum to enhance contrast will result in increased skin and glandular dose to the breast. This balance must be optimised. In order to provide the necessary spatial resolution to visualise small features, the focal spot of the X-ray tube is small, between 0.1 mm and 0.3 mm. A small focal spot necessitates using lower tube currents in order to avoid overheating the anode material. Lower tube currents require longer exposure times to produce an optimal image, thus risking motion blur. At the mammographic X-ray energy range, 37-50% of the total radiation incident on the image receptor is scattered radiation. Thus, the scatter-to-primary radiation ratio (SPR) ranges from 0.3 to 1.2, depending on breast thickness [12]. The use of grids with ratios (height/opening width) between 3.5:1 to 5:1 results in reduced scatter and improved SPRs. These grids reduce image noise and improve contrast [12].

Mammography machines utilise compression paddles which compress the breast tissue to a uniform thickness across the image receptor. Compression offers several advantages: minimised superposition of tissues, reduced SPRs at the detector, a reduction in geometric unsharpness, a reduction in overall attenuation, and hence dose to the breast, a reduction in the exposure range requirements of the detector and a reduction in motion blur due to patient movement. A significant disadvantage of compression is the resulting discomfort experienced by many women. This discomfort may contribute to an unwillingness to undergo mammography-based screening [16]. Automatic Exposure Control (AEC) is used in mammography to select the correct exposure to achieve an optimised optical density (OD) if a screen-film system is used, or a specified Signal to Noise Ratio (SNR) if a digital system is used [15].

### Screen-Film Mammography

Screen-film mammography uses single emulsion radiographic film coupled with an intensifying screen as the detector. The film is contained within lightproof cassettes which are available in 18cm x 24cm and 24cm x 30cm formats. A single high definition phosphor screen is positioned in contact with the emulsion side of the film within the cassette. A proportion of the X-rays that have passed through the compressed breast are absorbed by the phosphor screen and converted into visible light. The visible light emission from the screen requires an appropriate visible light sensitive film emulsion. A latent image is formed within the film emulsion which is then chemically processed to produce the final visible image. The OD of the film is related to the X-ray exposure by a sigmoid-shaped characteristic curve [15]. For example, microcalcifications are more attenuating than fat or glandular tissue. Microcalcifications therefore appear white in the image on a film. Mammography film has a characteristic curve with a high gradient that is designed to enhance the contrast between tissues with small differences in attenuation. However, the film has a concomitant narrow exposure latitude. The narrow exposure latitude results in some regions of the breast being under-or-over exposed resulting in lower contrast in those regions. The narrow exposure latitude also requires exposures to be precisely controlled, necessitating the use of AEC systems. While screen-film mammography provides excellent spatial resolution, it also suffers from several limitations. The narrow exposure latitude imposes strict requirements on exposure control, resulting in a higher incidence of retakes. Tumours may also be missed if they lie in areas of the breast which are under-or-over exposed. Screen-film systems also inherently require compromise between spatial resolution and quantum detection efficiency. Screen film systems can provide limiting spatial resolutions greater than 15 line pairs per millimeter [17]. The quantum detection efficiency measures the percentage of incident X-rays which are absorbed by the detector material [18]. For standard resolution screen-film systems used in mammography, the quantum detection efficiency is approximately 50-70% [18]. Hendrick *et al.* [19] found the average glandular dose for a standard screening examination with two views to each breast was

4.7mGy across 33 screening sites using screen-film systems.

### Digital Mammography

Digital mammography systems can be grouped into either Computed Radiography (CR) or Digital Radiography (DR) systems. Technical details of these digital acquisition methods are provided in Section 1.9. CR has inferior spatial resolution and lower SNRs for the same dose when compared to DR [20] and poorer cancer detection rates in screening programmes [21]. DR has several advantages compared to screen-film and CR mammography, resulting in the New Zealand National Screening Unit's breast screening programme (BreastScreen Aotearoa) exclusively using DR since 2014 [22]. DR allows the acquisition, processing, display and storage to be performed separately. As a result, each process can be optimised, leading to improved detection of DCIS and invasive carcinoma when compared to previous systems [23]. Other advantages of DR include improved exposure latitude, lower radiation doses, increased productivity due to fast acquisition and technologist evaluation, reduced patient waiting time and overall superior image quality. A disadvantage of digital systems is that the limiting spatial resolution is lower than screen-film systems because of the limitation imposed by the pixel size of the detector. The limiting spatial resolution based on pixel size is known as the Nyquist limit and is typically 5 line pairs per millimeter or greater [17]. There were initial concerns that the spatial resolution of digital systems would limit microcalcification detection [24]. Subsequent studies, however, have shown that digital mammography indicates improved image quality with higher reliability in characterising calcifications compared with screen-film mammography [17] [25]. Amorphous selenium digital detector systems can achieve greater than 95% quantum detection efficiency in the mammography X-ray energy range [18]. The increased quantum detection efficiency, detective quantum efficiency (DQE) and dynamic range of digital systems leads to lower radiation doses compared to screen-film systems [26]. Hendrick *et al.* [19] found the average glandular dose for a standard screening examination with two views of each breast was 3.7mGy across 33 screening sites using digital mammography systems: a 22% reduction in dose compared to screen-film systems.

Standard two-view mammography remains the most widely implemented screening technology. There is sufficient evidence for reduced mortality from breast cancer when used for screening women aged 50-69 years, as assessed by the International Agency for Research on Cancer [11]. Mammography is a relatively low-cost modality with adequate sensitivity to detect breast cancer at an early stage and with low radiation dose to the patient. Mammography screening, however, is not without risk. The risks are: false negative results, false positive results, over-diagnosis and ionising radiation exposure [27]. The most serious outcome from a mammogram is a false negative result: a patient has undetected breast cancer, resulting in delayed diagnosis and treatment. A false positive occurs when a cancer is indicated, which upon further investigation is not present. False positive results create unnecessary anxiety, extra cost and wasted time for the patient.

Half of all women over 50 enrolling in a screening program will experience a false positive in the following 10 year period [27]. Over-diagnosis is the diagnosis of a cancer which would not have adversely affected the patient if left alone. Over-diagnosis is likely to cause significant anxiety, risk of morbidity, extra cost and wasted time for the patient compared to a false positive. Some studies estimate that 1 in 5 cancers are over-diagnosed leading to unnecessary treatment [28]. The breast is one of the most radio-sensitive organs in the body [13] and a mammogram carries a very small chance of causing a radiation induced cancer. A major limitation of conventional projection mammography is that the three-dimensional volume of a breast is projected onto a two-dimensional image. This results in the superposition of breast tissues, leading to reduced conspicuity of lesions, and reduced sensitivity (probability of finding cancers which are present) [11]. Tissue superposition can also lead to a lesion being detected which does not exist, thus reducing specificity (probability of a negative result when cancer is not present) [11]. These effects are particularly challenging when reading the mammograms of women with dense breasts where there is a large portion of glandular tissue.

### 1.3.2 Digital Breast Tomosynthesis

Digital breast tomosynthesis (DBT) aims to overcome the problem of anatomical noise which arises from the superposition of tissues occurring during standard mammography acquisitions. DBT is a technique which produces a series of tomogram (in focus plane) images at given depths in the breast [15]. These tomogram images are reconstructed from a series of low dose projection images taken through a limited range of angles around the breast. DBT has been incorporated into several modern general mammography machines and, in some cases, is retro-fitted to older mammography machines. DBT is associated with increased radiation dose compared to standard digital mammography, where the average increase of DBT dose is 38% [29]. DBT is associated with an estimated 17% increase in sensitivity when compared to standard digital mammography [30]. Studies also suggest a likely improvement in specificity, but the level of improvement varies between studies [30]. While DBT is useful in diagnostic mammography, there is no clear consensus as to whether it is a cost-effective alternative to standard digital mammography for screening purposes. The main limitations preventing screening use include increased radiation dose, increased equipment costs and increased reading time required by radiologists [11].

### 1.3.3 Breast Ultrasound

Ultrasound systems utilise sound waves which propagate through the breast and reflect off tissue interfaces to form a tomographic grey-scale image. The generation of sound pulses and the detection of echoes is performed using a transducer, which is typically hand held and manipulated by a sonographer. The advantages of breast ultrasound compared to mammography are: no ionising radiation, no discomfort for the patient and superior ability to detect mammographically occult breast cancers in women with dense breasts [11] [31]. The disadvantages are: low spatial resolution leading to an inability to detect

microcalcifications, low contrast, low specificity, high biopsy rates with low cancer-to-biopsy yield, strong dependency on skills of the sonographer and slow acquisition times [32]. Due to the significant disadvantages of ultrasound, the National Screening Unit of New Zealand does not support the use of ultrasound as a primary or adjunct screening tool in the BSA screening programme [33]. Ultrasound is, however, widely used in breast clinics in New Zealand as an investigatory tool to characterise areas of interest seen on a mammogram or to guide biopsy needles to areas of interest. Ultrasound is useful for differentiating between solid and cystic masses, particularly in dense breasts [32].

### 1.3.4 Magnetic Resonance Imaging

Breast MRI utilises radio waves, strong magnetic fields and magnetic gradients to create detailed tomographic images of breast tissue. This technique is currently used to reliably detect breast malignancy [11]. Contrast-enhanced MRI involves imaging the breast with dedicated breast coils before and after intravenous administration of a contrast agent; commonly gadolinium chelates. Advantages of breast MRI include high sensitivity without the use of ionising radiation [11]. The disadvantages are: low specificity leading to high biopsy rates, magnetic field effects, side effects of contrast agents, claustrophobia, long setup and acquisition times and the prohibitively high cost for assessments. MRI has intrinsically higher sensitivity compared to mammography for breast cancer detection (greater than 90%) but has variable specificity between 30% and 90% [34]. Women with metallic or electronic implants may be excluded from using MRI due to the risk of severe injury from the strong magnetic field. Gadolinium contrast agents also add additional risk to the patient, including possible allergic reactions and a risk of nephrogenic systemic fibrosis. Due to the disadvantages associated with MRI, particularly the poor specificity, it has not been recommended by the American Cancer Society as an alternative to mammography for screening [35]. Several studies have investigated screening women who have the BRCA1 or BRCA2 gene mutation using mammography with and without adjunct MRI. Estimates of the sensitivity and specificity of mammography alone was approximately 40% and 95% respectively. The corresponding estimates for mammography with adjunct MRI were approximately 95% and 80% [36] [37]. These studies showed a clear increase in sensitivity and a smaller decrease in specificity, leading to the Ministry of Health New Zealand recommending annual MRI screening for women possessing the BRAC1 or BRAC2 gene from 10 years prior to the age of onset for the youngest affected family relative [38]. Annual mammography is also recommended for these women, but only after the age of 30.

### 1.3.5 Breast Computed Tomography

Dedicated Breast Computed Tomography (BCT) machines have been developed with the advent of flat-panel digital detectors. The patient lies prone on a dedicated table with the breast placed in a pendant position through a hole. The X-ray tube and detector rotate horizontally around the breast below the table [39]. With this technique, the problem of under- and overlying tissues evident in conventional two-dimensional mammography is

eliminated with the ability to view individual slices of a three-dimensional (3D) image of the breast. An additional advantage is that breast compression is unnecessary. A disadvantage of BCT is the increased dose. Some studies, however, claim to achieve dose levels comparable to two-view mammography [40]. While BCT has potential as an alternative to conventional mammography for screening purposes, it remains an experimental technology. It lacks sufficient clinical data for adoption into screening programmes [40].

### 1.3.6 Other Technologies

Other technologies pertinent to breast screening include thermography, positron emission tomography (PET) and clinical breast examination. Thermography involves measuring the temperature distribution on the surface of the breast, assuming higher temperatures indicate an area of a malignant tumor. A systematic review of diagnostic studies performed in 2013 found sensitivities ranged from 25% to 97% and specificities from 12% to 85%. The conclusion from the studies was that there is insufficient evidence to recommend thermography for breast cancer screening [41]. The National Screening Unit of New Zealand, The Cancer Society of New Zealand, The New Zealand Breast Cancer Foundation and The New Zealand Branch of the Royal Australian and New Zealand College of Radiologists do not support the use of thermography for screening or diagnosis [42]. PET maps the uptake of a radiotracer, typically [$^{18}$F]-fluorodeoxyglucose (FDG), which indicates areas of increased glucose metabolism. Assuming glucose metabolism is increased in tumours, PET can effectively locate these tumours. Whole body PET scanners have insufficient spatial resolution to effectively show small tumours in breasts so are therefore considered inadequate for imaging early stage breast cancer [11]. Positron Emission Mammography (PEM) machines are dedicated breast imaging machines which have superior spatial resolution compared to standard PET scanners. PEM studies involve the administration of 370 MBq of FDG which results in an estimated effective dose of 6.2-7.1 mSv [43]. This equates to approximately 16 times more dose than a standard two-view digital mammography examination which is approximately 0.44 mSv [43]. One study found that the diagnostic sensitivity of PEM was 91% and that the specificity was 84% [44]. PEM has not been investigated as a screening tool in any studies. Although the technique has high sensitivity, the low specificity, high radiation dose and high cost compared to digital mammography has eliminated PEM as suitable for screening purposes. Clinical breast examination (CBE) involves both a visual inspection and palpation of the breasts by a trained health care provider to look for lumps or visual changes. Based on pooled data of six studies, the sensitivity of CBE was estimated as 54% and specificity as 94% [45]. The international agency for research on cancer (IARC) concluded that there is sufficient evidence to suggest that screening by CBE improves the earlier detection of tumours but there is currently inadequate evidence that screening by CBE alone reduces breast cancer mortality [11].

## 1.4 X-ray Radiation

X-ray radiation was discovered in 1895 by German physicist, Wilhelm Konrad Röentgen, whilst performing an experiment involving cathode ray tubes [46]. During the experiment, Roentgen noticed that while the cathode ray tube was operating, a fluorescent screen, stored in the corner across the laboratory, was glowing. The fluorescent screen continued to glow even after it was shielded from visible and ultra-violet light produced by the cathode ray tube. Roentgen concluded that some form of invisible radiation was able to pass through material and interact with the fluorescent screen. In keeping with mathematical convention, Roentgen assigned the letter "$x$" to represent the unknown nature of the ray. He further demonstrated the penetrating nature of X-rays by producing the first absorption-based image of the bones in the human hand. This discovery was met with worldwide excitement and rapid clinical implementation of the newly discovered radiation.

### 1.4.1 Electromagnetic Radiation

X-rays are a type of electromagnetic (EM) radiation. EM radiation is characterised using either wavelength ($\lambda$), frequency ($f$) or energy. X-rays lie at the short wavelength, high frequency and high energy end of the EM spectrum. Gamma rays are also a type of EM radiation with, on average, higher energies than X-rays. Gamma rays are emitted by the decay of the nucleus of a radioactive atom whereas X-rays are produced outside the nucleus of atoms. EM radiation has a constant speed in a given medium and has no rest mass. EM radiation can propagate through matter or vacuum. Its maximum group velocity of $\approx 3 \times 10^8$ ms$^{-1}$ occurs in vacuum.

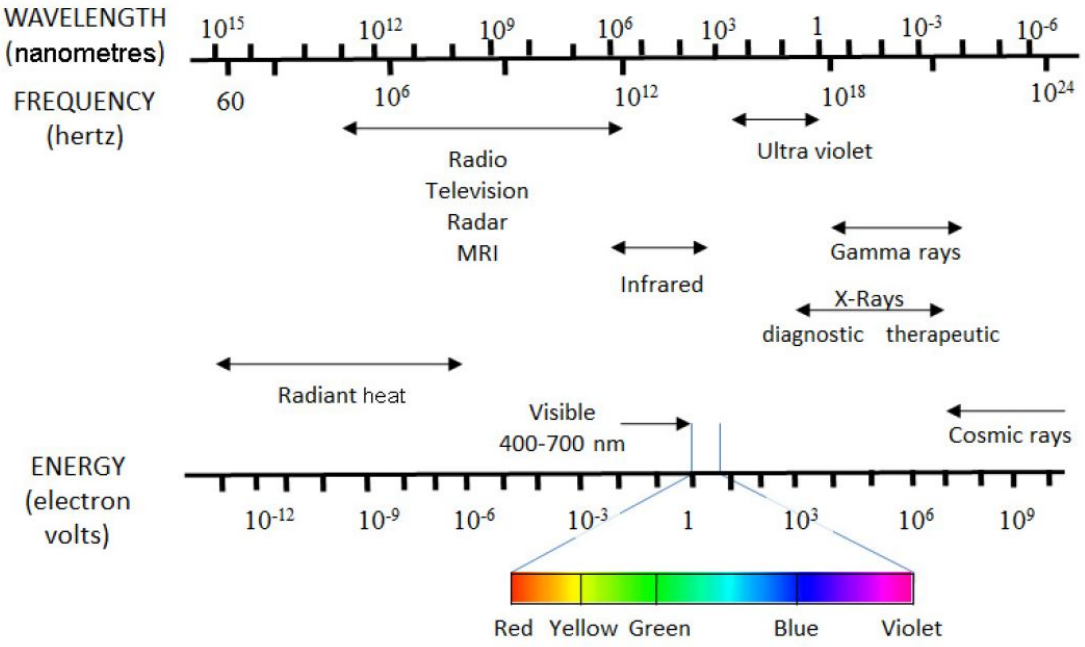


***Figure 1.1:*** *The Electromagnetic Spectrum [12]*

### 1.4.2 Wave Particle Duality

Throughout history, physicists have debated whether light consists of particles or waves. Ancient Greeks considered light to consist of tiny particles called corpuscles. Isaac Newton also believed in a particle theory of light. Christian Huygens in 1698 proposed that light had wave properties. In 1801, Thomas Young provided compelling evidence for the wave theory of light by demonstrating that light beams can interfere to produce interference patterns [47]. A discovery in the early 1860s with James Clerk Maxwell's four equations, which demonstrate that a changing magnetic field induces an electric field and vice versa [47], was a major advancement. Maxwell's equations can be solved to produce harmonic waves travelling at the speed of light, $c$. This discovery led to the recognition that EM radiation travels as waves comprising in phase oscillating electric and magnetic fields at right angles to each other and to the direction of travel as shown in Figure 1.2.

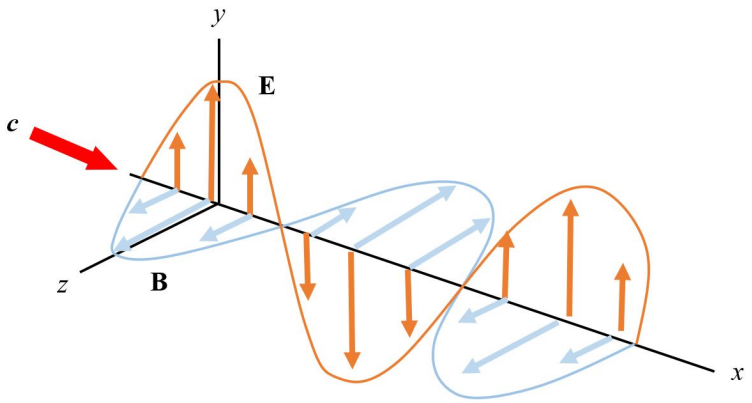


***Figure 1.2:*** *A diagram of an electromagnetic wave propagating at velocity, c in the x direction. The electric field oscillates in the xy plane, and the magnetic field oscillates in the xz plane [47].*

In the early twentieth century, Max Planck returned to the particle theory of light to explain how radiation is emitted by hot objects. In 1905, Albert Einstein provided further evidence for the particle theory by demonstrating the photoelectric effect, where electrons are emitted by a metal exposed to light. In the particle theory, light is composed of photons travelling at the speed of light. A photon is imagined as a massless particle-like packet of energy. It is now known that light has wave-particle duality in which it demonstrates wave properties in some situations and particle properties in other situations. X-rays also demonstrate optical phenomena such as refraction and attenuation.

### 1.4.3 Ionising Radiation

EM radiation is classified as either ionising or non-ionising, depending on its ability to ionise matter [12]. An atom becomes ionised when an orbital electron is removed, resulting in an overall positive charge. The amount of energy required to remove an electron from an atom is known as the ionisation potential. This energy range is a few electron volts

for alkali metals to 24.5 eV for helium. For water, which comprises most of the matter in human cells, the ionisation potential is 12.6 eV [12]. The radiobiological demarcation between ionising and non-ionising EM radiation is, therefore, approximately 12.6 eV. With reference to Figure 1.1, EM radiation having higher energy than the ultraviolet region is ionising, while EM radiation with energy below the ultraviolet region is non-ionising. Ionising EM radiation is capable of causing damage to DNA in human cells, leading to an increased risk of radiation induced cancer. Particulate radiations such as alpha and beta particles are also ionising.

## 1.5 X-ray Production

X-rays are produced when energetic electrons interact with either matter or a magnetic field. During these interactions, a portion of the incident electron's kinetic energy is converted into high energy EM radiation. X-rays produced using conventional diagnostic radiology equipment are either bremsstrahlung or characteristic X-rays. Bremsstrahlung X-rays are produced when an incident electron is rapidly decelerated by the opposing positive charge of the atomic nucleus of an absorbing material. The loss of kinetic energy of the electron is converted into the creation of a bremsstrahlung X-ray photon. The energy of the resultant photon ranges from very low, to the original energy of the incident electron. This energy is determined by how close the incident electron passes to the nucleus of the absorbing material. A close encounter with the nucleus will decelerate the electron to a greater extent. Bremsstrahlung radiation can also be produced by applying a magnetic field to a highly energetic electron. The magnetic field causes a deflection of the electron thus giving rise to an X-ray photon. Radiation produced in this manner is called magneto-bremsstrahlung or synchrotron radiation. Characteristic X-rays are produced when an incident electron has sufficient kinetic energy to exceed the binding energy of an orbital electron within an electron shell of a target atom, thus creating a vacancy in that shell. This vacancy is immediately filled by an outer shell electron and a characteristic X-ray is emitted with an energy equal to the difference in binding energies of the two shells.

### 1.5.1 X-ray Tubes

At diagnostic X-ray tube voltages, both bremmstrahlung and characteristic X-ray photons are produced. An X-ray tube comprises an electron source, an evacuated enclosure in which the electrons can be accelerated unimpeded, a target anode and a high voltage power supply. The electron source consists of a tungsten filament through which a current is passed. The current causes the filament to become white hot with electrons leaving the surface in a process called thermionic emission. The high voltage power supply provides a large potential difference between the filament (cathode) and the target (anode). This large potential difference accelerates the electrons, which have left the surface of the filament, towards the positively charged anode [15]. The anode and cathode are encased in a glass evacuated enclosure to prevent the accelerating electrons from interacting with unwanted

material in the path to the anode. The anode target material in general radiography applications is tungsten which has a high atomic number and melting temperature thus maximising bremsstrahlung efficiency and minimising heat damage to the anode. The highly energetic electrons which have been accelerated from the cathode to the anode collide with the tungsten anode, producing bremsstrahlung radiation through interactions with the target nuclei, and characteristic radiation, through interactions with the target orbital electrons. Most of the interactions between the incident electrons and the tungsten anode are collisional, giving rise to heat, without producing radiation. At a tube voltage of 100 kV, less than 1% of the input energy results in X-ray production. The remaining energy is wasted as heat [12]. Spinning anodes, and other cooling systems, are designed to disperse the heat and prevent early failure of the tube. The output spectrum of an X-ray tube comprises a continuum of Bremsstrahlung photons overlaid with discreet spikes from characteristic X-ray photons.

### 1.5.2 Synctrotron Sources

Synchrotron, or magneto-bremsstrahlung, radiation generation involves accelerating electrons to relativistic speeds before passing them through a bending magnet or an insertion device such as a wiggler or undulator to produce EM radiation [48]. Synchrotrons, such as the Australian Synchrotron in Clayton, Victoria, accelerate electrons by first using a linear accelerator to accelerate bunches of electrons up to an energy of 100 MeV. These relativistic electrons are then injected into a booster ring and further accelerated to an energy of 3 GeV. Within the booster ring are steering and focusing electromagnets which channel the electrons through a stainless steel vacuum chamber comprising the ring. The ring also contains a radio-frequency cavity to provide energy input for electron acceleration. These very high energy electrons are then transferred into a large outer storage ring which can hold 200 mA of stored current. The storage ring at the Australian Synchrotron has a 216 meter circumference and consists of a number of sectors, each containing a straight and curved section [49]. The straight sections can be replaced by insertion devices such as wigglers or undulators. These insertion devices produce synchrotron radiation by passing relativistic electrons through periodic magnetic structures [48]. The curved sections of the storage ring contain a pair of dipole bending magnets which curve the electron path, producing sychrotron radiation. Several beamlines are positioned around the storage ring to capture the radiation produced by the bending magnets or insertion devices. The radiation channelled into the beamlines is utilised in end stations for various experiments. The imaging and medical beamline (IMBL) at the Australian Synchrotron has been used for X-ray phase-contrast imaging (PCI) experiments. This beamline is based on a super-conducting wiggler that, in conjunction with a monochromator, provides a wide monochromatic and nearly parallel X-ray beam with an area of up to 500mm x 40mm (h x v) at a distance of 140m from the source [50]. A bent double-crystal monochromator is employed which is used to provide an energy range between 20 and 120 keV with an energy resolution of $\Delta E/E = 10^{-3}$. Situated along the beamline are 6 radiation enclosures called hutches. Propagation-based phase-contrast imaging (PBPCI) experiments are performed in hutch

number 3B, which is the farthest from the source and provides the smallest effective source size [51] [52].

## 1.6 X-ray Propagation in Free Space

### 1.6.1 Spatial and Temporal Coherence

Some methods of phase-contrast imaging (PCI) depend on X-ray wave fields with a high level of spatial and temporal coherence. Spatial coherence is a measure of the phase coherence transverse to the direction of propagation [53]. Temporal coherence is a measure of how monochromatic a wave field is. It also refers to the amount of coherence in the direction of propagation of the wave field (longitudinal coherence) [54]. Laboratory X-ray tube sources typically produce a polychromatic photon spectrum with low spatial coherence. Coherence of a wave field can be improved by using filters in the spatial and temporal domains. Spatial filtering is achieved by either reduction of the source size, with slits or pin holes, or an increased source-to-object distance. Temporal filtering is achieved by using a monochromator which has a narrow wavelength bandwidth [55]. The consequence of applying filtering techniques is a substantial decrease in intensity [53]. If such filtering techniques were to be applied to a conventional X-ray source, the concomitant decrease in intensity would necessitate impractically long exposure times. Synchrotron X-ray sources produce very high intensity radiation. With the use of monochromators and extended source-to-object distances, X-ray wave fields with adequate spatial and temporal coherence to acquire useful phase-contrast images with acceptable exposure times can be generated [54].

### 1.6.2 Scalar Wave Equation and the Complex Wave Function

X-rays used in diagnostic radiology have energies ranging from 15 keV to 140 keV [15]. All EM waves can be described mathematically by the Maxwell equations [56]. These equations comprise sets of coupled partial differential equations describing electric and magnetic fields. Using the approach, for example, described in Section 1.1 of Paganin (2006) [48] the d'Alembert equations can be derived from the free space Maxwell equations. The d'Alembert equations describe the electric and magnetic component of an EM disturbance with an electric and magnetic vector field at each point in space-time. For simplicity, the vector theory of an EM field in free space can be substituted by a scalar theory as described in Section 1.1 of [48]. Using a vector theory of an EM wave in vacuum, the electric and magnetic field disturbance is specified, at each point in space and time. Using a scalar theory, the disturbance can be characterised by a single scalar field $\Psi(x, y, z, t)$, and the d'Alembert equation becomes:

$$\left(\frac{1}{c^2}\frac{\partial^2}{\partial t^2} - \nabla^2\right)\Psi(x, y, z, t) = 0. \tag{1.1}$$

$\Psi(x, y, z, t)$ can be treated as a complex function with both magnitude and phase such that:

$$\Psi(x, y, z, t) = \sqrt{I(x, y, z, t)} \exp\left[i\phi(x, y, z, t)\right], \tag{1.2}$$

where $I(x, y, z, t)$ is the intensity of the field and the phase is $\phi(x, y, z, t)$.

### 1.6.3 Coherent Fields

X-ray image quality can be improved by utilising information on the phase shift of the X-ray field which has passed through an object. The phase shift, however, must first be obtained using phase retrieval methods. The task of phase retrieval is significantly simplified if the X-ray field, prior to passing through the object, is known to have high spatial and temporal coherence. X-ray fields, with sufficient spatial and temporal coherence for PCI experiments, can be produced with synchrotron sources that have large source-to-object distances and monochromators.

If a field is spatially coherent and monochromatic then it oscillates at a fixed angular frequency $\omega$ and

$$\Psi(x, y, z, t) = \psi(x, y, z) \exp\left(-i\omega t\right). \tag{1.3}$$

Substituting Equation 1.3 into Equation 1.1 results in the Helmholtz Equation in vacuum [48]:

$$(\nabla^2 + k^2)\psi(x, y, z) = 0. \tag{1.4}$$

### 1.6.4 Coherent Paraxial Fields

Determination of the phase change of an X-ray field which has passed through an object, also known as phase retrieval, is further simplified when the initial X-ray field is not only coherent, but also paraxial.

Using a geometric optics approximation of X-rays, a paraxial field is a field in which the rays make a small angle with respect to the optic axis, i.e. almost parallel to the optic axis. With a wave optics interpretation, all points along the lines of constant phase, or wave fronts, have a Poynting vector which is close to parallel with the optic axis. An X-ray field with zero divergence from the source is impossible to generate. Under certain conditions, however, an X-ray field with only slight divergence can be created [57]. Such conditions exist in synchrotron PCI systems which employ extended source-to-object distances and collimating monochromators.

Consider the Helmholtz Equation (1.4) where the incident X-ray field is paraxial. Expressing the solution of Equation 1.4, $\psi(x, y, z)$, as the product of a plane wave travelling

in the $z$-direction, $e^{ikz}$, and a perturbing envelope, $\tilde{\psi}(x,y,z)$, the following is derived:

$$\psi(x,y,z) = \tilde{\psi}(x,y,z)e^{ikz}. \tag{1.5}$$

Here $\tilde{\psi}(x,y,z)$ represents a slowly varying function which, when multiplied by the z-directed plane wave, $e^{ikz}$, effectively deforms the z-directed plane wave fronts. Here,

$$|\tilde{\psi}(x,y,z)|^2 = |\psi(x,y,z)|^2 = I(x,y,z). \tag{1.6}$$

Substitute Equation 1.5 into the Helmholtz Equation (1.4), and making use of the identity:

$$\begin{aligned}\nabla^2[A(x,y,z)B(x,y,z)] = A(x,y,z)\nabla^2 B(x,y,z)+\\ B(x,y,z)\nabla^2 A(x,y,z) + 2\nabla A(x,y,z)\cdot\nabla B(x,y,z),\end{aligned} \tag{1.7}$$

for suitably well-behaved functions $A(x,y,z)$ and $B(x,y,z)$, to arrive at:

$$\left(2ik\frac{\partial}{\partial z} + \nabla_\perp^2 + \frac{\partial^2}{\partial z^2}\right)\tilde{\psi}(x,y,z) = 0. \tag{1.8}$$

In the above equation, $\nabla^2$ is written as $\nabla_\perp^2 + \partial^2/\partial z^2$, where $\nabla_\perp^2$ is the transverse Laplacian, or the Laplacian in the xy-plane, which is equal to $\partial^2/\partial x^2 + \partial^2/\partial y^2$. Due to the paraxial approximation, the second derivative with respect to $z$ is close to zero and can be disregarded. This will be a good approximation if the envelope, $\tilde{\psi}(x,y,z)$, is 'beamlike' or more strongly varying in the $x$- and $y$-directions than in the $z$-direction [48]. Equation 1.8 now becomes:

$$\left(2ik\frac{\partial}{\partial z} + \nabla_\perp^2\right)\tilde{\psi}(x,y,z) = 0. \tag{1.9}$$

## 1.7 X-ray Interactions with Matter

The previous section introduced the equations which govern the propagation of X-rays in vacuum. This section examines the range of interactions of X-rays with scattering media and introduces the application of the wave equations in the presence of this scattering media.

### 1.7.1 Mechanisms of Attenuation

When X-ray photons traverse matter they may penetrate without interaction, scatter or be absorbed. The three major interactions between photons and matter in the diagnostic radiology energy range are: Rayleigh scattering, Compton scattering and photoelectric absorption [15].

### Rayleigh Scattering

Rayleigh scattering involves the temporary excitation of an entire atom by an incident photon [15]. The energy from the excited atom is re-released as a scattered photon with the same energy and wavelength as the incident photon but with a slightly different direction. The atom then returns to its previous non-excited state. The conservation of energy between the incident and scattered photon results in Rayleigh scattering being an elastic scattering event. Rayleigh scattering tends to occur at low X-ray energies, such as those in mammography. The small scattering angles associated with Rayleigh interactions result in deleterious effects on image quality. This type of scattering, however, has a low probability of occurring and only accounts for approximately 10% of interactions at 30 keV [15].

### Compton Scattering

A Compton scattering event occurs when an incident photon interacts with an outer orbital electron [15]. This leads to the incident photon losing a portion of its energy and being scattered relative to its initial direction. Energy and momentum are conserved such that the energy lost by the incident photon is transferred to the orbital electron. The electron is ejected from the atom with extra kinetic energy. The energy of the incident photon is equal to the sum of the energy of the scattered photon and the kinetic energy transferred the ejected electron. Compton scattering results in ionisation of the atom due to the ejection of an electron. It is the predominant interaction of X-ray photons with soft tissue in the diagnostic energy range above 26 keV [15]. The Compton mass attenuation coefficient is effectively independent of atomic number so, being the dominant interaction in soft tissue, contrast between different soft tissues in standard X-ray images is poor. Compton scattering also has a deleterious effect on image quality as the scattering of photons results in increased noise in the image, thus further degrading soft tissue contrast.

### Photoelectric Effect

In photoelectric interactions, an incident photon transfers all its energy to an inner shell electron. The energy of the incident photon must first exceed the binding energy of the electron for this interaction to occur. The net result is complete absorption of the incident photon and ejection of the inner shell electron from the atom. The kinetic energy of the ejected photo-electron is equal to the incident photon energy minus the binding energy of the inner shell electron. With the removal of the inner shell electron, the atom is ionised. This vacancy is quickly filled by an outer shell electron, resulting in emission of a characteristic X-ray or an Auger electron. The mass photoelectric attenuation coefficient is approximately proportional to $Z^3/E^3$, where Z is the atomic number and E is the energy of the incident photon [15, 58]. Traditional mammography uses specialised anode materials and filter combinations, as discussed in section 1.3.1, to produce low energy X-rays which increase photoelectric interactions in soft tissue, thus improving contrast between tissues with slightly different atomic numbers.

The attenuation of an X-ray beam as it passes through matter by these three major attenuation mechanisms is represented by a singular linear attenuation coefficient, $\mu$. This is illustrated in Figure 1.3 which shows the mass attenuation coefficient which is equal to $\mu/\rho$, where $\rho$ is mass density, on the y-axis.

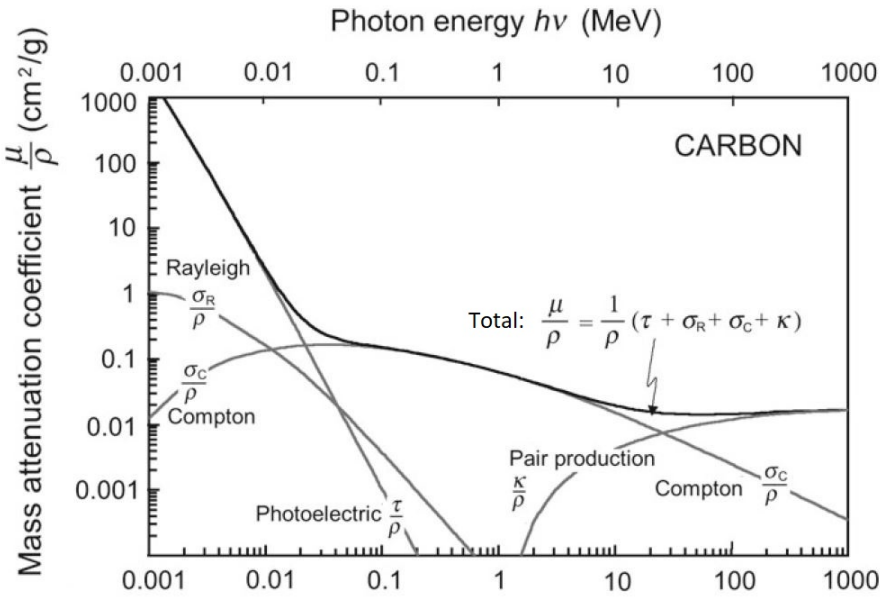


***Figure 1.3:*** *Graph of the Rayleigh, Compton, photoelectric, pair production and total mass attenuation coefficients for carbon as a function of photon energy [58]*

### 1.7.2 Wave Equations in Matter

PCI in mammography requires the wave equations (1.4 and 1.9) to be applied so as to account for the scattering conditions within breast tissue. Breast tissue can be described by a position- and frequency-dependent refractive index, $n(x, y, z)$. Noting that the wavelength in the medium is equal to the vacuum wavelength divided by the refractive index of the medium, the 'inhomogeneous' Helmholtz equation is derived (see Section 2.1 of [48] for a full derivation) such that:

$$[\nabla^2 + k^2 n^2(x, y, z)]\psi(x, y, z) = 0. \tag{1.10}$$

Assuming the X-ray field produced by a synchrotron source is effectively paraxial, the paraxial, inhomogeneous Helmholtz equation becomes:

$$\left(2ik\frac{\partial}{\partial z} + \nabla_\perp^2 + k^2[n^2(x, y, z) - 1]\right)\tilde{\psi}(x, y, z) = 0. \tag{1.11}$$

### 1.7.3 The Projection Approximation, Attenuation and Refraction

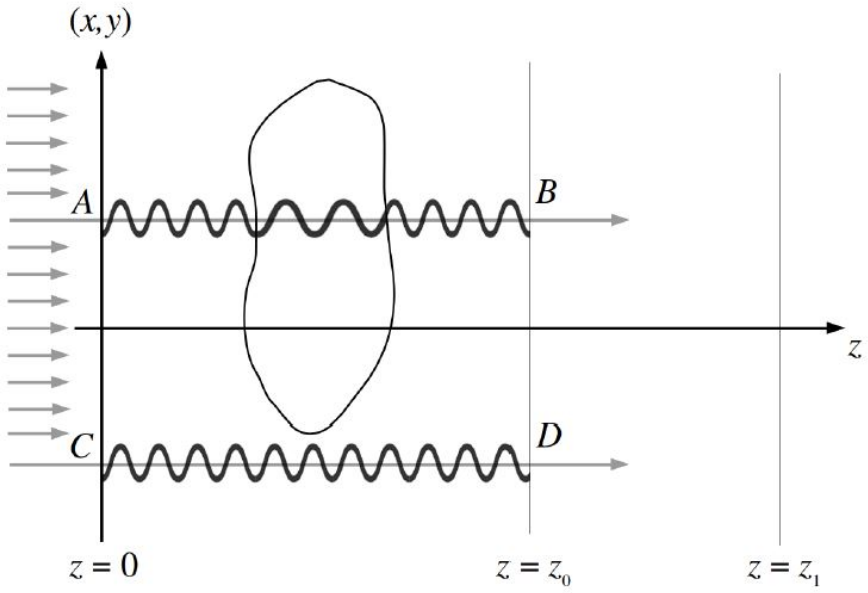


***Figure 1.4:*** *X-ray wave field travelling from the entrance surface, through an object, to the exit surface under the projection approximation [48]*

Figure 1.4 illustrates a material contained within an area $0 < z < z_0$, which is irradiated by z-directed, monochromatic X-rays from the left side. The complex disturbance at the exit surface of the material ($z = z_0$) is a function of the complex disturbance at the entrance surface ($z = 0$) and the refractive index distribution of the material. The refractive index for hard X-rays passing through soft tissue is approximately unity, implying that the interactions between these X-rays and the material is weak. The paths of the X-rays are assumed to be negligibly perturbed and remain almost parallel to the z axis as they pass through the length of the material as shown in Figure 1.4. This assumption, known as the

projection approximation, allows the transverse Laplacian term, $\nabla_{\perp}^2$, in Equation 1.11 to be disregarded such that:

$$\frac{\partial}{\partial z}\tilde{\psi}(x,y,z) \approx \frac{k}{2i}[1-n^2(x,y,z)]\tilde{\psi}(x,y,z). \tag{1.12}$$

This is a linear first order, ordinary differential equation which can be integrated with respect to $z$ to give:

$$\tilde{\psi}(x,y,z=z_0) \approx \exp\left\{\frac{k}{2i}\int_{z=0}^{z=z_0}[1-n^2(x,y,z)]dz\right\}\tilde{\psi}(x,y,z=0). \tag{1.13}$$

The refractive index for X-rays is approximately unity so the equation is often expressed as:

$$n = 1-\delta+i\beta, \tag{1.14}$$

where the real decrement, $\delta$, is related to the phase shift, or refraction of the X-ray beam, and the imaginary decrement, $\beta$, is related to the attenuation. The complex refractive index for hard X-rays is approximately unity, thus $|\delta|$, $|\beta| \ll 1$ and:

$$1-n^2(x,y,z) \approx 2[\delta(x,y,z)-i\beta(x,y,z)]. \tag{1.15}$$

The terms containing $\delta^2$, $\beta^2$ and $\delta\beta$ are small and can be disregarded. Equation 1.15 is substituted into Equation 1.13 to become:

$$\tilde{\psi}(x,y,z=z_0) \approx \exp\left\{-ik\int_{z=0}^{z=z_0}[\delta(x,y,z)-i\beta(x,y,z)]dz\right\}\tilde{\psi}(x,y,z=0). \tag{1.16}$$

This equation gives the exit wave field, $\tilde{\psi}(x,y,z=z_0)$ in terms of the entrance wave field, $\tilde{\psi}(x,y,z=0)$ multiplied by a transmission function. The transmission function is the exponential term in the above equation.

The phase shift and attenuation of the X-ray wave field are now considered separately. According to Equation 1.16 the phase shift, $\Delta\phi(x,y)$, experienced by the wave field passing from $z=0$ to $z=z_0$ is:

$$\Delta\phi(x,y) = -k\int\delta(x,y,z)dz. \tag{1.17}$$

If the material is composed of a homogeneous material, $\delta$ is a constant and can be removed from the integral. If the material has a thickness $T(x,y)$ along the $z$-direction, the previous equation reduces to:

$$\Delta\phi(x,y) = -k\delta T(x,y). \tag{1.18}$$

Taking the squared modulus of Equation 1.16 and recalling $|\tilde{\psi}(x,y,z)|^2 = I(x,y,z)$ (Equation 1.6), the following equation is derived:

$$I(x, y, z = z_0) = \exp\left[-2k \int \beta(x, y, z)dz\right] I(x, y, z = 0). \tag{1.19}$$

When the material is composed of a homogeneous material, $\beta$ is a constant and can be removed from the integral. If the material has a thickness $T(x, y)$ along the $z$-direction, the previous equation reduces to Beer's law of absorption in a homogeneous material, which is pivotal in conventional attenuation-based imaging:

$$I(x, y, z = z_0) = \exp\left[-\mu T(x, y)\right] I(x, y, z = 0). \tag{1.20}$$

In the equation above, $\mu = 2k\beta$ is the linear attenuation coefficient which was introduced at the end of Section 1.7.1.

## 1.8 Phase-Contrast Imaging

Since the discovery of X-rays, medical X-ray imaging has utilised differences in attenuation of various tissues to produce image contrast. PCI involving X-rays has been a focus of some research and development in the medical field in recent times. PCI exploits the phase shift by X-ray waves passing through different components of a sample. Through the application of a PCI technique, the phase-shift introduced by an object produces variations in intensity which can be recorded by a detector. A useful metric, when comparing the theoretical relative contrast between different types of breast tissue using phase-contrast and absorption-based imaging, is the relative value of $\delta$ and $\beta$ associated with each breast tissue type [57]. Figure 1.5 illustrates the difference between breast glandular tissue and adipose tissue for both the real part, $\Delta\delta = \delta_{glan} - \delta_{adi}$, and the imaginary part, $\Delta\beta = \beta_{glan} - \beta_{adi}$, of the complex refractive indices for the X-ray energy range used in mammography imaging. Note that for all energies shown, $\Delta\delta \gg \Delta\beta$. At an X-ray energy of 32 keV, which was recently used for breast imaging experiments at the IMBL of the Australian Synchrotron (Clayton, Victoria) [59], the ratio, $\Delta\delta/\Delta\beta$ was equal to 870 [60] for glandular tissue in adipose tissue. This suggests that PCI, which utilises differences in the real component of the refractive index, $\delta$, may in some cases, offer an advantage when differentiating soft tissues compared to conventional attenuation-contrast methods, which utilise differences in the imaginary component, $\beta$ [57]. If phase-contrast mammography imaging can be implemented in a clinical setting it has the potential to significantly improve breast cancer diagnosis and characterisation [61].

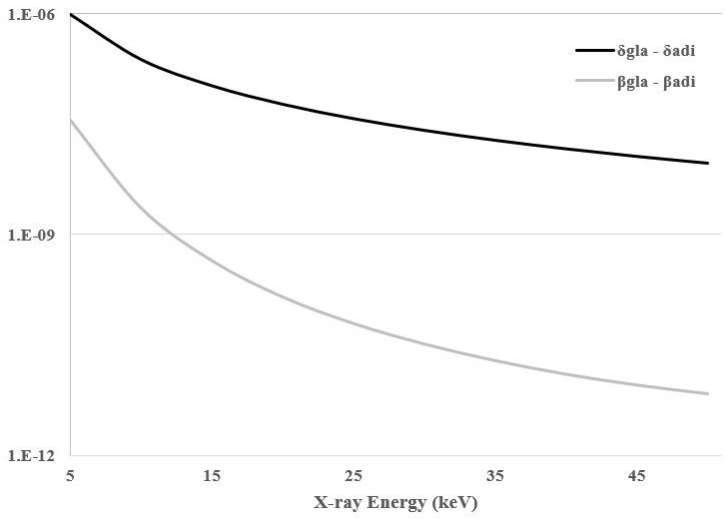


***Figure 1.5:*** *Calculated differences between the real and imaginary components of the complex refractive index between glandular tissue and adipose tissue. Data sourced from [60]*

### 1.8.1 Propagation-Based Phase-Contrast Imaging

The simplest and most common PCI method is propagation-based phase-contrast imaging (PBPCI) [62]. As with conventional X-ray imaging, PBPCI uses an X-ray source, an object to be imaged and a detector. The main difference between the two methods is the requirement for high spatial coherence and the detector-object distance, which is extended in PBPCI. This free space propagation distance allows phase differences in the X-ray field to be converted into intensity modulations which are then recorded by a detector [63]. The mechanism by which these intensity variations occur is Fresnel diffraction. This is depicted by considering the X-ray field as rays in Figure 1.6 and waves in Figure 1.7. The enhancement of edges due to the appearance of Fresnel fringes, as depicted in Figure 1.7, is a characteristic feature of PBPCI. At point Q, in Figure 1.6, there is a decrease in intensity, while at point P there is an increase, corresponding to the edge of the sample. The evolution of these edge enhancing Fresnel fringes through the free space propagation distance is depicted on the right of Figure 1.7 and can be seen on the images of Figure 1.8.

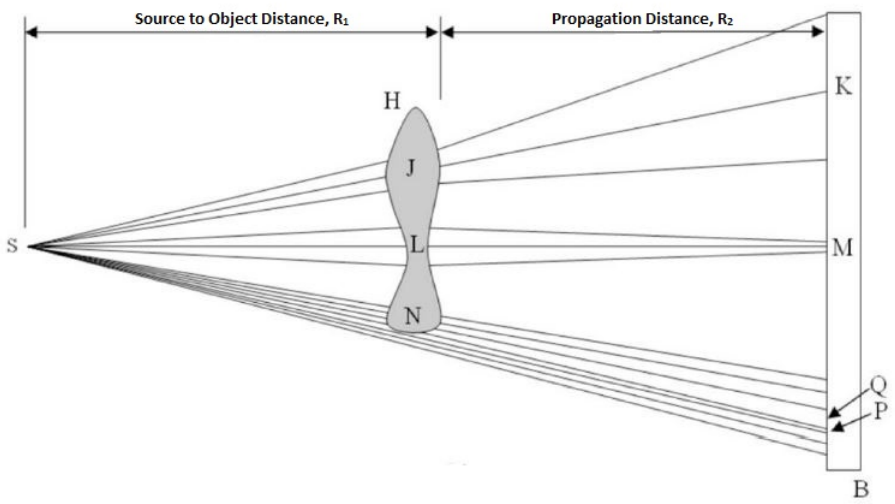


***Figure 1.6:*** *Geometric-optics ray based diagram showing the evolution of intensity modulations due to phase differences through free space propagation [64]*

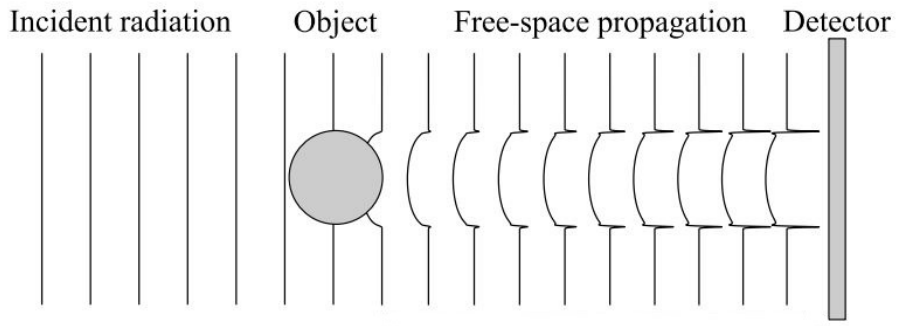


***Figure 1.7:*** *Wave based diagram showing the evolution of intensity modulations due to phase differences through free space propagation [63]*

### Fresnel Diffraction

Fresnel diffraction describes the intensity variations in the near field due to phase shifts of the X-ray field after passing through an object in PBPCI experiments. The near field is the region in which the Fresnel number (defined here in the case of plane wave illumination),

$$N_F = \frac{h^2}{\lambda R_2}, \tag{1.21}$$

is much larger than unity. In the equation above, $h$ is the size of the smallest feature in the object, or the spatial resolution limit of the imaging system (whichever is larger), $\lambda$ is the wavelength and $R_2$ is the propagation distance (adapted from [66]). The region where $N_F \ll 1$ is the far field, or Fraunhofer region.

Using a Cartesian coordinate system $(x, y, z)$, where the positive $z$ axis represents the nominal optic axis, a sample is situated at a plane some distance from the source, $z = 0$. Assume the scalar X-ray field is paraxial, sufficiently coherent and monochromatic. Under

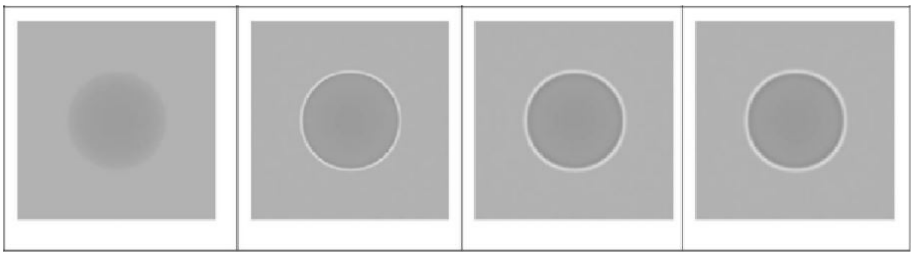

***Figure 1.8:*** *Simulated PBPCI images of a solid carbon sphere of 0.5 mm diameter. The source to object distance is fixed at 10 cm, while the object to detector distance, $R_2$, increases from left to right. The left most image is a contact, absorption based image at $R_2 = 0$. The remaining images, from left to right have propagation distances of $R_2 =$ 10 cm, 50 cm and 100 cm respectively. Image adapted from [65]*

these assumptions, Fresnel diffraction theory describes the wave field over the plane $z > 0$ due to diffraction caused by a disturbance of the X-ray field at $z = 0$, where the space $z \geq 0$ is vacuum [48]. Consider an operator formulation for Fresnel diffraction. The wave field at $z > 0$, denoted $\psi_\omega(x, y, z = R_2)$, can be expressed as the wave field at $z = 0$, denoted $\psi_\omega(x, y, z = 0)$, acted on by a Fresnel diffraction operator to propagate it through a distance $R_2$ [48]:

$$\psi(x, y, z = R_2 \geq 0) \approx \exp(ikR_2)\mathcal{F}^{-1} \exp\left[\frac{-iR_2(k_x^2 + k_y^2)}{2k}\right]\mathcal{F}\psi(x, y, z = 0). \tag{1.22}$$

In the expression above, $\mathcal{F}$ indicates a two-dimensional Fourier transform and $\mathcal{F}^{-1}$ indicates an inverse two-dimensional Fourier transform, $k_x$ and $k_y$ respectively give the $x$ and $y$ components of the wave vector $\mathbf{k}$. This expression can be solved numerically, making use of fast Fourier transform algorithms.

An equivalent formulation for Fresnel diffraction can be derived through a treatment based on the convolution integral. This treatment results in the Fresnel diffraction integral, which expresses the propagated field as the sum of the propagated disturbances, which are due to each of the points $(x', y')$ on the incident wavefront over the plane $z = 0$ [48]:

$$\begin{aligned}\psi(x, y, z = R_2 \geq 0) = -\frac{ik\exp(ikR_2)}{2\pi R_2}\exp\left[\frac{ik}{2R_2}(x^2 + y^2)\right] \\ \times \int\int_{-\infty}^{\infty} \psi(x', y', z = 0)\exp\left[\frac{ik}{2R_2}(x'^2 + y'^2)\right] \\ \times \exp\left[\frac{-ik}{R_2}(xx' + yy')\right]dx'dy'.\end{aligned} \tag{1.23}$$

The Fresnel diffraction integral also provides a convenient means for numerically computing coherent diffraction patterns [48].

**Transport of Intensity Equation**

Teague (1982) [67] first established the quantitative relationship between the intensity variation along the optical ($z$) axis and phase of a coherent beam with the Transport of Intensity Equation (TIE). Teague considered a paraxial, coherent and monochromatic beam propagating along the $z$-axis, where the complex amplitude can be expressed by Equation 1.2. Teague substituted Equation 1.2 into the paraxial, free space Helmholtz Equation (1.9) before separating the real and imaginary parts to arrive at the TIE:

$$-\nabla_{\perp} \cdot [I(x,y,z)\nabla_{\perp}\phi(x,y,z)] = k\frac{\partial I(x,y,z)}{\partial z}. \tag{1.24}$$

The TIE describes how variations in intensity are produced by Fresnel diffraction of X-rays in the near field region for PBPCI techniques [68]. The TIE, therefore, can alternatively be derived from the Fresnel diffraction formulas (1.22) and (1.23) [69].

The TIE can be rearranged to yield an expression for the propagated intensity, $I(x,y,z+R_2)$, by first taking the finite difference approximation,

$$\frac{\partial I(x,y,z)}{\partial z} \approx \frac{I(x,y,z+R_2) - I(x,y,z)}{R_2}. \tag{1.25}$$

This expression is then substituted into Equation 1.24 and solved for the propagated intensity, $I(x,y,z+R_2)$, to arrive at the following approximate description for PBPCI within a sufficiently small propagation distance, $R_2$:

$$I(x,y,z+R_2) \approx I(x,y,z) - \frac{R_2}{k}\nabla_{\perp} \cdot [I(x,y,z)\nabla_{\perp}\phi(x,y,z)]. \tag{1.26}$$

In PCI experiments, the phase-shift of the X-ray field cannot be measured directly. The only measurable quantity is the intensity recorded by X-ray detectors. The TIE provides an important link between the intensity measured at the detector and the phase-shift of the X-ray field.

### 1.8.2 Bonse-Hart X-ray Interferometry

The work of Bonse and Hart, published in 1965, provides the earliest example of X-ray PCI using a crystal interferometer [70] [71]. The interferometer uses analyser crystals to split, recombine and create interference with the beam (Figure 1.9). Analyser crystals have a periodic structure with periods, or lattice constants, comparable the wavelength of the X-rays used in interferometry. This allows the crystals to diffract incident X-rays through appreciable angles. The reflectivity of the crystal, as a function of the incident X-ray angle, is sharply peaked at the Bragg angle of the crystal [48]. This angular dependent reflectivity of the crystal is termed the rocking curve of the crystal. The interferometer described by Bonse and Hart makes use of three analyser crystals. The first crystal splits the incident beam into two coherent beams, one of which passes through a sample, and the other is used as a reference beam. The second crystal causes the beams to converge. The converging beams combine at the third crystal to form an interference pattern which is recorded by a

detector. The phase interference effects are resolved using a wedge-shaped phase shifter, which is placed in the reference beam [72]. Without a sample in the interferometer, the reference beam, with the ramp in place, will interfere with the constant phase of the sample beam, causing straight, periodic interference fringes at the detector. When a sample is introduced, the fringes become distorted due to the phase shifts introduced by the sample [57]. Crystal interferometry is a very sensitive PCI method as it directly detects the phase of the wave field rather than derivatives of the phase. This technique can render three-dimensional images through CT as demonstrated by Momose *et al.* (1996) [73]. Adoption of crystal interferometry has been constrained due to difficulties in achieving adequate mechanical stability in the setup. Crystal interferometers also have strict requirements for the spatial and temporal coherence of the X-ray beam.

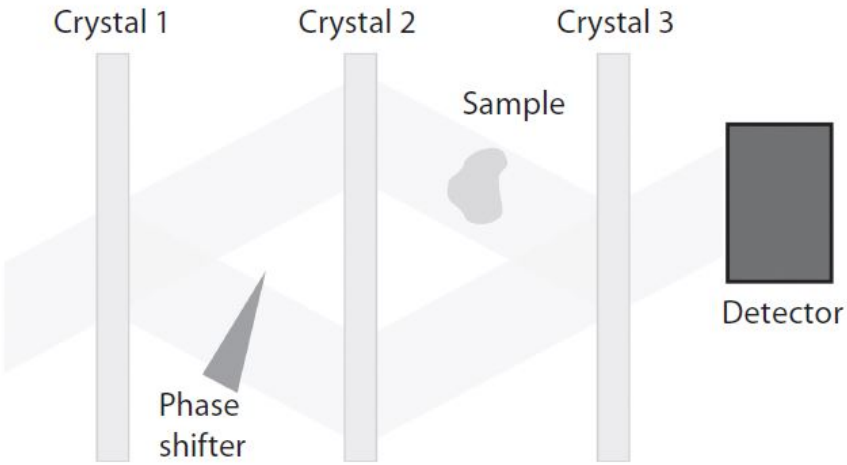


***Figure 1.9:*** *Crystal Interferometer Setup. [57]*

### 1.8.3 Analyser-Based Phase-Contrast Imaging

Analyser-based phase-contrast imaging (ABPCI) uses two sets of crystals. The first set of crystals, placed between the source and the object, acts as a monochromator and collimator of the incident X-ray beam. The second set (analyser crystals) is placed between the object and the detector and acts as an angular filter of the radiation scattered and refracted by the sample [74]. The object-detector distance is small so that propagation phase-contrast effects are minimised [68]. The analyser crystals selectively reflect X-ray photons which satisfy the Bragg condition, i.e those which are incident on the crystallographic planes at an angle which is close to the Bragg angle, while most others are rejected. On passing through the sample, the X-rays are refracted at an angle relative to the incident beam. This refraction angle is proportional to the local gradient of the phase shift imposed by the corresponding part of the sample [75]:

$$\Delta\theta = \frac{1}{k}\frac{\partial\phi(x,y)}{\partial x}. \tag{1.27}$$

The analyser crystal only reflects the un-refracted beam with maximum intensity when the crystal is oriented at the Bragg angle relative to the incident X-ray beam. When the crystal is rotated slightly off the Bragg angle, the refracted beams, for which the new crystal position better satisfies the Bragg condition, are reflected with increased efficiency, as shown in Figure 1.10. The images which are acquired with the crystal in the $\theta_L$ and $\theta_H$ positions ($I_L$ and $I_H$ in Figure 1.10) contain both absorption and phase-contrast information. Each of these ABPCI images is sensitive only to the phase-gradient component in the plane of diffraction, so therefore, only has phase-contrast in one-dimension parallel to the diffraction plane. The phase and absorption contrast components can be extracted from the $I_H$ and $I_L$ images (Figure 1.11 (a) and (b)) using the method demonstrated by Chapman *et al.* (1997) [76]. If the analyser crystal is rotated to an angle positioned at the tail of the rocking curve ($\theta_D$ in Figure 1.10), a dark field image is produced. In the dark field image, only the most strongly scattered X-rays will be displayed in the image, resulting in bright areas corresponding to small features in the object (Figure 1.11 (c)). Dark field images can provide sub-pixel resolution sensitivity of small features which can be used to assess micro-calcifications [77].

The limitations of ABPCI for use in medical applications include the need for high mechanical stability of the crystals, the significant loss of intensity due to the filtering effect of both the monochromator and analyser crystals, which limit the use of conventional X-ray sources, and the field of view being limited to the size of the analyser crystal [74].

### 1.8.4 Grating Interferometry

Grating Interferometry, or Talbot-Lau Interferometry, is a promising technique for achieving phase-contrast images in mammography applications. Grating Interferometry relies on the Talbot effect, first described by Talbot in 1836 [79]. The Talbot effect is evident in the propagation of a monochromatic X-ray wave field beyond a grating [57]. The grat-

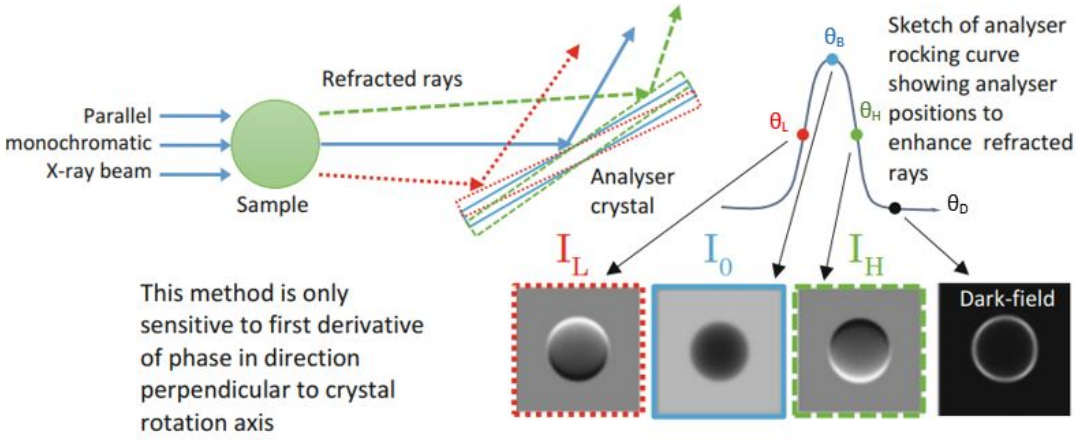


***Figure 1.10:*** *ABPCI setup. The rocking curve represents the reflection intensity of the main beam versus crystal angle, the peak of the curve corresponds to the Bragg angle, $\theta_B$, [75]*

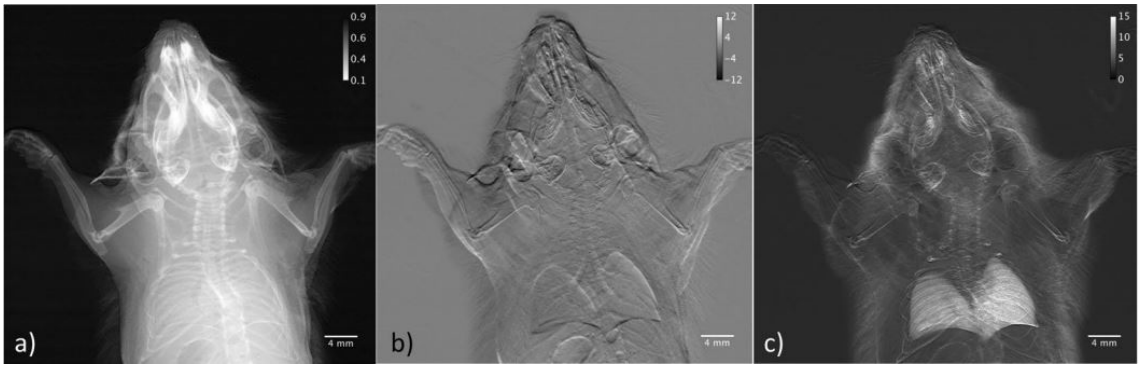


***Figure 1.11:*** *ABPCI Images of a mouse: (a) absorption based image, (b) refraction image, (c) scattering dark field image [78]*

ing creates X-ray beam diffraction, resulting in interference patterns which evolve with propagation distance. These patterns repeat at integer multiples of the Talbot distance [57],

$$z_{Talbot} = \frac{2T^2}{\lambda}, \tag{1.28}$$

from the absorption grating. In Equation 1.28, $T$ is the period of the grating and $\lambda$ is the wavelength of the radiation (where $\lambda \ll T$). The Talbot distance is not appreciably altered for X-rays of slightly differing wavelength [57]. As a result, this effect is still apparent using a limited bandwidth, polychromatic X-ray source. The Talbot effect is also apparent with a phase grating which alters the phase, rather than the intensity, of the X-ray wave field. In the case of a phase grating which introduces a phase shift of $\pi$, a rectangular intensity pattern of $T/2$ pattern is observed at the following Talbot lengths [57]:

$$z_{Talbot} = (n - 0.5)\frac{T^2}{4\lambda}, \tag{1.29}$$

where $n = 1, 2, 3, etc.$ The Grating Interferometry technique involves irradiating an

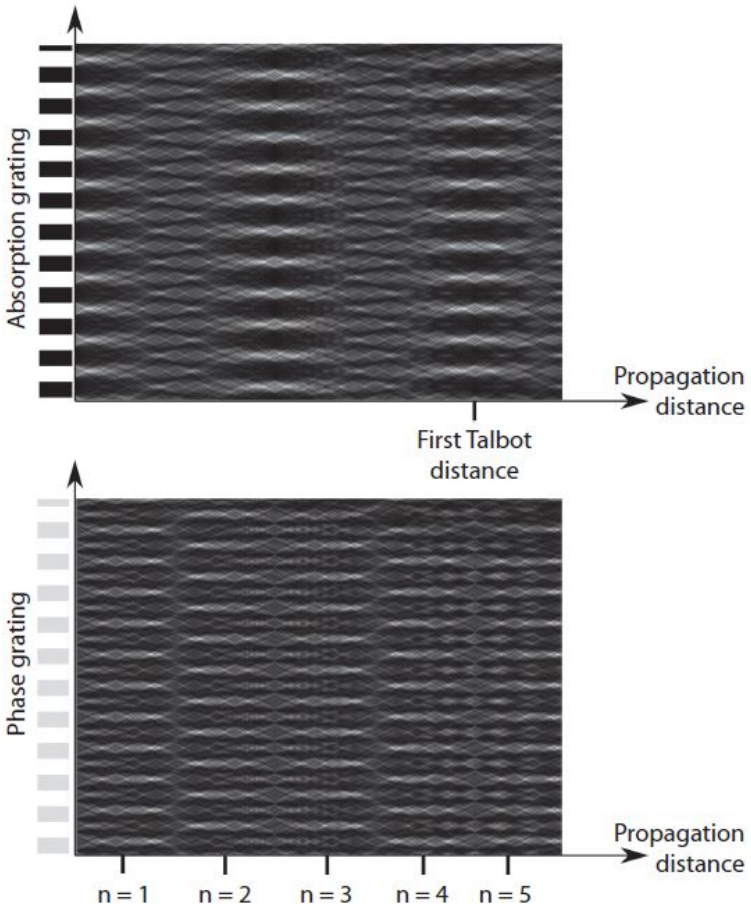


***Figure 1.12:*** *Interference pattern following X-ray diffraction due to an absorption grating (top) and phase grating (bottom) [57].*

object with highly spatially coherent X-rays and analysing the X-ray wave field transmitted through the object with a pair of gratings [68]. The first grating, $G_1$, is placed either in front of or behind the object. This phase grating introduces a periodic phase shift. The second grating, $G_2$, is placed after $G_1$ at one of the fractional Talbot distances (see Figure 1.13). At the fractional Talbot distances, the interference fringes created by the phase grating produce the "self-imaging effect". The technique can be extended to X-ray tubes with low spatial coherence by the use of a third grating ("Grating 0" in Figure 1.13) placed in front of the phase grating. The additional grating, however, reduces intensity, thus necessitating longer exposure times. Phase-contrast in one-dimension using line gratings can be achieved using the method described in [80] and shown in Figure 1.13. To create a pattern which has a period of T at $G_2$, the phase grating $G_1$ must have a period of 2T, twice the period of $G_2$ [57] [80]. During image acquisition, in a process called phase stepping, $G_2$ is incrementally stepped through a full period of the grating along the direction indicated by the phase stepping arrow ($x_g$) in Figure 1.13. Several images are acquired at different points throughout this cycle. The intensity signal, $I(x, y)$ in each pixel $(x, y)$ in the detector plane oscillates as a function of $x_g$ as shown in the phase stepping curve of Figure 1.14 (e). The phase differences $\phi(x, y)$ of the intensity oscillations in each pixel (Figure 1.14 (f)) are related to the wave front phase profile $\Phi(x, y)$, the X-ray wavelength $\lambda$, the

distance $d$ between the two gratings, and the period $g_2$ of the absorption grating by [80] [81]:

$$\phi = \frac{\lambda d}{g_2} \frac{\partial \Phi}{\partial x}. \tag{1.30}$$

The phase profile (Figure 1.14 (g)) of the object can thus be retrieved from $\phi(x, y)$ by a simple one-dimensional integration [80].

The phase stepping image acquisition process is now described. Consider three discreet positions of $G_2$ which give rise to absorption, dark field, and phase-gradient images respectively. In the first position, the grating $G_2$ is aligned with the phase grating intensity pattern such that the high intensity regions of the pattern pass through the gaps in $G_2$, resulting in maximum intensity at the detector in the absence of an object (position $x_3$ in Figure 1.14). When an object is introduced, refraction and scattering lead to shifts in the high intensity regions of the pattern. These shifts result in the high intensity regions no longer aligning with the gaps, and so are absorbed by the grating producing reduced intensity at the detector. With the grating in this position, an image resembling an absorption-based image with edge enhancement is generated, similar to that shown in Figure 1.14 (c). If $G_2$ is now moved to a position where the high intensity regions of the interference pattern align with the grating lines and are absorbed, minimum intensity will be recorded at the detector in the absence of an object (position $x_1$ of Figure 1.14). With the addition of an object, refraction and scattering will result in the high intensity regions shifting into the gaps of $G_2$, creating high intensity regions which correspond to small scale features at the detector. A dark field image similar to the one shown in Figure 1.14 (a) will result. When $G_2$ is positioned halfway between the previous two positions, the grating lines will partially absorb the high intensity regions of the interference pattern, resulting in medium intensity at the detector in the absence of an object (position $x_2$ or $x_4$ in Figure 1.14). Adding an object produces refraction in one direction resulting in the movement of the high intensity regions into the gaps of $G_2$ and subsequent increased intensity at the detector. Refraction in the opposite direction causes the high intensity regions to move over the grating lines of $G_2$ leading to absorption with a subsequent decrease in intensity at the detector. A phase-gradient image similar to that shown in Figure 1.14 (b) or (d) results. Grating Interferometry methods produce similar images to ABPCI methods, with phase-contrast being proportional to the first derivative of the phase shift. A significant advantage of the Grating Interferometry method is the ability to utilise X-ray fields with low spatial and temporal coherence [82]. This introduces the possibility of clinical implementation with conventional X-ray tubes.

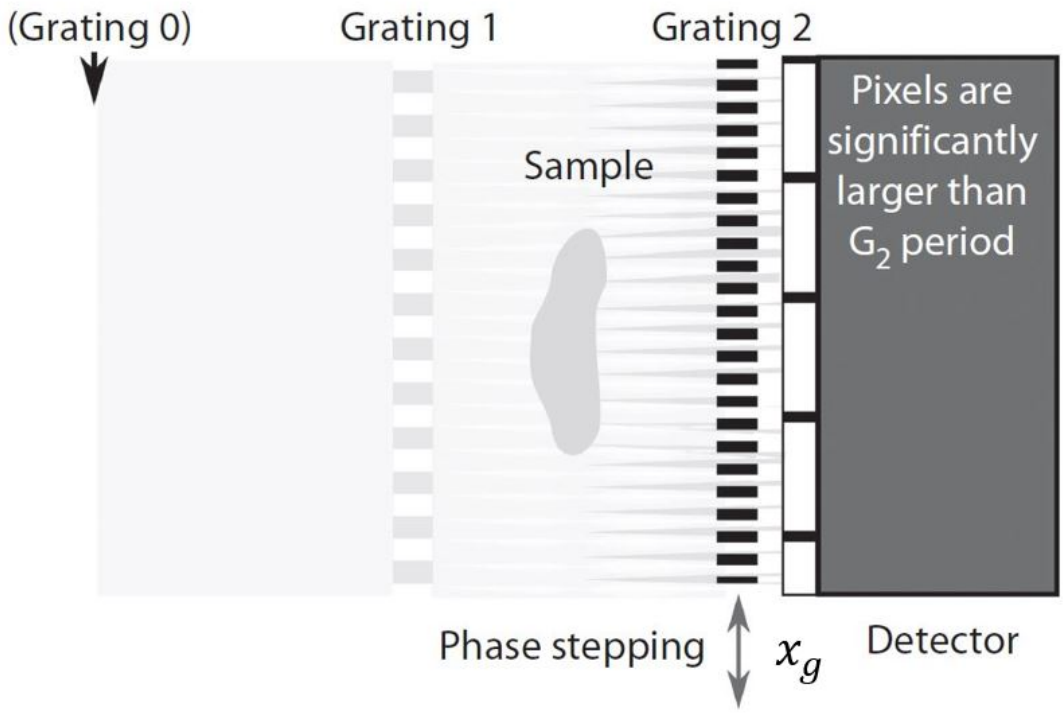


***Figure 1.13:*** *Grating based interferometry setup for a synchrotron X-ray source. A grating, "Grating 0" can be added for a laboratory X-ray source such as an X-ray tube [57].*

### 1.8.5 Edge Illumination Methods

The edge illumination method was initially developed as a synchrotron-based X-ray phase-contrast procedure in the late 1990s [75]. A synchrotron edge illumination technique is illustrated in Figure 1.15. A well collimated, monochromatic synchrotron X-ray beam is shaped by an aperture placed before the sample to produce a narrow beam of radiation. The beam is analysed by a second aperture positioned next to the detector. A function of detected intensity versus the relative displacement between the sample and the detector aperture is defined as the illumination function (Figure 1.15 (b)). When the system is aligned such that half of the X-ray beamlet impinges on the edge of the detector aperture, a shift of the X-ray beam by refraction is detected as intensity modulation by the analyser. The concepts applicable to a synchrotron source have been replicated for a laboratory source using the technique illustrated in Figure 1.15 (c) as demonstrated by Olivo *et al.* (2007) [83]. The method produces phase-contrast which is proportional to the derivative of the phase shift.

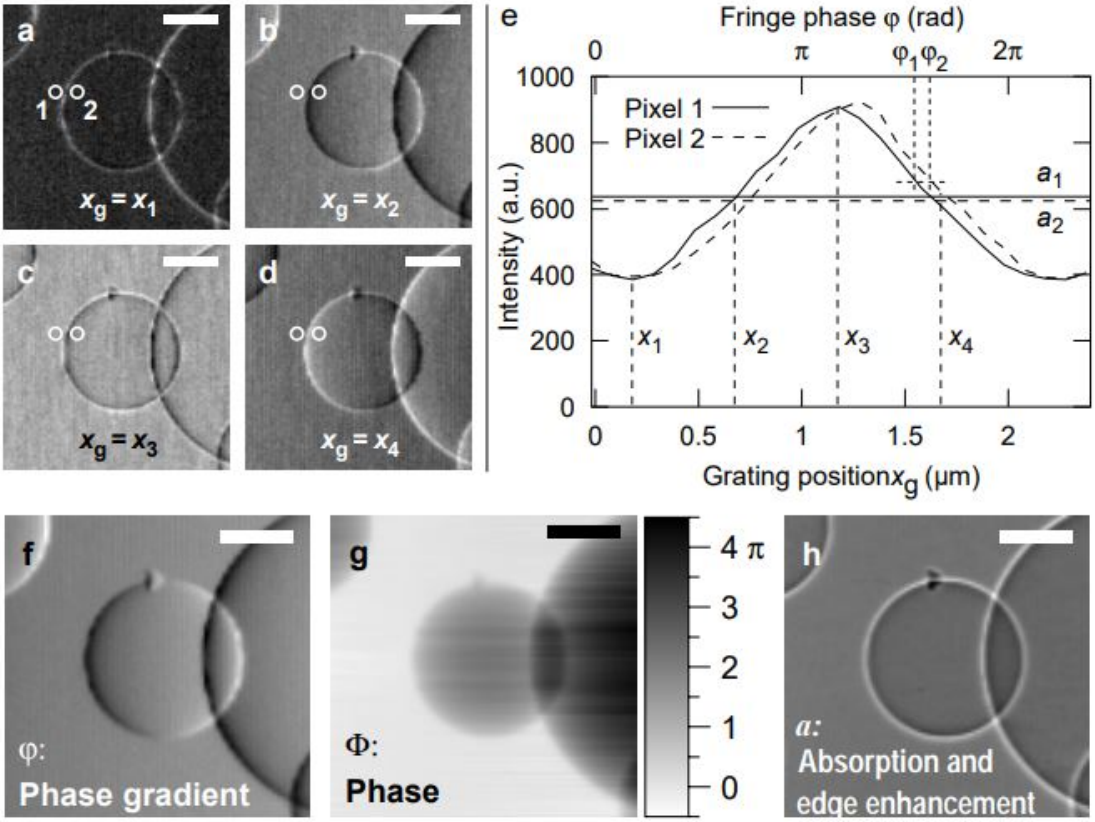


***Figure 1.14:*** *The principle of phase stepping. Images of polystyrene spheres (100 and 200 μm) acquired at different positions $x_g = x_1, ..., x_4$ of the absorption grating (a-d). (e) Phase stepping curve showing intensity oscillation in two different detector pixels i=1,2, as a function of $x_g$. Note that due to the position of pixel 1 outside the sample, the corresponding curve (shown in solid black) is equivalent to having no sample in the interferometer. For each pixel, the oscillation phase, $\phi$, and average intensity, a, can be determined. (f) Image of the oscillation phase, $\phi$, for all pixels. (g) Wave front phase, $\Phi$, retrieved from $\phi$ by integration. (h) Image of the average intensity a for all pixels, equivalent to a non-interferometric image. The length of the scale bar is 50 μm [80]*

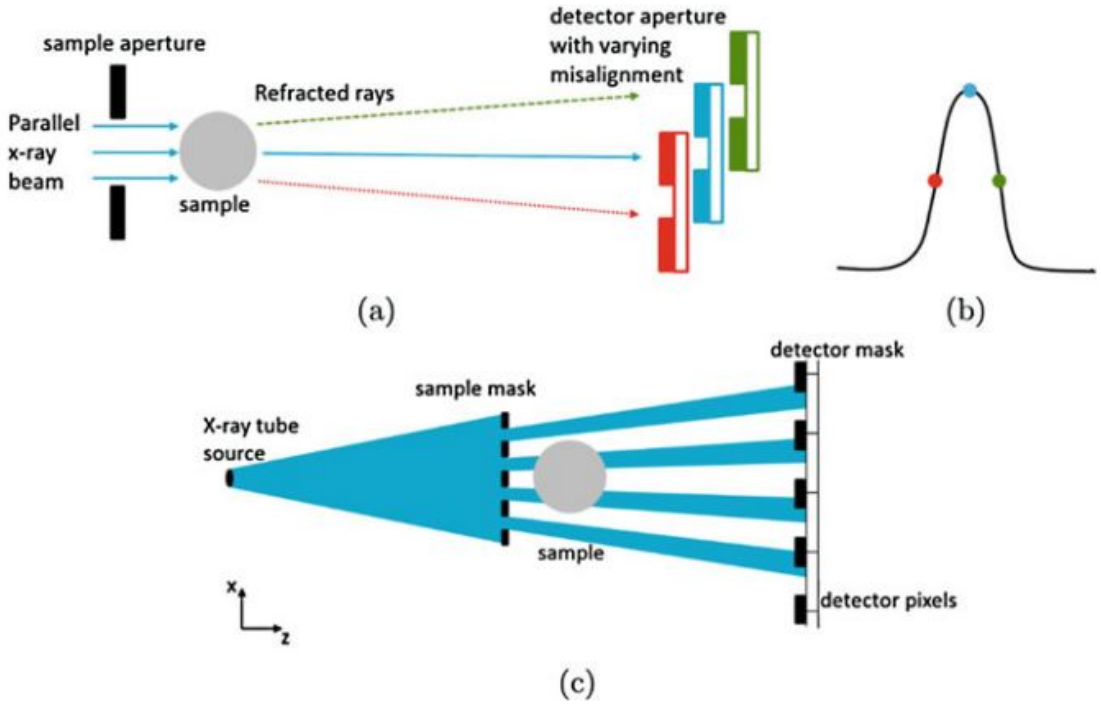


***Figure 1.15:*** *(a) Edge illumination setup, (b) illumination function (c) laboratory X-ray source implementation [75]*

## 1.9 X-ray Image Detection

X-ray image detectors record intensity variations over a 2D plane to form an image. The detectors convert the energy transported by X-ray photons into a form which can be recognised either visually or electronically. PBPCI utilises information encoded in Fresnel fringes to reduce radiation dose. To resolve fine Fresnel fringes, the detector must have sufficient spatial resolution [84]. Image detection in mammography has evolved over the years from screen-film to CR and then DR. Screen-film detectors have been described previously in Section 1.3.1. In the remainder of this section, CR and DR detectors are further discussed with an emphasis on phase-contrast mammography techniques.

### 1.9.1 Computed Radiography

CR is a technique used to produce digital mammographic images [15]. CR was an interim measure before converting to full DR systems in mammography. Photostimulable Storage Phosphor (PSP) plates replaced film. The cassettes housing the PSP plates had the same format as screen-film cassettes so could be used in existing machines that previously used screen-film. A latent image of trapped, excited electrons is formed within the storage phosphor upon exposure to X-rays. Once exposed, the imaging plate is placed in a CR reader which converts the latent image into a digital image through luminescence stimulated by a scanning laser beam. The plate is then erased using white light to eliminate any residual trapped electrons prior to the next use [15].

### 1.9.2 Charge-Coupled Device Detectors

Charge-Coupled Device (CCD) detectors convert visible light to an electronic signal which ultimately displays as a 2D image [15]. CCD detectors cannot detect X-rays directly, so the energy must first be converted to visible light using intensifying screens. Intensifying screens comprise a scintillating material (such as CsI) which absorbs X-ray photons and converts their energy into visible light photons through the conservation of energy. The visible light photons tend to propagate laterally in the scintillator material and are absorbed by several detector elements resulting in reduced spatial resolution [15]. CCD chips are an integrating type of detector composed of crystalline silicon. The photosensitive silicon surface of the CCD is divided into an array of discrete detector elements. Light is absorbed by the photosensitive silicon, resulting in liberation of electrons and a build-up of charge in each detector element. The charge is proportional to the intensity of light incident on each element. After exposure, the accumulated charge in each detector element is read out sequentially along rows of the CCD chip. CCD chips are often much smaller than the required field of view of the X-ray detector, necessitating that the light emitted from the large area of the intensifying screen be focused onto the small area of the CCD chip [15]. Due to lens coupling inefficiencies, a significant number of light photons is lost, resulting in decreased DQE and increased image noise [12].

### 1.9.3 Complementary Metal-Oxide Semiconductor Detectors

Complementary Metal-Oxide Semiconductor (CMOS) detectors convert visible light into an electronic signal and so are an alternative to CCD detectors [15]. CMOS detectors are composed of a crystalline silicon matrix with integrated photosensitive detectors, storage capacitors and read-out electronics. CMOS chips have the ability to address any detector element in read or read-and-erase mode. This allows opportunities for AEC, which is an advantage compared to CCD chips [15]. CMOS-based detector systems have inherently high electronic noise in both acquisition and readout states. These types of detectors are used for small field of view applications, and sometimes to replace image intensifier systems in fluoroscopy [12].

### 1.9.4 Flat Panel Thin Film Transistor Array Detectors

Thin Film Transistor (TFT) technology, originally developed for use in laptop computer screens, enabled the manufacture of large-area detector panels [15]. TFT technology eliminated the requirement for optical lens coupling to an intensifying screen, as in the case of CCD and CMOS detector systems. This resulted in improved DQE. TFT arrays are divided into individual detector elements which are arranged in a 2D matrix. Each detector element contains a TFT, a charge collecting electrode and a storage capacitor [15]. During X-ray exposure the TFT switch is closed, thus allowing the charge collected by the electrode to accumulate in the storage capacitor. During readout, the TFT array is activated one row at a time, by sequentially turning on the gate line to every detector element in the row. The charge in each detector element flows through the transistor to a drain line and on to a charge amplifier. The charge is amplified before converting it to a proportional voltage. The voltage signal is then digitised and represented as a pixel value for each detector element. This process is repeated row by row to fully convert the array into a 2D image. Two types of detector systems employ TFT technology: indirect and direct. Indirect systems use phosphor screens composed of either Cesium iodide (CsI) or gadolinium oxysulfide (GOS), to convert X-ray energy into visible light before detection by a photosensitive element on the TFT array. Direct systems use a semiconductor material, amorphous selenium (*a*-Se), which absorbs X-ray photons to create electron-hole pairs. An applied voltage across the semiconductor layer causes the electrons to move to the detector elements where they are stored as charge. An advantage of direct systems is high spatial resolution, as the applied voltage across the semiconductor reduces lateral spread of charges. Indirect systems suffer from lower spatial resolution due to lateral spreading of the light photons in the phosphor layer causing blurring. A disadvantage of direct systems in general radiography is the reduced DQE due to the low atomic number of *a*-Se compared to indirect systems. By comparison, the high atomic number of the CsI phosphor in indirect systems provides high detective quantum efficiencies in general radiography applications [15]. Direct conversion TFT flat panel detectors are commonly used in mammography where high spatial resolution is required and the low energy X-rays can be efficiently detected by the *a*-Se semiconductor layer [18].

### 1.9.5 Photon Counting Detectors

Photon counting detectors interact with photons individually, registering each photon electronically as a 'count' [12]. Energy resolving photon counting detectors can determine the energy of each photon based on the voltage pulse height associated with each count [84]. The advantage of photon counting detectors, compared to integrating detectors, is their ability to detect low exposure rates with significantly reduced noise levels [12]. Energy discrimination allows materials to be differentiated more effectively in computed tomography (CT) applications where the detector can characterise the manner in which different X-ray wavelengths are attenuated [85]. The disadvantages of photon counting detectors are: limitations on pixel size (>50 $\mu$m) and high cost [84].

## 1.10 Phase Retrieval

PCI techniques involve the use of X-ray detectors which cannot directly measure the phase shift of an X-ray wave field after interaction with an object. The only measurable quantity of the X-ray wave field is the intensity distribution. As shown by the TIE (Equation 1.24), the X-ray field phase shifts, caused by interaction with an object, result in variations of intensity which are dependent on propagation distance. In the case of PBPCI, these variations in intensity can be visualised as the characteristic Fresnel fringes which result in edge enhancement. The Fresnel fringes help visualise subtle changes in thickness or density between materials but do not directly yield information about the object. The Fresnel fringes can, therefore, be considered an aberration, meaning the object is not depicted correctly by the image. Information on the phase shifts and thus, information on the object, can be recovered through a process called phase retrieval. Phase retrieval unlocks the significant image quality benefits of PCI, allowing increased SNR for a lower radiation dose, compared to absorption-based images [86].

### 1.10.1 Transport of Intensity Homogeneous Phase Retrieval

In this section, an algorithm is derived which allows quantitative phase extraction from a single propagation-based phase-contrast image. This algorithm provides the thickness of a single material sample projected along the $z$-direction, $T(x, y)$, using information from both the phase-shift and the attenuation of the X-ray wave field. The algorithm relies on knowledge of the complex refractive index of the material, the input intensity and the intensity distribution of the phase-contrast image, as measured by the detector. It does not rely on measurement of the phase-shifts of the X-ray wave field, which cannot be directly measured. The Paganin *et al.* (2002) [87] method is described below:

Figure 1.16 shows a PBPCI layout with a point source. It is assumed that the scalar X-ray field is a paraxial and monochromatic. The TIE, which describes the intensity variation due to phase shifts with propagation distance, can be solved for the projected thickness $T(x, y)$ of the object. To simplify the derivation, the X-ray point source is assumed to be an infinite distance from the object ($R_1 \to \infty$). This assumption results in

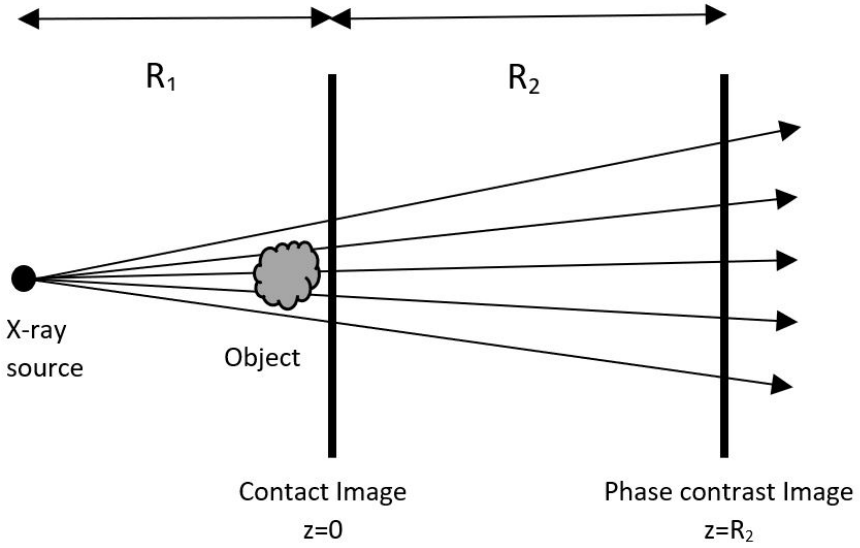


***Figure 1.16:*** *Propagation based phase-contrast imaging setup using a point source (not to scale). Adapted from [87]*

collimated illumination and a magnification factor of unity. The object is assumed to be composed of a homogeneous material. For X-ray radiation of uniform intensity over the area occupied by the object, the intensity at the exit surface ($z$=0) of the object, i.e. the contact image, is assumed to be approximated by Beer's Law of attenuation (Equation 1.20).

$$I(x, y, z = 0) = I_{in} \exp\left(-\mu T(x, y)\right).$$

The image at the plane $z = 0$ is equivalent to a conventional attenuation-based X-ray image. If the object is sufficiently thin, the phase-shift, $\Delta\phi(x, y, z = 0)$, of the illuminating beam at the exit surface of the homogeneous object is proportional to the projected thickness as shown by Equation 1.18:

$$\Delta\phi(x, y, z = 0) = -k\delta T(x, y).$$

Substituting the homogeneous Beer's Law Equation (1.20) and Equation 1.18 into Equation 1.26 gives an equation which is non-linear in $T(x, y)$, but can be written as an equation which is linear in $\exp\left(-\mu T(x, y)\right)$:

$$\left(-\frac{R_2\delta}{\mu}\nabla_\perp^2 + 1\right) \exp\left(-\mu T(x, y)\right) = \frac{I(x, y, z = R_2)}{I_{in}}. \tag{1.31}$$

The following identity has been utilised:

$$\delta\nabla_\perp \cdot \left(\exp\left(-\mu T(x, y)\right)\nabla_\perp T(x, y)\right) = -\frac{\delta}{\mu}\nabla_\perp^2 \exp\left(-\mu T(x, y)\right). \tag{1.32}$$

In order to proceed, the contact image, $I(x, y, z = 0) = I_{in} \exp\left(-\mu T(x, y)\right)$, and the phase-contrast image, $I(x, y, z = R_2)$ are represented by the following Fourier integrals:

$$I_{in}\exp\left(-\mu T(x,y)\right) = I_{in}\int\int \mathcal{F}\{\exp\left(-\mu T(x,y)\right)\}\exp\left(i2\pi(ux+vy)\right)dudv, \tag{1.33}$$

$$I(x,y,z=R_2) = \int\int \mathcal{F}\{I(x,y,z=R_2)\}\exp\left(i2\pi(ux+vy)\right)dudv. \tag{1.34}$$

In the expressions above, $\mathcal{F}\{\}$ is the Fourier transfrom. These can be substituted into Equation 1.31 and rearranged, recalling that $\mu = 2k\beta = 4\pi\beta/\lambda$, to give:

$$\mathcal{F}\{\exp\left(-\mu T(x,y)\right)\} = \frac{\mathcal{F}\{I(x,y,z=R_2)\}/I_{in}}{R_2\pi\lambda(\delta/\beta)(u^2+v^2)+1}. \tag{1.35}$$

Taking the inverse Fourier transform of the previous equation and solving for $T(x,y)$, the final algorithm is:

$$T(x,y) = -\frac{1}{\mu}\log_e\left(\mathcal{F}^{-1}\left\{\frac{\mathcal{F}\{I(x,y,z=R_2)\}/I_{in}}{R_2\pi\lambda(\delta/\beta)(u^2+v^2)+1}\right\}\right). \tag{1.36}$$

This is a well utilised relationship in PCI, known as Paganin's method [64]. In CT applications the homogeneous approximation can be considered valid within local areas [64]. This method can be implemented numerically, utilising the fast Fourier transform algorithm to significantly improve the SNR in propagation-based phase-contrast computed tomography (PB-CT). Nesterets *et al.* (2014) [86] demonstrated that a maximum theoretical SNR gain of $0.3(\delta/\beta)$ is possible using phase retrieval methods. With a $(\delta/\beta)$ ratio of approximately 870, as was used in the phase retrieval of PB-CT images of a mastectomy sample [59], a maximum theoretical SNR boost of 261, compared to an attenuation-based image, may be achieved. This significant boost in SNR arises from the utilisation of both attenuation and phase shift information of the X-ray field. The considerable increase in SNR could enable a reduction in radiation dose, while still maintaining adequate diagnostic image quality. Kitchen *et al.* [88] demonstrated that, with a 300 fold reduction in absorbed dose, the phase retrieved phase-contrast image SNR was 9.6 ± 0.2 times greater than that from absorption contrast data when imaging soft tissues with PB-CT. Gureyev *et al.* (2014) [89] demonstrated a dose reduction of approximately 400 times, while maintaining adequate image quality using TIE-Hom phase retrieval on PB-CT images of breast tissue samples. These considerable reductions in absorbed dose may allow breast CT to be performed at doses which are acceptable for screening with a significant improvement in image quality [59] [90].

## 1.11 Computed Tomography

A major limitation of conventional projection radiography is that the three-dimensional volume of the human body is projected on to a two-dimensional image. This results in superposition of different tissues and significantly reduced visibility of areas of interest. De-

spite good spatial resolution in projection radiography images, there is poor low-contrast resolution in soft tissues. The limitations of projection radiography are particularly significant in mammography. CT is able to compute a single slice image, based on projection images taken at many different angles around the object. These slice images eliminate the problem of over- and underlying structures obscuring regions of interest. These advantages have led to increasing research into the clinical applications of dedicated breast CT. One of the primary limitations of breast CT imaging is the increased dose to the patient. Breast phase-contrast CT imaging has the potential for significant reduction in dose compared to attenuation based CT, while maintaining acceptable SNR levels [90]. This modality is of particular interest for breast screening applications.

In CT scanners, the X-ray tube and detector, which are mounted within a gantry, rotate around the patient taking a series of one-dimensional (1D) projection images at different angles. These projection images are plotted on a two-dimensional (2D) Radon space image called a sinogram. The sinogram comprises rows, which correspond to different positions, $p$, on the 1D detector and columns, which correspond to projection angles, $\theta$, around the patient (Figure 1.17).

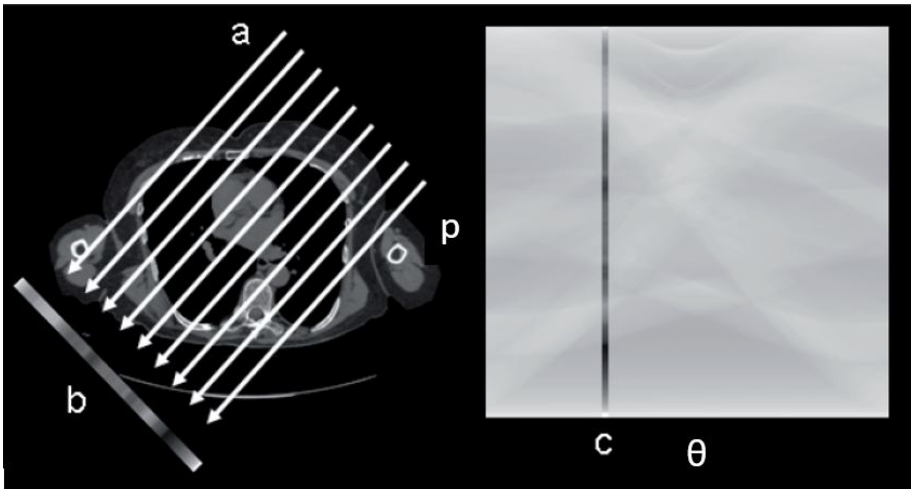


***Figure 1.17:*** *A specific projection angle (a) results in a 1D intensity image (b) which corresponds to one column in Radon space (sinogram) (c). Adapted from [12]*

The sinogram is then reconstructed into a slice image using one of several reconstruction methods.

### 1.11.1 Filtered Back Projection

Back projection is one of the simplest methods of forming a projection image from a sinogram. The method involves taking a 1D projection profile in the sinogram and distributing the measured signal, at the same angle as the projection, evenly over the object area. A slice image is formed by adding the back projections from all angles of every 1D profile. A limitation of simple back projection is the characteristic blurring as shown in Figure 1.18

(d). The blurring follows a 1/r intensity reduction around a feature in the image, where r is equal to the radial distance from the feature [15]. To correct the characteristic blurring, filtered back projection (FBP) is performed. The process of FBP involves performing a 2D Fourier transform on the sinogram image and applying a filter such as a ramp filter (shown as a Ram-lack filter in Figure 1.19) in Fourier space. The filtered Fourier space image is then converted back to a sinogram with the application of a 2D inverse Fourier transform. Finally, the filtered sinogram is back projected into a slice image that is free from characteristic blurring. Application of a ramp filter will correct for 1/r blurring but it results in excessive noise in the slice image due to gains in the high frequency region of Fourier space [15]. To reduce noise, a filter such as a Shepp-logan filter is applied [15]. The application of this filter results in a roll-off in the gain at the high frequency region of Fourier space. A further reduction in noise can be achieved by applying a Hann filter as shown in Figure 1.19 [15]. This filter significantly reduces gain in the high frequency region, but at the expense of spatial resolution [15].

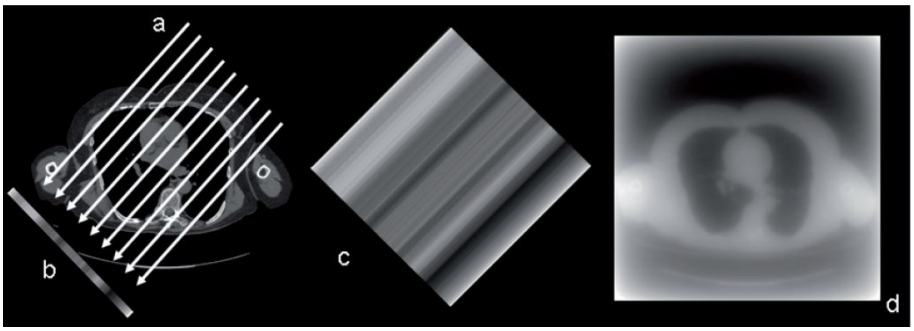


***Figure 1.18:*** *Simple back projection reconstruction. A specific projection (a) results in a 1D intensity image (b) which is back projected across the object area at the angle of the projection (c) The sum of many back projections results in a blurred slice image (d) [12].*

### 1.11.2 Iterative Reconstruction

With improvements in algorithm design and fast computer hardware, most modern scanners now offer iterative reconstruction methods as well as FBP [15]. The sinogram is known, whereas the slice image is unknown, in the reconstruction process. Iterative reconstruction algorithms begin with an initial estimate of the slice image. A forward projection is then performed. This forward projection can be considered as a type of simulated CT scan. The sinogram arising from the simulation is compared to the actual sinogram and an assessment of the match between the two sinograms is performed. If the profiles do not match within a given tolerance, then another iteration is performed. The iteration process is complete when the forward projected sinogram closely matches the actual sinogram. Following the completed iteration process, the slice image is a close approximation of the scanned object. Iterative reconstruction produces improved SNR images compared to FBP. Also, an equivalent SNR can be achieved with a lower radiation dose compared to FBP [15]. Nesterets *et al.* [91] (2015) investigated four iterative reconstruction methods applied to PB-CT acquisitions. The study concluded that all four

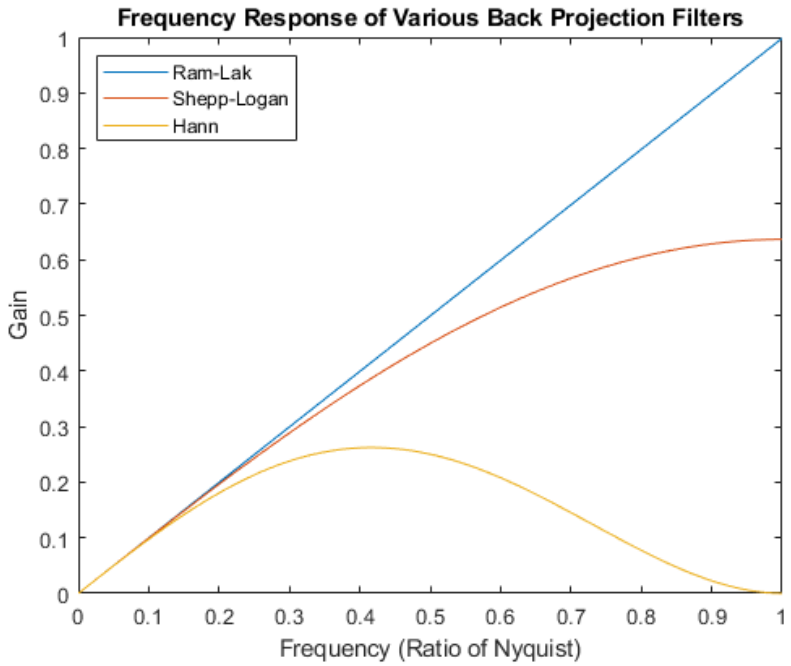


***Figure 1.19:*** *Different filters applied during filtered back projection reconstruction.*

reconstruction algorithms produced superior image quality metrics compared to FBP, with the Total Variation (X-TRACT 2015) algorithm providing the best overall improvement.

The slice images which result from these reconstruction methods commonly have pixel values that are represented by Hounsfield Units ($HU$). The HU scale represents the linear attenuation coefficient of the material ($\mu_{material}$) relative to the linear attenuation coefficient of water at room temperature ($\mu_{water}$):

$$HU = \frac{\mu_{material} - \mu_{water}}{\mu_{water}} \times 1000. \tag{1.37}$$

## 1.12 Image Quality Assessment

The purpose of imaging in breast cancer screening is to detect and characterise pathology. In this context, image quality is best defined in relation to diagnostic performance. The most effective descriptor of image quality is the receiver operating characteristics (ROC) curve, which is a quantitative method for assessing diagnostic performance [92]. It is often impractical to perform ROC studies to assess image quality because of the large number of images and significant observer time required. Often the only practical alternative is to use the subjective evaluation of clinical images by radiologists [93]. To have radiologists assessing large numbers of medical images can be uneconomical and impractical. It is beneficial, therefore, to establish a robust, quantitative image assessment method that can accurately predict the subjective clinical image quality assessment made by radiologists. This section presents further details on subjective clinical image quality assessment and introduces quantitative, image-based metrics which could potentially be used to predict

the clinical image quality assessment by radiologists. This section is based on a submitted paper (see Appendix B).

### 1.12.1 Clinical Image Quality Assessment

Clinical image quality assessment involves visually assessing the appearance of an image by a trained observer such as a radiologist. The radiologist will then provide an opinion on overall image quality. This method depends on human judgement and so is a subjective method of image quality assessment [93]. Clinical image quality assessment can be a side-by-side relative assessment, or an absolute assessment of image quality [94]. These two types of clinical image quality assessment can be referred to as relative or absolute visual grading analysis (VGA) studies [92]. Clinical image quality assessment suffers from intra- and inter-observer variability [93]. Furthermore, it cannot always be assumed that high clinical image quality leads to improved diagnostic performance [95]. Variability in clinical image quality assessments can be minimised by averaging assessments across many radiologists, giving the radiologists specific assessment instructions, and assessing images relative to a consistent reference image [96].

Taba *et al.* (2021) [97] subjectively compared overall image quality of mammographic phase-contrast CT images against attenuation-based CT images. The authors adopted a system of rating scores as follows: the overall clinical image quality of the phase-contrast CT image is clearly better than (+2); slightly better than (+1); equal to (0); slightly worse than (-1); and clearly worse than (-2) the overall image quality of the attenuation-based CT image. The authors of this study took measures to reduce variability between radiologists' scores. These measures included using a score averaged across 11 radiologists, performing a side-by-side relative comparison between phase-contrast and attenuation-based images, and giving the radiologists instructions on what aspects of image quality to focus on. Further details on this study are presented in Section 2.2

### 1.12.2 Physical Image Quality Assessment

Physical image quality assessment involves the computation of certain quantitative image criteria from greyscale values in the image. Physical assessment is independent of an observer assessing the image. However, subjective assessment by radiologists is more clinically relevant to achieving a diagnosis. Objective, physical image quality assessment methods, which accurately reflect overall image quality as assessed by radiologists, is still an active research area. The following sections describe various quantitative image metrics which may be used to form an objective model capable of predicting subjective clinical image quality.

### Contrast

Michelson contrast, also known as visibility [12], of an object indicates how easily the object is visually differentiated from the background. A CT image can be normalised so that the reconstructed pixel values correspond to the local value of the imaginary part, $\beta$, of the relative refraction coefficient. In this case, the contrast (C) can be calculated as [98],

$$C = \frac{\beta_{hi} - \beta_{low}}{2\beta_{aver}}, \tag{1.38}$$

where, in the case of breast CT images, $\beta_{hi}$ and $\beta_{low}$ are the average pixel values in the glandular and adipose regions respectively and $\beta_{aver}$ is the average of the pixel values across both the glandular and adipose regions.

### Signal to Noise Ratio

The SNR is a measure of the signal level in the presence of noise [15]. It is an important metric in mammography images as the visibility of low contrast soft tissue features, such as a tumour, is strongly dependent on the SNR of the image. A low SNR corresponds to poor visibility of low contrast features [12]. The SNR can be defined as [98]:

$$SNR = \frac{\beta_{aver}}{\sigma}, \tag{1.39}$$

where $\beta_{aver}$ is the mean output signal within a region of interest (ROI) and $\sigma$ is the standard deviation of the noise within the same ROI.

### Contrast to Noise Ratio

The contrast to noise ratio (CNR) is a measure of the signal difference (contrast) in the presence of noise. A definition of the CNR which is invariant with respect to affine pixel value transformations is [98],

$$CNR = \frac{\beta_{hi} - \beta_{low}}{2\sigma} = C \times SNR. \tag{1.40}$$

### Spatial Resolution

Spatial resolution is a metric used to quantify the ability of an imaging system to display two unique objects which are closely separated in space [12]. Spatial resolution is used to quantify the level of unsharpness in an image. Unsharpness or blurring in an image reduces the contrast of small objects. A high level of spatial resolution is required in mammography to visualise small micro-calcifications. The physical characteristics of an X-ray imaging system that affect spatial resolution include the size of the X-ray tube focal spot, the object to detector distance, the lateral spread of light photons in the phosphor layer of an indirect detector system and the pixel size of the detector.

There are several methods to quantify spatial resolution. The simplest method involves determining the limiting spatial resolution, which is defined as the maximum spatial frequency for which modulation is visually preserved. Limiting spatial resolution is quantified by acquiring an image of a line pattern phantom with a range of high contrast modulation patterns. The highest spatial frequency pattern which can just be visually resolved is the limiting spatial resolution. However, a simple descriptor of spatial resolution, such as the limiting spatial resolution, is often not sufficient to characterise it [92]. The measurement of the limiting spatial resolution by a line pattern phantom does not describe signal transfer at lower frequencies. Signal transfer at lower frequencies is in practice responsible for providing diagnostic information [99]. The modulation transfer function (MTF) provides a more complete description of the system spatial resolution. The MTF quantifies the degradation of the contrast of a system as a function of spatial frequency (Figure 1.20) [12]. The MTF of a digital system can be measured by first determining the edge spread function (ESF) of the system by imaging an attenuating object which presents a sharp edge [100]. The derivative of the ESF gives the line spread function (LSF) (shown in Figure 1.21). The LSF is then normalised so that the area under the curve is unity [15]:

$$\int_{x=-\infty}^{\infty} LSF(x)dx = 1. \tag{1.41}$$

Taking the Fourier transform and modulus of the normalised LSF results in a one-dimensional (1D) MTF [15]:

$$MTF(f) = |\mathcal{F}\{LSF(x)\}|, \tag{1.42}$$

where, $\mathcal{F}\{\}$ represents the Fourier transform. In many imaging systems, the point spread function (PSF) is assumed to be rotationally symmetric and spatially invariant (does not change with position in the image) [15]. The PSF is the response of the imaging system to a point, or impulse input [15]. Under these assumptions, the 1D MTF is sufficient to characterise the spatial resolution in any direction and any position in the image. Another measure used to quantify spatial resolution is the full width at half maximum (FWHM) of the system PSF. The FWHM is the width of the PSF function halfway between the maximum and minimum points. If the PSF is assumed to be rotationally symmetric, the LSF is a one-dimensional integral representation of the two-dimensional PSF [12]. Therefore, under most circumstances, with knowledge of one of the previously described spatial domain spread functions, the others (as well as the MTF) can be computed.

A method that determines the width of the PSF from the power spectrum of the noise in a uniformly illuminated area of a CT image is implemented in the X-TRACT software [86] [101]. A more detailed description of this method is provided in Section 2.3.1.

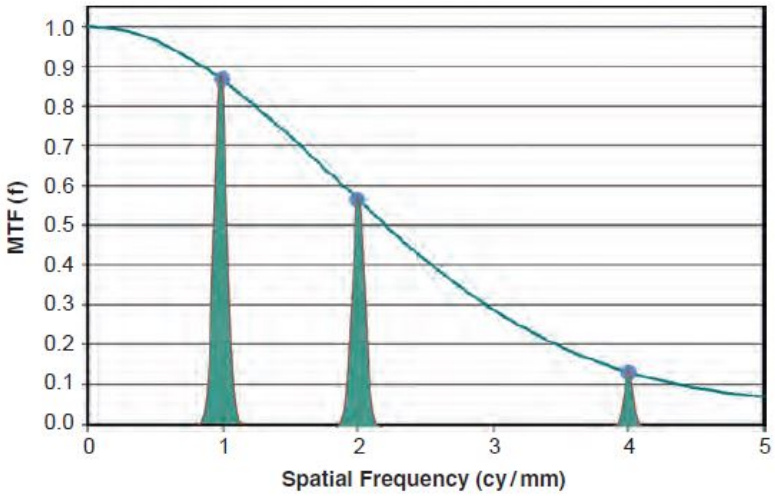


***Figure 1.20:*** *A plot of the MTF of an imaging system. Sinusoidal input signals are incident on the detector. The input signal with a spatial frequency of 1 cycle per millimetre (cy/mm) has diminished its input contrast to 87% by resolution losses in the imaging system. The input signals with spatial frequencies of 2 and 4 cy/mm have likewise been diminished to 56% and 13% of their input contrast, respectively. [15].*

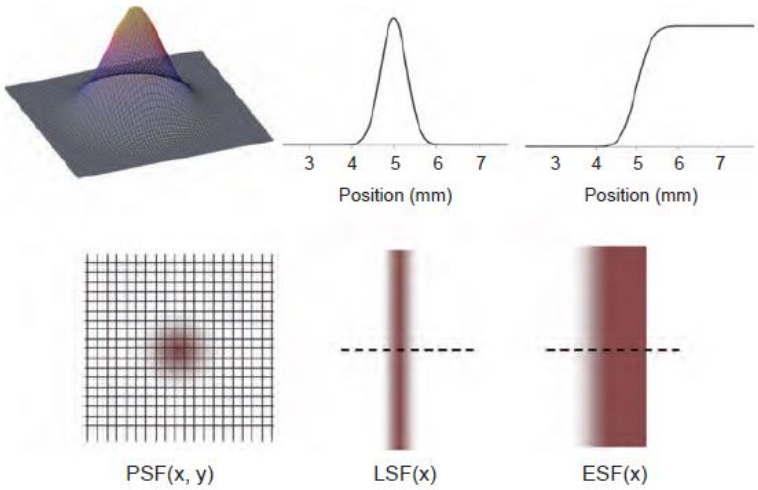


***Figure 1.21:*** *The spread functions in the spatial domain are shown. [15].*

#### Detective Quantum Efficiency and Noise Equivalent Quanta

The detective quantum efficiency (DQE) is used to characterise an X-ray imaging system in terms of the overall frequency-dependent SNR performance [15]. The DQE is commonly expressed in terms of spatial frequencies [12]:

$$DQE(u,v) = \frac{SNR^2_{out}(u,v)}{SNR^2_{in}(u,v)}, \tag{1.43}$$

where the subscript *out* is related to the output image and the subscript *in* corresponds to the incident X-ray flux.

The noise equivalent quanta (NEQ) is the effective number of quanta needed to achieve a specific SNR in an ideal detector [12]:

$$NEQ = SNR^2_{in}. \tag{1.44}$$

In some sense, the NEQ denotes the net worth of the image data in terms of X-ray quanta and the DQE defines the efficiency with which an imaging system converts X-ray quanta into image data [12].

#### Intrinsic Imaging Quality

Gureyev *et al.* [102, 103] proposed a measurement to assess the overall quality of an X-ray imaging system termed the "intrinsic imaging quality" ($Q_s$) characteristic (per single particle) of the imaging system. This is a dimensionless metric, incorporating both the noise sensitivity and spatial resolution of the system:

$$Q_s = \frac{SNR}{\Delta r I_{in}^{1/2}}. \tag{1.45}$$

In the equation above, $SNR$ is the average signal to noise ratio in a "flat" area of the image, $I_{in}$ is the mean incident intensity (i.e. the statistically averaged intensity distribution in the image), and $\Delta r$ is the standard deviation of the PSF (i.e. the spatial resolution).

### 1.12.3 Relationship Between Physical and Clinical Image Quality

Traditionally, quantitative image assessment has been performed using robust, intrinsic, objective quantities such as noise equivalent quanta NEQ or DQE, measured using simple phantoms [92]. Frequently, pathology detectability is not limited by system noise (such as quantum, structural and electronic noise), but by normal anatomic structure [92]. Metrics such as NEQ and DQE describe the imaging system but fail to describe the complex patient anatomy in clinical images. Recent studies have found a good correlation between DQE and subjective assessment of chest radiographs of an anthropomorphic phantom [104]. However, it remains difficult to predict clinical image quality using these metrics. Variable anatomical backgrounds significantly complicate the relationship be-

tween objective measures and subjective clinical image quality [92]. Several studies have demonstrated an image-based method that can successfully predict radiologists' perceptual rank ordering of chest radiograph images based on certain perceptual attributes (such as rib sharpness) [105, 106]. Given the complex anatomy present in chest radiography, a successful image-based predictive, objective measure of overall image quality has not yet been formulated. Promising results using no-reference image quality assessment models to predict subjective assessment of medical images has been demonstrated [107, 108]. However, these models have not been thoroughly verified against subjective image quality assessments performed by radiologists. Compared to many projection radiographs, thin-slice CT images of breasts have a relatively simple anatomical background. In thin-slice CT images of breasts, visibility of pathology is likely limited by system noise rather than the anatomical background. In this context, the likelihood of establishing a correlation between physical measurements and clinical image quality is improved.

# Chapter 2

# Experimental Methods

In 2018, 12 mastectomy samples were scanned using PB-CT techniques at the IMBL. This was part of a larger study of approximately 120 mastectomy samples scanned over approximately five years. For each of the 12 samples, eight different PB-CT image sets were collected using a variety of imaging parameters. Additionally, reference absorption-based computed tomography (AB-CT) images were also collected using a small object to detector distance for each sample. A recent study by Taba et al. [97] enrolled 11 specialist breast radiologists to assess the subjective clinical image quality of the PB-CT test images of the mastectomy samples against AB-CT reference images of the same mastectomy samples. The methods described in this section provide a quantitative, relative image assessment model which predicts the corresponding subjective assessments performed by a pool of radiologists. Two separate methods, using two different software programs for performing quantitative image measurements are described. This section uses material presented in a submitted paper (see Appendix B).

## 2.1 Samples and Imaging Technique

As described in Taba (2021) [97], 12 fresh mastectomy specimens were used. The samples were scanned within a few hours of surgical excision with no fixation or preservation applied. All scans for this study took place at the IMBL. A near-parallel X-ray beam with a cross-sectional area of approximately 120mm $\times$ 30mm and energies of 32 or 34 keV, with a monochromaticity ($\Delta E/E$) of about $10^{-3}$, was used, based on previous optimisation studies [109] [110]. The X-ray detector used was a Hamamatsu C10900D Flat Panel Sensor, with a pixel size of 100 $\mu$m $\times$ 100 $\mu$m, a field of view of 1248 $\times$ 1248 pixels and a frame rate of 17 fps. Each mastectomy sample was placed in a thin-walled ($\approx$ 1 mm) cylindrical plastic container, with a diameter of either 11 cm ($n$ = 11) or 12 cm ($n$ = 1), while the skin and nipple were positioned on the top. The surgical sutures and clips on the mastectomy specimens were used to orient the breast (resembling a coronal view) before positioning the container on a rotation stage for CT scans. Images were collected at two different sample-to-detector distances: the minimum practically achievable distance of 0.19 m was used to represent an AB-CT scan, and the maximum achievable distance

of 6 m was employed for PB-CT scans. An ionisation chamber was used to measure the photon fluence rate, and the corresponding rate of the surface absorbed dose to air at the ionisation chamber plane. The subsequent calculation of the mean glandular dose (MGD) was performed using Monte Carlo simulations, with a numerical phantom simulating the breast. The numerical phantom was composed of 30% weight glandular tissue and 70% weight adipose tissue [111] surrounded by a 5mm thick layer of adipose tissue (representing the skin). In this study, all the AB-CT images were collected at 4 mGy MGD ("standard" dose), while PB-CT scans were collected at two different doses of 4 mGy MGD ("standard" dose) and 2 mGy MGD ("low" dose). For each scan at 4 mGy, 2400 projections with 0.075° angular steps were collected over the 180° rotation range. Similarly, for the 2 mGy scans, 1200 projections with 0.15° angular steps were collected. Additionally, dark-current images (for removing the detector dark current contribution) and flat field images (for correcting uneven illumination) were collected during each acquisition. The CT reconstruction method used to produce the 3D images of the breast tissue was Filtered Back Projection (see Section 1.11.1). For PB-CT images, a phase retrieval technique was employed to exploit the refraction information in the transmitted X-ray beam by applying the Homogeneous Transport of Intensity Equation (TIE-Hom) algorithm to the collected projection data [87]. The TIE-Hom algorithm is a low-pass filter controlled by a single parameter $\gamma$. To perform phase retrieval that completely removes diffraction fringes at the boundary of two materials, the applied $\gamma$ value should be equal to the ratio of the real decrement ($\delta$) to the imaginary decrement ($\beta$) of the relative complex refractive index of these two materials ($\Delta\delta/\Delta\beta$). In general, by increasing $\gamma$, better SNR in the CT image can be achieved but with poorer spatial resolution. Similarly, by decreasing $\gamma$, poorer SNR in the CT image results but with better spatial resolution [86] [112]. In order to find an optimal balance between SNR and spatial resolution, each CT reconstruction was performed at two different levels of phase retrieval, i.e. two different values of $\gamma$. For "full phase retrieval," a $\Delta\delta/\Delta\beta$ value that depends on the X-ray energy and is close to the theoretical value for glandular tissue relative to blood (to mimic tumour; $\Delta\delta/\Delta\beta = 550$ for 32 keV and $\Delta\delta/\Delta\beta = 600$ for 34 keV) is used [60]. For "half phase retrieval" a $\Delta\delta/\Delta\beta$ value equal to half the value in full phase retrieval is applied. When comparing different X-ray energies (32 keV and 34 keV), the effect of phase-retrieval is controlled by including both half-phase retrieval (hTIE) and full-phase retrieval (fTIE) image sets (equal number of cases) in the assessment. Similarly, when comparing different levels of phase retrieval (hTIE and fTIE), both 32 keV and 34 keV image sets (equal number of cases) are included in the assessment, so the effect of X-ray energy on the quality scores is controlled.

## 2.2 Subjective Radiological Assessment

As described in Taba (2021) [97], the AB-CT and PB-CT slices were originally reconstructed in the plane corresponding to the coronal view in mammography. For the radiological assessments, the images were numerically re-sliced into axial and sagittal views, representing craniocaudal and mediolateral oblique views, respectively. Furthermore, while the original in-plane resolution of 100 $\mu$m was preserved, median values were used to gener-

ate thicker slices of 1mm each (close to the slice thickness in digital breast tomosynthesis) for assessments. The original AB-CT and PB-CT slices were in 32 bit greyscale with the reconstructed pixel values corresponding to the local value of the imaginary part, $\beta$, of the complex refractive index. For the radiological assessment, the images were converted to 8bit greyscale, where the pixel values have a value between 0 and 255, corresponding to the darkest and lightest greyscale shade, respectively. Before assessing the PB-CT images, the best quality AB-CT image set, among the corresponding 32 keV and 34 keV images sets, was selected by three medical imaging experts as the reference image set for each sample. A visual grading characteristics (VGC) study was conducted [113], in which radiological image quality was assessed in a blinded experiment by 11 radiologists with 5-20 years of experience in reporting mammography. The assessment included evaluating overall radiological image quality in PB-CT (test) images, prepared in axial and sagittal planes, compared with the corresponding AB-CT (reference) images using a five-point rating scale. The definition of the scale is; the image quality of the test image set is clearly better than (+2); slightly better than (+1); equal to (0); slightly worse than (-1); and clearly worse than (-2) the reference image set. The radiologists were asked to consider "perceptible contrast," "lesion sharpness," "normal tissue interfaces," "calcification visibility," "image noise," and "artefacts" when rating the overall radiological image quality.

## 2.3 Quantitative Assessment

It is hypothesised that the CNR to spatial resolution (res) ratio (CNR/res) is a quantitative metric that is likely to correlate with the overall clinical image quality as assessed by radiologists. The CNR/res criterion is closely related to the "intrinsic image quality" (Equation 1.45) proposed by Gureyev *et al.* [102, 103]. Furthermore, the CNR/res criterion is a metric that combines the three most fundamental factors affecting image quality: contrast, noise and spatial resolution [92]. To calculate the CNR/res, the contrast, noise, and spatial resolution measurements were performed on both the PB-CT (test) and the AB-CT (reference) images. Two methods for quantifying the contrast and SNR (as a measurement of noise) and three methods for calculating spatial resolution were implemented using two separate software programs.

### 2.3.1 X-TRACT Software

X-TRACT software [101] has been utilised in several studies relating to PB-CT image quality [50, 98, 109, 114]. In these studies, it has been utilised to perform measurements of contrast, SNR and spatial resolution.

The "Thick line" tool in X-TRACT ("T" in the Image Control dialogue) is able to calculate and report visibility (as a measure of contrast), SNR and spatial resolution. The "Thick line" tool is used to draw a rectangle across an interface between glandular and adipose tissue as shown in Figure 2.1. The contrast is calculated using Equation 1.38. In the X-TRACT software calculation, $\beta_{hi}$ and $\beta_{low}$ are the average pixel values inside

the top and bottom histogram bins, respectively, of a 5-bin histogram into which all pixel values from the selected "Thick line" (see red/white rectangle in Figure 2.1) region are sorted. $\beta_{aver}$ is the average pixel value inside the same "Thick line" selection area [98].

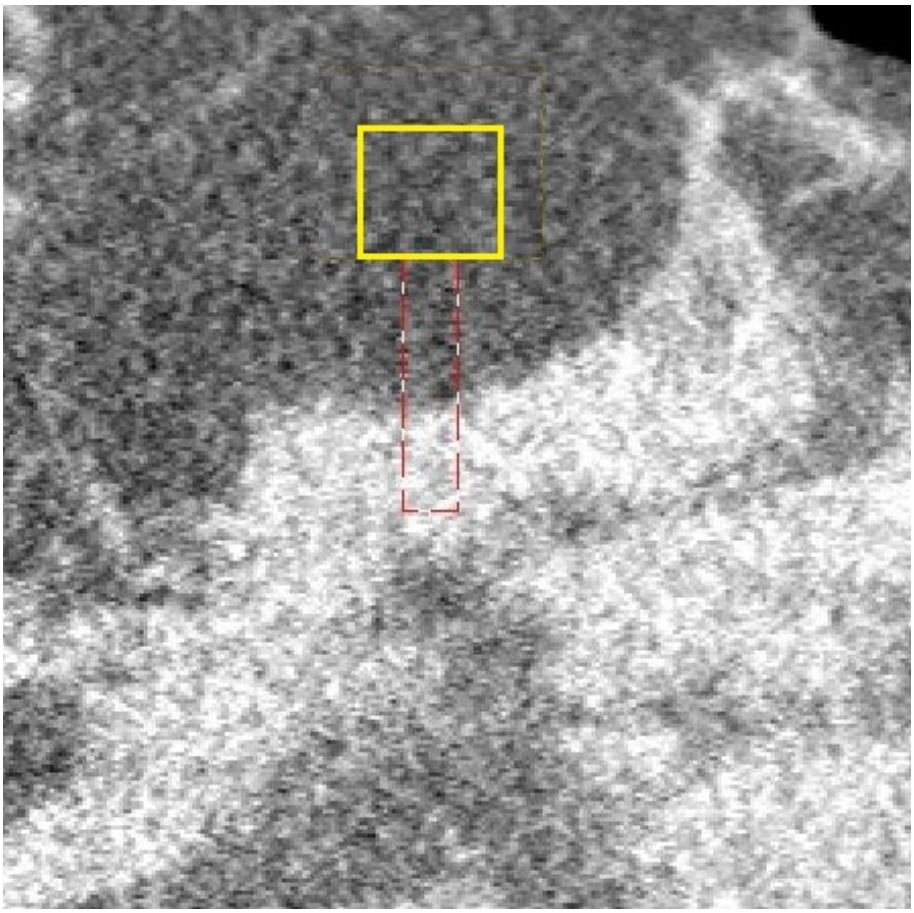

***Figure 2.1:*** *An example of the placement of the thick line tool in X-TRACT to measure the contrast between glandular and adipose tissue, the SNR and the spatial resolution in the image. The red/white rectangle indicates the shape of the thick line tool rectangle and the yellow square indicates the approximate location of the virtual square (not usually shown in X-TRACT).*

The SNR is calculated using both the "Thick line" area and the adjacent "virtual square" region (see yellow square in Figure 2.1) which should be located in a "flat" (featureless) area of the image to allow the evaluation of the photon statistics. This "virtual square" region is located immediately next to the left edge, in the case of a horizontal "Thick line", or next to the top edge in the case of a vertical "Thick line". The area of the "virtual square" region is equal to the area of the selected "Thick line" [115]. The SNR is defined as the ratio of the average pixel value in the thick line area to the standard deviation of the pixel values within the virtual square region (see Equation 1.39). Generally, the noise in medical images is not independent from one pixel to another. Therefore, the noise power spectrum (NPS) is usually required for full characterisation of the noise [92]. All images in this study are acquired using the same system setup, so the shape of the NPS stays approximately constant. Therefore, a simple measure of the pixel value

standard deviation is deemed adequate to compare noise between images.

The spatial resolution in X-TRACT is calculated from the power spectrum of the noise, which is defined as the difference between the value of intensity in a given pixel and the mean intensity value within the uniformly illuminated virtual square region [109]. It is assumed that the incident photon flux within the selected small uniformly illuminated area is spatially stationary, ergodic and has Poisson statistics [12]. Under these assumptions, it is possible to calculate the width ($\Delta r$) of the detector PSF by measuring the effective width of the power spectrum of the image noise. The input power spectrum of the incident quantum noise is uniform, indicating that it has the appearance of a flat line across all spatial frequencies. The output power spectrum of the noise, measured from the noise in the image, is a convolution of the input incident quantum noise with the detector PSF, phase retrieval and the CT reconstruction. This leads to the multiplication of the power spectrum by the square of the corresponding MTF [116]. Therefore, by calculating the power spectrum of the noise within the virtual square region (assuming it is placed on a uniformly illuminated region of the image) the width of the MTF can be determined. The width of the PSF, assuming it has a gaussian shape, can be calculated from the width of the MTF [109]. The spatial resolution of the imaging system (including all the post processing operations) is equated with the width of the PSF. This calculation accounts for the PSF of the detector, but not the X-ray source size (penumbral blurring) [50]. However, given the extended source-to-object distance in the synchrotron setup, the X-ray source size has a negligible contribution to blurring.

The CNR/res value is calculated using the contrast, SNR and spatial resolution ($\Delta r$) in the following equation and displayed in the X-TRACT Image Control dialogue:

$$CNR/res = \frac{C \times SNR}{\Delta r}. \tag{2.1}$$

To perform the measurements using the "Thick line" tool, the PB-CT (test) and corresponding AB-CT (reference) images were opened side by side. A suitable interface between glandular and adipose tissue was selected on the PB-CT image and a "Thick line" was drawn across the interface (an example of which is illustrated in Figure 2.1). The same interface was then located on the corresponding AB-CT image, and a "Thick line" of similar size and position was drawn. This method is intended to minimise errors introduced by comparing different anatomy or different parts of the image between the PB-CT (test) and AB-CT (reference) images. The PB-CT and AB-CT images come as a CT image set, so the "Thick line" tool is used to measure every tenth sagittal and axial slice of the reconstructed PB-CT and AB-CT image sets. For every tenth image, the calculated value of CNR, contrast and the CNR/res is read from the X-TRACT Image Control dialogue and recorded. With reference to Equation 2.1, the SNR can be calculated from both the CNR and contrast values given by X-TRACT. The spatial resolution can

likewise be calculated from the CNR and the CNR/res values given by X-TRACT. The final value for each metric is calculated from the average across all analysed slices (typically ten per CT image set) and across both the axial and sagittal image sets as illustrated in Figure 2.2.

| PCT-2370691-1-32keV-6m-2mGy-fTIE | | | | | |
|---|---|---|---|---|---|
| | | | | | |
| Axial | CNR | CNR/res | Visib | Res | SNR |
| Slice_010 | 2.067 | 1.302 | 0.425 | 1.588 | 4.864 |
| Slice_020 | 2.165 | 1.381 | 0.479 | 1.568 | 4.520 |
| Slice_030 | 2.307 | 1.442 | 0.387 | 1.600 | 5.961 |
| Slice_040 | 2.265 | 1.429 | 0.413 | 1.585 | 5.484 |
| Slice_050 | 2.246 | 1.435 | 0.421 | 1.565 | 5.335 |
| Slice_060 | 2.182 | 1.402 | 0.41 | 1.556 | 5.322 |
| Slice_070 | 2.393 | 1.5 | 0.433 | 1.595 | 5.527 |
| Slice_080 | 2.138 | 1.353 | 0.416 | 1.580 | 5.139 |
| Slice_090 | 1.94 | 1.246 | 0.372 | 1.557 | 5.215 |
| Slice_100 | 2.056 | 1.31 | 0.375 | 1.569 | 5.483 |
| | | | | | |
| Mean | 2.176 | 1.380 | 0.413 | 1.576 | 5.285 |
| | | | | | |
| Sagittal | CNR | CNR/res | Visib | Res | SNR |
| Slice_010 | 2.287 | 1.501 | 0.466 | 1.524 | 4.908 |
| Slice_020 | 2.276 | 1.439 | 0.418 | 1.582 | 5.445 |
| Slice_030 | 2.097 | 1.328 | 0.407 | 1.579 | 5.152 |
| Slice_040 | 2.301 | 1.441 | 0.42 | 1.597 | 5.479 |
| Slice_050 | 2.265 | 1.436 | 0.504 | 1.577 | 4.494 |
| Slice_060 | 2.649 | 1.704 | 0.476 | 1.555 | 5.565 |
| Slice_070 | 2.446 | 1.544 | 0.524 | 1.584 | 4.668 |
| Slice_080 | 1.981 | 1.235 | 0.414 | 1.604 | 4.785 |
| Slice_090 | 2.267 | 1.439 | 0.49 | 1.575 | 4.627 |
| Slice_100 | 2.119 | 1.348 | 0.385 | 1.572 | 5.504 |
| | | | | | |
| Mean | 2.269 | 1.442 | 0.450 | 1.575 | 5.063 |
| | | | | | |
| Overall Mean | 2.222 | 1.411 | 0.432 | 1.576 | 5.174 |

***Figure 2.2:*** *An example of the measurements performed on one PB-CT slice stack for patient number 2370691 which used an X-ray energy of 32 keV, a MGD of 2 mGy and full TIE phase retrieval. Using the "Thick line" tool, a measurement is performed on every tenth slice of both the axial and sagittal reconstructions. The bottom line shows the final values for each metric averaged across all measurements of both projections. The cells shaded with yellow indicate values which are recorded from the X-TRACT Image Control dialogue, while grey cells are values that are calculated in Microsoft Excel from the values shaded in yellow.*

### 2.3.2 3D Slicer Software

In addition to the measurements performed using X-TRACT software, an alternative software program, 3D Slicer (http://www.slicer.org) [117], was utilised to perform measurements of contrast, SNR and spatial resolution in both the PB-CT (test) and AB-CT (reference) images. 3D Slicer is an open-source software used for medical, biomedical and imaging-related research. Operations in the 3D Slicer software can be automated using

python scripts. For this study, custom python scripts were written to perform contrast, SNR and spatial resolution measurements on a set of CT images loaded as a 3D volume in 3D Slicer. The following sub-sections describe the method which was implemented using code to perform the previously described measurements.

### Contrast and Signal to Noise Ratio Calculation

The Digital Imaging and Communications in Medicine (DICOM) image sets were loaded into the 3D slicer software. The Segment Editor module was then used to create two different segments. One segment was used to highlight areas of glandular, nipple and cancerous tissue (as one segment, henceforth referred to as the "glandular segment"), and the other was used to highlight the adipose tissue. The "Paint" effect of the Segment Editor module was then used to firstly, paint areas of "glandular" tissue and secondly, areas of adipose tissue on every $10^{\text{th}}$ image in the image set as shown in Figure 2.3. The Segment Statistics module was then utilised to compute the mean pixel value (MPV) and standard deviation of the noise within the entire glandular (green segment) and adipose (yellow segment) regions throughout the image set. The contrast (also known as visibility or Michelson contrast using this definition [12]) was calculated using Equation 1.38, where $\beta_{hi}$ is the MPV in the glandular segment, $\beta_{low}$ is the MPV in the adipose segment and $\beta_{aver}$ is the average of the $\beta_{hi}$ and $\beta_{low}$ values. The SNR was defined as the ratio of the average pixel value in the adipose segment divided by the standard deviation of the pixel values in the adipose segment.

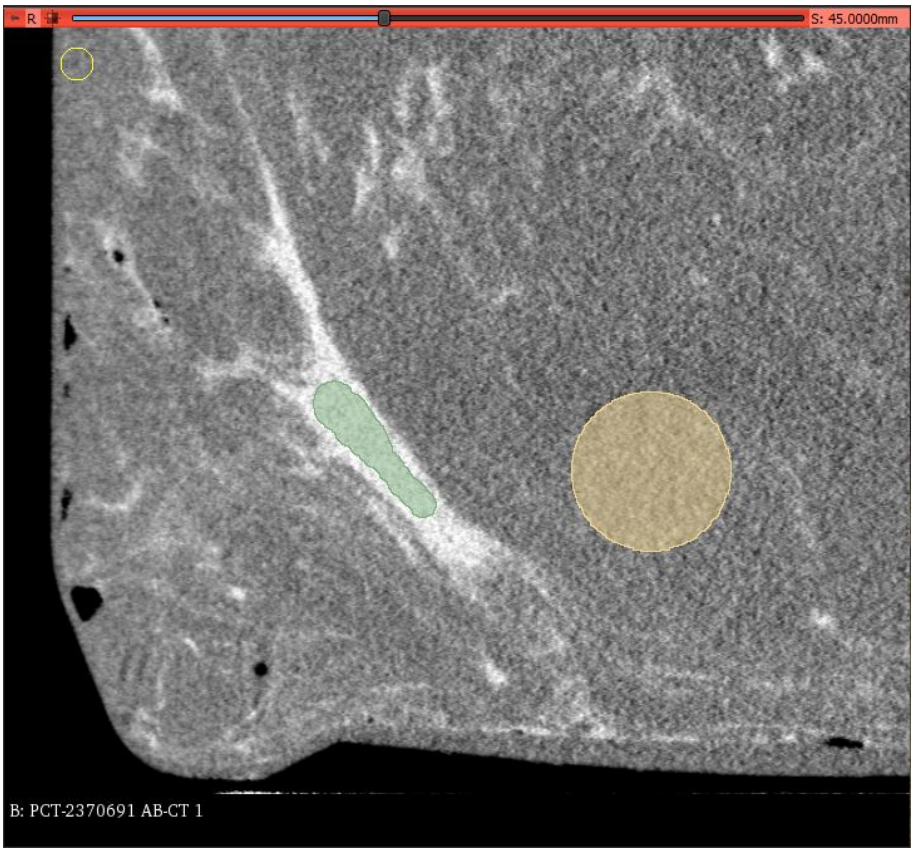


***Figure 2.3:*** *A magnified area of an AB-CT reference image. The green painted segment represents glandular tissue, and the yellow painted segment represents the background adipose tissue. Similar segments were painted on every 10th image of the CT image set.*

### Spatial Resolution Computation

The aim of this method was to calculate the spatial resolution of the PB-CT (test) image set relative to the AB-CT (reference) image set. This was achieved by establishing an image-based edge profile between adipose and glandular tissue, averaged over several features of several images throughout the image set. The derivative of the edge profile (or tissue, image-based ESF) was then computed to show a Line Spread Function (LSF). Assuming the LSF has a Gaussian shape, a Gaussian curve can be fitted to the LSF, and a FWHM then computed from the fitted Gaussian curve. The FWHM was used to quantify the spatial resolution of the CT image set.

The one-dimensional LSF is an integral representation of the two-dimensional PSF [12]. It is assumed that the two-dimensional PSF is rotationally symmetrical, therefore the standard deviation (which is proportional to the width) of the LSF is equivalent to the standard deviation of the PSF. The standard deviation of the LSF resulting from this method, $\sigma_{tot}$, includes contributions from both the PSF of the imaging system, $\sigma_{sys}$, and the physical width of the tissue interface itself, $\sigma_{obj}$, as described by the following equation [118]:

$$\sigma_{tot}^2 = \sigma_{obj}^2 + \sigma_{sys}^2. \tag{2.2}$$

When determining the width of the PSF of an X-ray imaging system, an image of a sharp-edged test object is acquired so that $\sigma_{obj}$ is effectively zero [100]. For the measurements performed in this study, the "edge" is the average of a large number of glandular/adipose interfaces within a breast CT image set. Therefore, this "edge" cannot be assumed to have a negligible width. Without knowledge of the "edge" width, the true system PSF width cannot be determined using this method. For this study, the FWHM of the PB-CT and the AB-CT image sets are used to calculate the ratio of the PB-CT spatial resolution relative to the AB-CT spatial resolution. The PB-CT and reference AB-CT images come from the same sample, so $\sigma_{obj}$ can be assumed to stay constant. While this method may not give an accurate estimate of the absolute spatial resolution of the system, it is intended to indicate the relative spatial resolution between the PB-CT and AB-CT images. Two different methods of computing an edge profile between the glandular and adipose tissue were implemented using the 3D Slicer software. The first method is designed to give the same result as averaging many line profiles placed along the direction of the steepest local gradient at many points along the tissue interface. This method gives a result closer to but, as previously explained, not equivalent to the absolute spatial resolution. This will be referred to as the "absolute" spatial resolution measurement method. The second method is intended to give an equivalent result to placing many "thick" (averaged across a number of pixels along the tissue interface direction) line profiles, placed approximately perpendicular to the edge, at many points along a tissue interface. Prior to phase-retrieval, PB-CT images have characteristic diffraction fringes present at tissue interfaces. Therefore, these images appear as though they have sharper edges (even after phase retrieval) compared to AB-CT images, despite having equivalent absolute spatial resolution (see Figure 2.4). This second method is designed to express more accurately how sharp the edge *appears* to an observer, given these unique properties of phase-contrast images. This method will be referred to as the "perceived" spatial resolution measurement method.

**"Absolute" Spatial Resolution Measurement**

Prior to the implementation of the "absolute" spatial resolution method, every 10th image in the CT stack is isolated. The isolated slice images are then segmented to separate the glandular regions using simple thresholding, as implemented in the "Threshold" effect of the Segment Editor module. The glandular tissue is segmented using a pixel value range from a minimum threshold value up to the highest pixel value in the image. The minimum threshold value used for this method is the average of the MPV in the glandular regions of the image set and the MPV of the adipose regions of the image set. Both have been previously calculated in the method to calculate contrast (shown in Figure 2.3). With the glandular tissue segmented, an island filter is applied to remove islands of noise smaller than 10 pixels in size. A fill holes filter with a kernel size of 2 pixels is then applied to fill small holes within the glandular segment. The final glandular segment is shown in green in Figure 2.5. The edges of the green glandular segment are then expanded outward by 3

pixels before being hollowed into a 1-pixel thick ring. The Segment Statistics module is then used to calculate and store a MPV of the ring-shaped segment. The original segment is then restored before repeating the previous steps. The segment is expanded by only 2 pixels, however. This process is repeated, expanding the segment by 1 less pixel each time. After the 4th iteration, the segment shrinks by increasing amounts rather than expanding. This approach ensures that throughout the steps, the ring-shaped segment maintains the general shape of the glandular/adipose edge. An illustration of the ring-shaped segments resulting from the first (green ring), fourth (yellow ring) and eighth (red ring) iterations are shown in Figure 2.6. At each iteration, the MPV of the pixels, highlighted by the ring-shaped segment, was recorded and subsequently plotted against the iteration number to show an ESF averaged across all glandular/adipose interfaces in the image. This averaging allows the computation of an ESF with greatly reduced noise levels compared to a traditional line profile plot. The derivative of the ESF is then calculated and plotted to show a LSF. A Gaussian curve is then fitted to the central 3 points of the LSF, and the FWHM of the Gaussian curve is used to measure the "absolute" spatial resolution.

**"Perceived" Spatial Resolution Measurement**

Prior to the "perceived" spatial resolution measurement, the glandular tissue throughout the entire volume was segmented. Simple thresholding, as implemented in the "Threshold" effect of the Segment Editor module, was used. The glandular tissue was segmented using a pixel value range from a minimum threshold value up to the maximum pixel value in the volume. For this method, the minimum threshold value was determined by eye, ensuring that the value was high enough to only segment the most solid glandular areas without including excess noise. With the glandular tissue segmented, an island filter is applied to remove islands of noise smaller than 20 pixels in size. A fill holes filter with a kernel size of 5 pixels is then applied to fill small holes within the glandular segment. The segment is then expanded in all directions by 8 pixels before being hollowed to form a 1-pixel thick ring as shown by the green ring in Figure 2.7. This hollow ring is then progressively reduced by 1 pixel at a time across the glandular/adipose interfaces. The original expansion of the segment smooths out the initial noisy or uneven edge, and subsequent iterations move the smoothed curve across the edge. At each iteration, the MPV was recorded and was subsequently plotted against the iteration number to show an ESF (see Figure 2.8). As described in the previous section, a Gaussian curve is fitted to the resulting LSF to arrive at a FWHM (which is generally wider than the FWHM determined using the "absolute" method). This is used as a measure of the "perceived" spatial resolution.

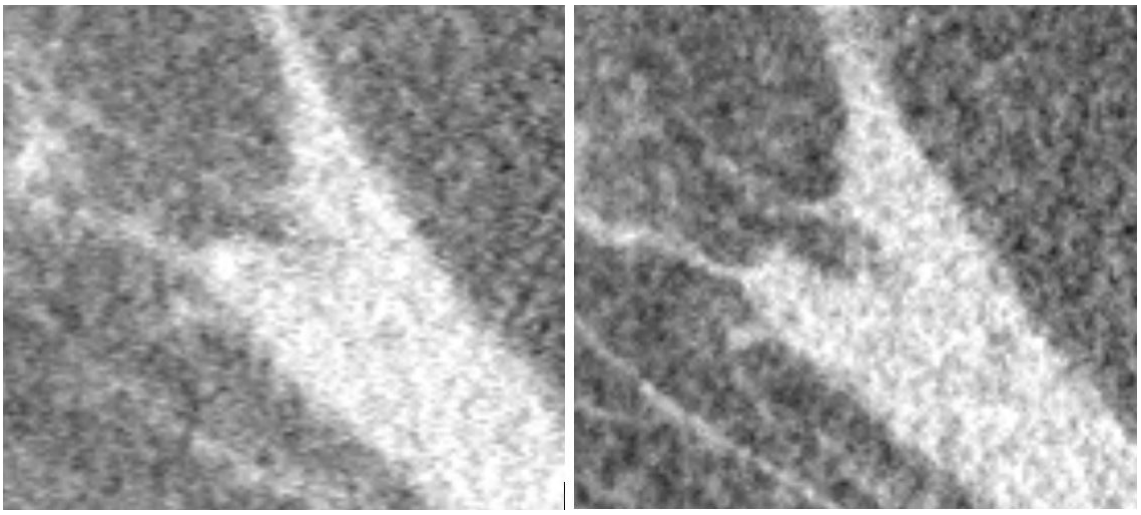

***Figure 2.4:*** *Comparison of a 32 keV, 4 mGy, hTIE PB-CT image (right) and the equivalent reference AB-CT image (left). The glandular/adipose interface of the PB-CT image (right) appears sharper than the equivalent AB-CT reference image (left). The X-TRACT method gives a spatial resolution ratio (PB-CT/AB-CT) of 1.02, and the "absolute" spatial resolution method (implemented in 3D Slicer) gives a ratio of 1.05, both indicating almost equivalent spatial resolution between the PB-CT and AB-CT images. The "perceived" spatial resolution method (implemented in 3D Slicer) gives a ratio of 1.80, indicating the PB-CT image has significantly sharper edges relative to the AB-CT image. This demonstrates that the "perceived" spatial resolution method potentially correlates more accurately with how the image appears to a human observer in the context of PB-CT images.*

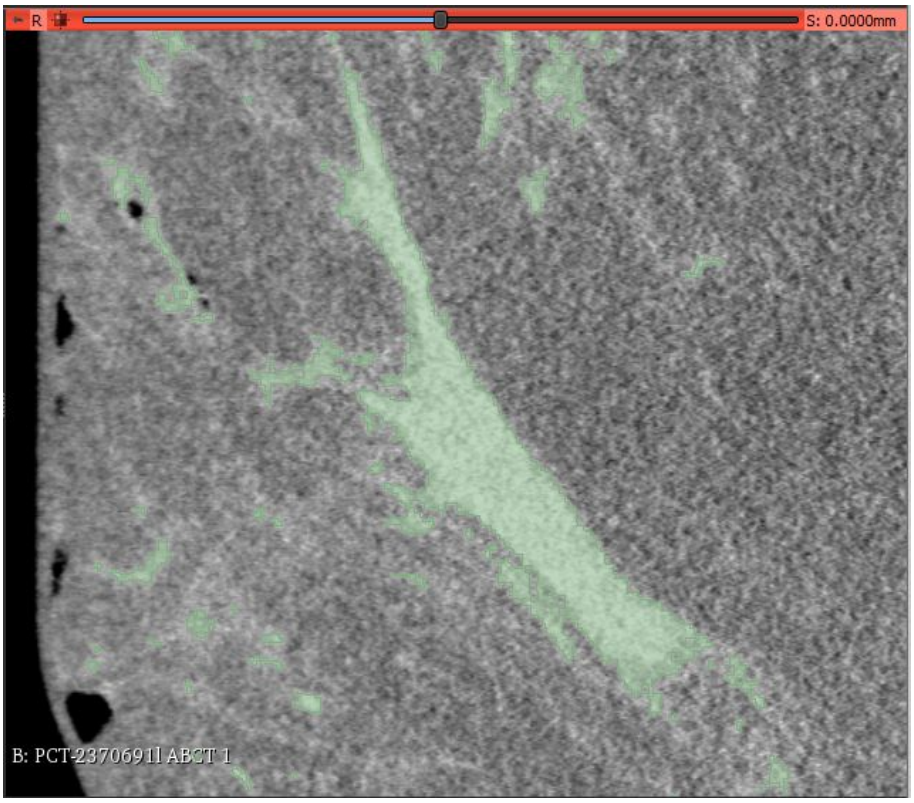


***Figure 2.5:*** *Segmented glandular tissue (in green) on an isolated slice image prior to calculating the "absolute" spatial resolution.*

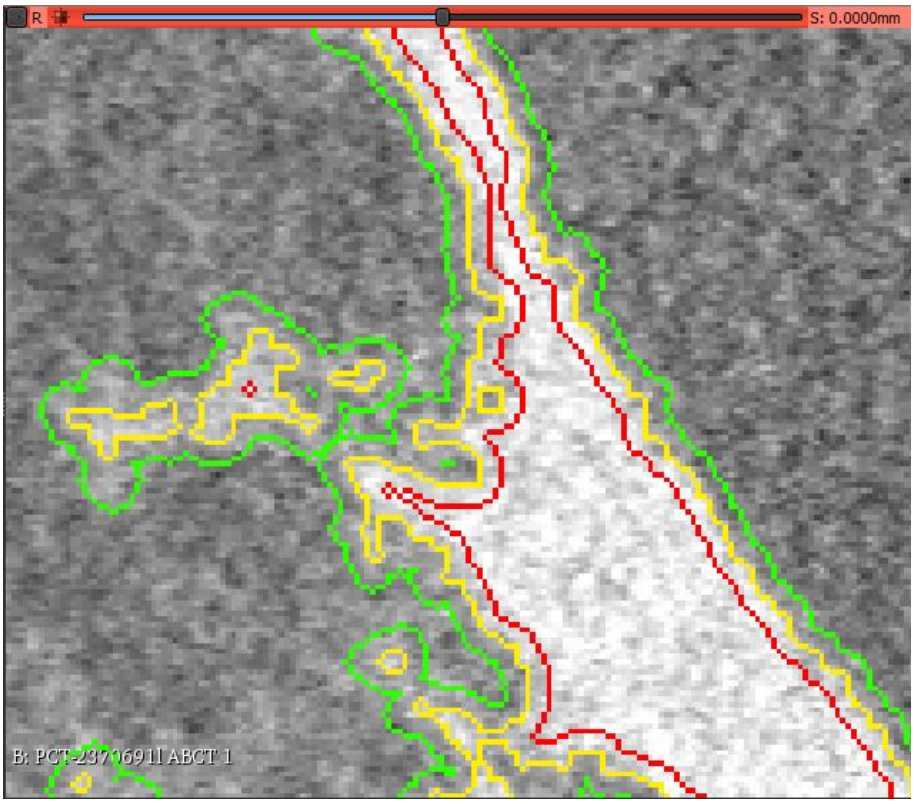


***Figure 2.6:*** *Ring segments resulting from the first (green), fourth (yellow) and eighth (red) iteration of the "absolute" spatial resolution measurement method.*

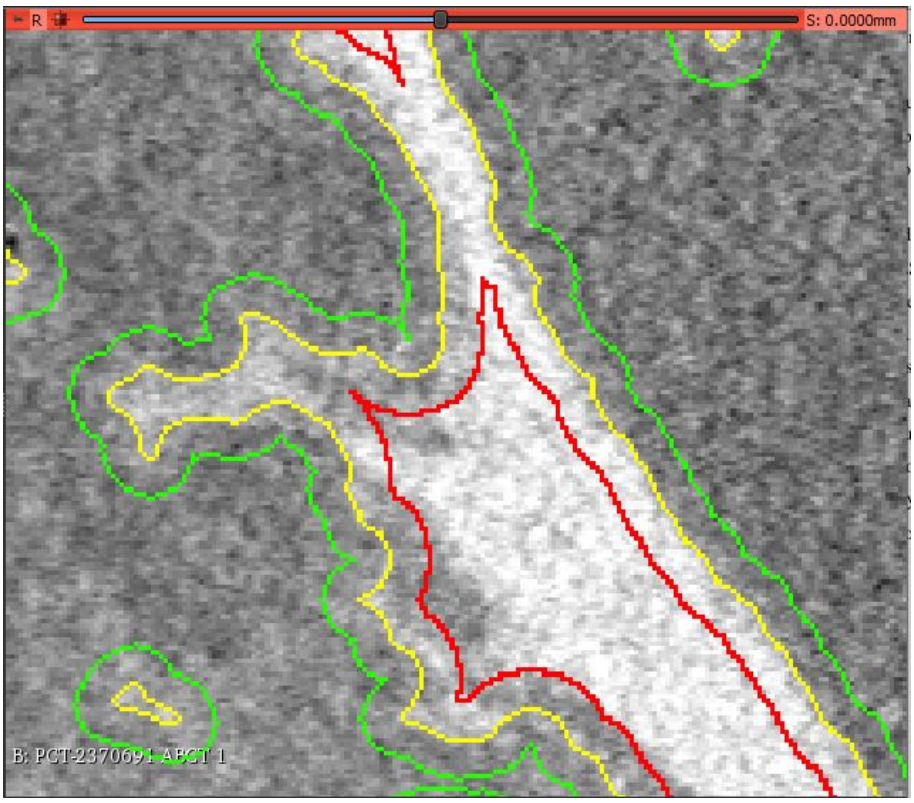


***Figure 2.7:*** *Ring segments resulting from the first (green), eighth (yellow) and sixteenth (red) iteration of the "perceived" spatial resolution measurement method.*

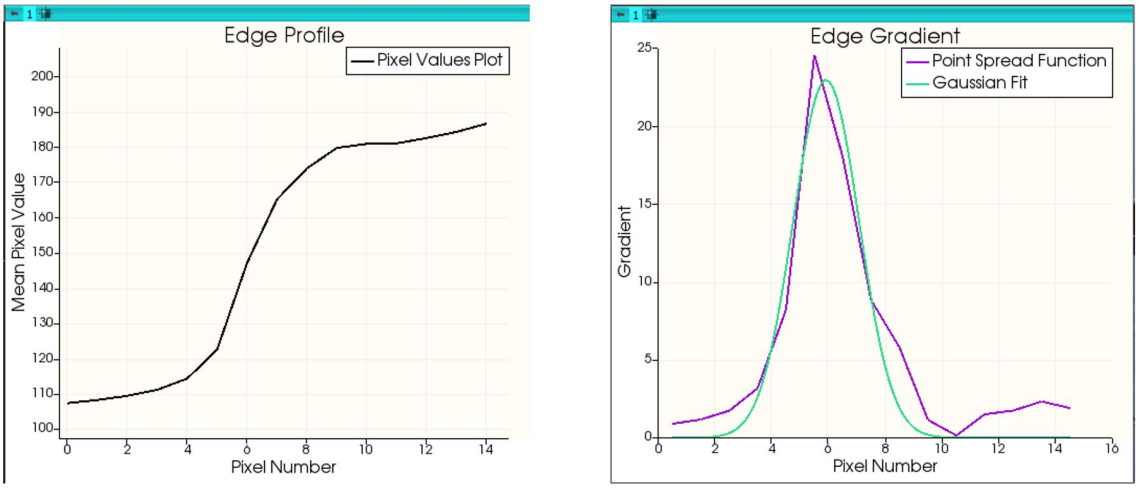


***Figure 2.8:*** *Plots of MPV vs iteration number (left) and the derivative of the edge profile with fitted Gaussian Curve (right).*

### 2.3.3 Formulation of a Predictive Quantitative Image Assessment Metric

Normally the CNR/res criterion gives equal weight to each of its components, namely contrast, noise and spatial resolution. However, it is reasonable to assume that radiologists may, for example, put more weight on sharpness (spatial resolution) of the image rather than contrast or noise. As a result, it may be necessary to weight these components differently, depending on the importance of each component to the overall clinical image quality. The ratios of the contrast, noise and spatial resolution components between the PB-CT and AB-CT image sets were calculated from the data computed using X-TRACT and 3D Slicer software. The contrast ratio is expressed as $C_{PBCT}/C_{ABCT}$, where $C_{PBCT}$ is the contrast calculated for the PB-CT (test) images and $C_{ABCT}$ is the contrast calculated for the AB-CT (reference) images. The SNR ratio is expressed as $SNR_{PBCT}/SNR_{ABCT}$, where $SNR_{PBCT}$ is the SNR calculated for the PB-CT (test) images and $SNR_{ABCT}$ is the SNR calculated for the AB-CT (reference) images. The spatial resolution ratio is expressed as $res_{ABCT}/res_{PBCT}$, where $res_{PBCT}$ is the metric used for expressing the spatial resolution calculated for the PB-CT (test) images and $res_{ABCT}$ is the metric used for expressing the spatial resolution calculated for the AB-CT (reference) images. Note that the spatial resolution ratio is inverted so that in the case where the PB-CT image set has a narrower PSF width (i.e. higher spatial resolution), the resulting spatial resolution ratio is greater than one. A good image, in the context of medical imaging, is generally considered to have high contrast, high SNR, and high spatial resolution (narrow PSF) [12]. Therefore, all the previously introduced quantitative ratios increase as the quantitative metric for the PB-CT (test) scan becomes more desirable relative to the AB-CT (test) scan. The ratio of the CNR/res values is then calculated from the contrast, SNR and spatial resolution ratios using the following formula:

$$(CNR/res_{PBCT})/(CNR/res_{ABCT}) = (C_{PBCT}/C_{ABCT}) \times (SNR_{PBCT}/SNR_{ABCT}) \times (res_{ABCT}/res_{PBCT}). \tag{2.3}$$

Note that in Equation 2.3, the spatial resolution ratio is inverted relative to the contrast and SNR ratios and is therefore multiplied by the contrast and SNR ratios rather than divided by them. The ratio of the CNR/res values between the PB-CT and the AB-CT scans $((CNR/res_{PBCT})/(CNR/res_{ABCT}))$ was calculated in this manner for each of the eight imaging conditions for the 12 patients. The effect of each component on the overall ratio of the CNR/res values can be increased or decreased by scaling each of the contrast, SNR or spatial resolution ratios using the following formula:

$$ScaledRatio = ((Ratio - 1) \times ScalingFactor) + 1, \tag{2.4}$$

so that when a scaling factor greater than one is applied, the ratio diverges away from one (the effect is increased). When a scaling factor of less than one is applied, the ratio

converges towards one (the effect is reduced). When a scaling factor of zero is applied, the ratio is reduced to one (no effect).

To predict the subjective radiologists' score for a particular PB-CT (test) image set relative to a AB-CT (reference) image set, the ratio of the CNR/res value needs to be transformed into a "CNR/res Score" which has values consistent with the subjective radiologist scoring system. The subjective scoring system described in Taba (2021) [97] has a value of +2 when the PB-CT images have significantly higher overall image quality compared to the reference AB-CT images, a value of 0 when both image sets are assessed as being equal and a value of -2 when the PB-CT images have significantly lower overall image quality compared to the reference AB-CT images (shown in Table 2.1).

| Subjective Image Quality of PB-CT scan is: | $\gg$AB-CT reference | = to AB-CT reference | $\ll$AB-CT reference |
|---|---|---|---|
| Score: | +2 | 0 | -2 |

***Table 2.1:*** *Subjective radiologist scoring system described in Taba (2021) [97]*

Consider a situation where three PB-CT image sets are quantitatively assessed against corresponding reference AB-CT image sets by calculating the ratio of the CNR/res values for each of the three PB-CT and AB-CT image sets. The first PB-CT scan has a CNR/res value which is 3 times smaller than the CNR/res value of the corresponding AB-CT reference scan. Therefore, the ratio of the CNR/res values is equal to 0.334. The second PB-CT image set has a CNR/res value which is equal to the CNR/res value of the corresponding AB-CT image set. Therefore, the ratio of the CNR/res values is equal to 1. The third PB-CT image set has a CNR/res value which is 3 times greater than the CNR/res value of the corresponding AB-CT reference image set. Therefore, the ratio of the CNR/res values is equal to 3, as shown in Table 2.2.

| CNR/res value of PB-CT scan is: | $\gg$AB-CT reference | = to AB-CT reference | $\ll$AB-CT reference |
|---|---|---|---|
| Score: | 3 | 1 | 0.334 |

***Table 2.2:*** *Values of the ratio of the CNR/res values under different circumstances*

The values shown in Table 2.2 need to be transformed to a "CNR/res Score" which is consistent with the subjective radiologist scoring system shown in Table 2.1. Two transforms are proposed depending on whether the ratio of the CNR/res values is greater or equal to one, or less than one. When the ratio of the CNR/res values is greater than or equal to one, the value one is subtracted from the ratio to arrive at the "CNR/res Score". Applying this transform to the left-most scores shown in Table 2.2, the value of 3 now becomes 2, and the value of 1 now becomes 0, in line with the corresponding values shown in Table 2.1. If the ratio of the CNR/res values is less than 1, the ratio of the CNR/res values is inverted, has 1 subtracted from it, and is then multiplied by -1. Applying this

transform to the right-most score shown in Table 2.2, the value of 0.334 becomes -2, in line with the left-most score shown in Table 2.1. The maximum and minimum value of the quantitative "scores" is limited to 2 and -2, respectively, in line with the radiologist scoring system. These transforms are implemented using IF statements in Microsoft Excel.

The scaling factors were determined by trial and error to achieve a CNR/res "score" for each imaging condition (averaged across all samples) which closely correlated with the radiologist score for each imaging condition (averaged across all radiologists and samples). The quality of the correlation was assessed by comparing the mean and standard deviation between both the radiologist scores and CNR/res scores and visual assessment of a plot of both parameters.

### 2.3.4 Statistical Analysis

The ability of the quantitative scores to predict the corresponding subjective radiologist scores was assessed using correlation metrics and the mean absolute error between the two sets of scores.

#### Normality Tests

Prior to calculating correlation metrics, the extent to which the data distribution deviates from a Gaussian (normal) distribution must be assessed. Different correlation assessment methods are used, depending on the extent of this deviation. The Graphpad Prism [119] software help page [120] recommends the use of a D'Agostino-Pearson omnibus K2 test [121]. This test was used in Graphpad Prism [119] to perform a normality test on all data sets prior to performing a correlation analysis. The D'Agostino-Pearson omnibus normality test computes the skewness and kurtosis to quantify the deviation of the distribution from a Gaussian distribution in terms of asymmetry and shape. It then calculates the deviation of these values from the expected Gaussian distribution values. Finally, a single P-value from the sum of these deviations is calculated [120]. A significance level (alpha) of 0.05 was used to assess whether or not the data passed the normality test. If the P-value is greater than 0.05, the data passes the normality test and is assumed to be Gaussian (normal). If the P-value is less than 0.05, the data fails the normality test and cannot be assumed to be Gaussian (normal) [122].

#### Correlation Analysis

Graphpad Prism [119] was used to assess the correlation between the radiologists' scores and various quantitative metrics. An XY correlation analysis was performed using the Prism software. If the data passed the previously explained normality test, the data was assumed to be Gaussian, and a Pearson correlation coefficient (r) was computed. If the data did not pass the normality test, the data was not assumed to be Gaussian, and a nonparametric Spearman correlation coefficient (rs) was computed. The correlation

coefficient (r) ranges from -1 to 1. The Spearman correlation coefficient (rs) has the same range. An r-value of 1 indicates a perfect correlation, an r-value of 0 indicates no correlation, and an r-value of -1 indicates a perfect inverse correlation [123]. A two-tailed P-value was computed with a confidence interval of 95%. The P-value indicates the chance that random sampling would result in a correlation coefficient as far from zero (or further) as observed in the experiment. If the P-value is small, the correlation is very unlikely due to random sampling. If the P-value is large, then there is no compelling evidence that the correlation is real and not due to chance [123]. By default, Prism considers the correlation significant if the P-value is less than 0.05.

**Mean Absolute Error**

The previously described correlation assessment does not indicate how well the quantitative scores predict the absolute value of the radiologists' scores. The mean absolute error (MAE) indicates, on average, the deviation between the quantitative and radiologists' scores. If the value of the MAE is 0, the quantitative scores perfectly predict the values of the radiologists' scores. The further the MAE deviates from 0, the poorer the quantitative scores are at predicting the value of the radiologists' scores. The MAE is calculated using the following equation:

$$MAE = \frac{1}{n}\sum_{i=1}^{n}(|q_i - s_i|), \tag{2.5}$$

where, $q_i$, are the quantitative score data set values, $s_i$, are the corresponding radiologists' score data set values and $n$ is the number of corresponding quantitative and radiologists' score pairs.

# Chapter 3

# Results

This section begins by describing the subjective radiologists' assessment data which was acquired by Taba et al. [97]. The data acquired by implementing the methods described in the previous chapter using X-TRACT and 3D Slicer software is then presented. This section contains material presented in a submitted paper (see Section B).

## 3.1 Subjective Radiologist Assessment

Each radiologist provided a score between 2 and -2 (as described in Section 2.2) for each PB-CT image relative to the corresponding AB-CT reference image and for each imaging condition for each sample. Table 3.1 shows an example of the 11 radiologist (labelled A1-A11) scores for each of the eight PB-CT imaging conditions for sample number 2370691. Due to the coarse scoring system and the scoring variation between individual radiologists, the standard deviation associated with each imaging condition is relatively large.

| Individual Radiologist Scores - 2370691 | | | | | | | | | | | | | |
|---|---|---|---|---|---|---|---|---|---|---|---|---|---|
| Radiologist Number: | A1 | A2 | A3 | A4 | A5 | A6 | A7 | A8 | A9 | A10 | A11 | AV | SD |
| 32keV-2mGy-fTIE | 1 | 2 | 1 | 2 | 1 | 1 | 1 | 1 | 2 | 1 | 1 | 1.27 | 0.45 |
| 32keV-2mGy-hTIE | 2 | 2 | 2 | 2 | 2 | 1 | 2 | 2 | 2 | 2 | 1 | 1.82 | 0.39 |
| 32keV-4mGy-fTIE | 1 | 2 | 1 | 2 | 1 | 1 | 1 | 1 | 1 | 1 | 0 | 1.09 | 0.51 |
| 32keV-4mGy-hTIE | 2 | 2 | 2 | 2 | 2 | 1 | 2 | 1 | 1 | 1 | 1 | 1.55 | 0.50 |
| 34keV-2mGy-fTIE | 1 | 1 | 1 | 2 | 1 | -1 | 2 | 1 | 1 | 1 | 0 | 0.91 | 0.79 |
| 34keV-2mGy-hTIE | 1 | 1 | 1 | 2 | 1 | 1 | 1 | 0 | 2 | 1 | 1 | 1.09 | 0.51 |
| 34keV-4mGy-fTIE | 0 | 1 | 0 | 2 | 1 | 0 | 1 | 1 | 0 | 0 | 0 | 0.55 | 0.66 |
| 34keV-4mGy-hTIE | 1 | 1 | 0 | 2 | 1 | 0 | 1 | 0 | 0 | 1 | 0 | 0.64 | 0.64 |

***Table 3.1:*** *Individual radiologist (labelled A1-A11) scores for sample number 2370691. Average (AV) and standard deviation (SD) are shown in the right most columns.*

Tables 3.2 & 3.3 show the average radiologist scores (averaged across 11 radiologists) for each of the eight imaging conditions for each of the 12 samples. Tables A.1 and A.2 of the appendix show the standard deviations associated with each average radiologist score presented in Tables 3.2 and 3.3.

Table 3.4 shows the average radiologist score and standard deviation for each imaging condition, averaged across all 12 samples.

| Average Radiologist Scores | | | | | | |
|---|---|---|---|---|---|---|
| Sample Number: | 2370691 | 4247239 | 4638975 | 4704628 | 7096050L | 709605R |
| 32keV-2mGy-fTIE | 1.27 | 1.45 | 1.09 | 0.55 | 0.55 | 1.36 |
| 32keV-2mGy-hTIE | 1.82 | 1.45 | 1.36 | 0.91 | 0.55 | 1.18 |
| 32keV-4mGy-fTIE | 1.09 | 1.36 | 1.18 | 0.55 | 0.55 | 1.18 |
| 32keV-4mGy-hTIE | 1.55 | 1.36 | 1.18 | 0.64 | 0.64 | 1.45 |
| 34keV-2mGy-fTIE | 0.91 | 1.00 | 0.55 | 0.00 | 0.09 | 0.91 |
| 34keV-2mGy-hTIE | 1.09 | 0.73 | 0.73 | 0.27 | 0.09 | 1.36 |
| 34keV-4mGy-fTIE | 0.55 | 0.82 | 0.45 | -0.27 | 0.18 | 0.64 |
| 34keV-4mGy-hTIE | 0.64 | 1.00 | 0.73 | 0.45 | 0.45 | 0.91 |

***Table 3.2:*** *Average radiologist scores for each imaging condition for the first six samples*

| Average Radiologist Scores | | | | | | |
|---|---|---|---|---|---|---|
| Sample Number: | 7104092 | 7949430 | 8283541L | 8283541R | 8413420 | 8423990 |
| 32keV-2mGy-fTIE | 1.36 | 0.73 | 0.64 | 1.27 | 1.18 | 0.00 |
| 32keV-2mGy-hTIE | 1.27 | 1.18 | 1.00 | 1.45 | 1.00 | 0.27 |
| 32keV-4mGy-fTIE | 0.91 | 0.91 | 0.64 | 1.64 | 1.18 | 0.09 |
| 32keV-4mGy-hTIE | 1.18 | 1.18 | 0.64 | 1.64 | 1.27 | 0.64 |
| 34keV-2mGy-fTIE | 0.73 | -0.18 | 0.18 | 0.91 | 0.55 | -0.27 |
| 34keV-2mGy-hTIE | 1.09 | 0.55 | 0.27 | 1.27 | 0.36 | 0.00 |
| 34keV-4mGy-fTIE | 0.64 | -0.09 | 0.18 | 1.00 | 0.55 | -0.36 |
| 34keV-4mGy-hTIE | 0.64 | 0.45 | 0.18 | 1.27 | 0.64 | -0.45 |

***Table 3.3:*** *Average radiologist scores for each imaging condition for the last six samples*

| Average of the Average Radiologist Scores | | |
|---|---|---|
| | Average | SD |
| 32KeV-2mGy-fTIE | 0.95 | 0.43 |
| 32KeV-2mGy-hTIE | 1.12 | 0.40 |
| 32KeV-4mGy-fTIE | 0.94 | 0.41 |
| 32KeV-4mGy-hTIE | 1.11 | 0.36 |
| 34KeV-2mGy-fTIE | 0.45 | 0.44 |
| 34KeV-2mGy-hTIE | 0.65 | 0.45 |
| 34KeV-4mGy-fTIE | 0.36 | 0.41 |
| 34KeV-4mGy-hTIE | 0.58 | 0.42 |

***Table 3.4:*** *Average radiologist scores and standard deviation for each imaging condition, averaged across all 12 samples*

## 3.2 X-TRACT Results

The un-scaled contrast, SNR, spatial resolution and CNR/res ratios between the PB-CT (test) and AB-CT (reference) images for each imaging condition (averaged across all axial and sagittal image sets of all samples) were converted to quantitative "scores" (as described in Section 2.3.3). These un-scaled quantitative "scores" are tabulated in Table A.3 and plotted against the average radiologist score for each imaging condition (averaged across all radiologists and samples) in Figure 3.1.

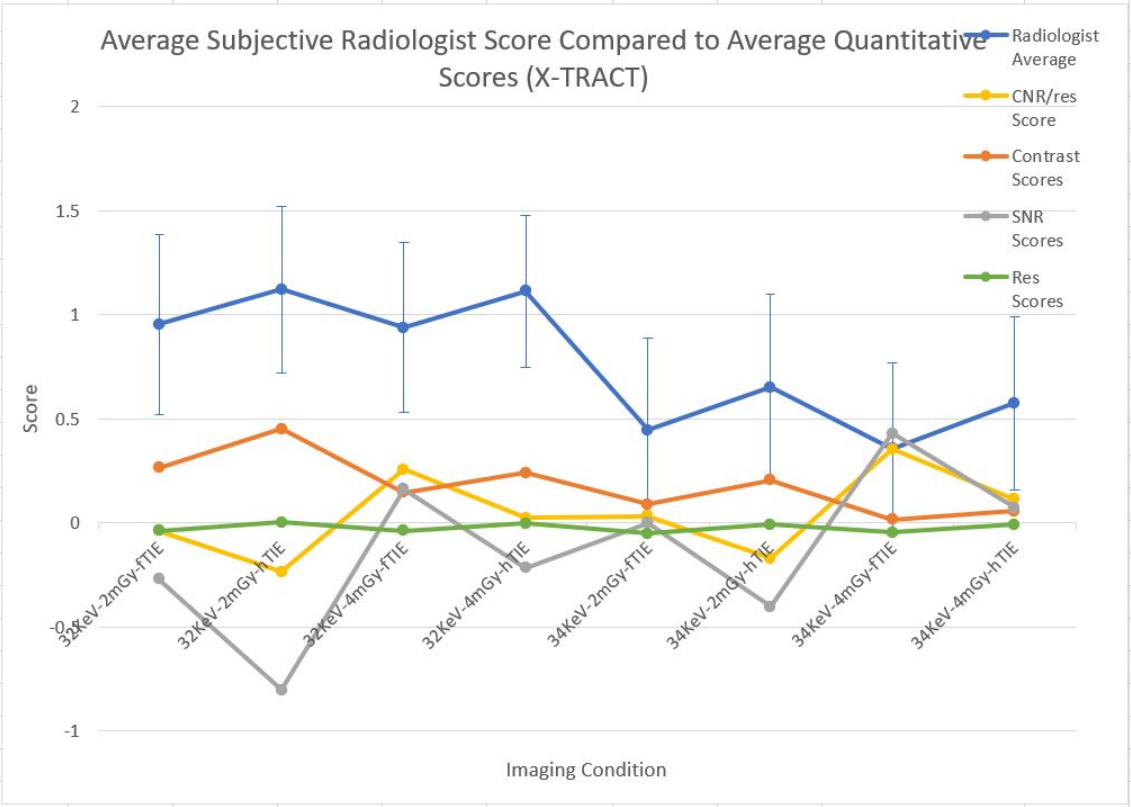


***Figure 3.1:*** *Plot of radiologist scores (in blue) for each imaging condition averaged across all radiologists and samples (scores shown in Table 3.4), with error bars of ± one standard deviation (also shown in Table 3.4). The radiologist score is compared to various un-scaled quantitative scores measured using X-TRACT including; CNR/res (yellow), contrast (red), SNR (grey) and spatial resolution (green). These results are tabulated in Table A.3*

The correlation between the radiologist scores and the four un-scaled quantitative "scores" (shown in Figure 3.1) was then analysed using the Graphpad Prism Software [119]. The resulting correlation metrics are displayed in Table 3.5.

The contrast, SNR and spatial resolution ratios were then scaled using Equation 2.4 before being converted into a "score" as described in Section 2.3.3. The CNR/res "score" comprises the scaled contrast, SNR and spatial resolution components as shown in Equation 2.3. The final scaling factors which were used in Equation 2.4 to scale the ratio of each quantitative measure were; 3.7 for the contrast ratio, 0.9 for the SNR ratio and 6 for

| Correlation Between Radiologist and Un-scaled Quantitative Scores | | | | |
|---|---|---|---|---|
| | Radiologist vs contrast | Radiologist vs SNR | Radiologist vs Res | Radiologist vs CNR/res |
| Pearson r | 0.8346 | -0.6561 | 0.5574 | -0.4660 |
| P value (two tailed) | 0.0100 | 0.0773 | 0.1512 | 0.2445 |
| Significant? | Yes | No | No | No |

***Table 3.5:*** *Correlation metrics between the radiologist scores and each of the four un-scaled quantitative metrics plotted in Figure 3.1 calculated using Graphpad Prism [119]. The correlation is considered significant if the P-value is less than 0.05.*

the spatial resolution ratio. The scaled quantitative scores are shown in Figure 3.2 and tabulated in Table A.4. The CNR/res scores shown in yellow in Figure 3.2 show a good correlation with the radiologist scores shown in blue. However, there is a clear height discrepancy between the two plots. With the addition of an offset factor of 0.55 to the CNR/res scores, the mean (or height in the case of a plot) closely matches the mean of the subjective radiologist scores as shown in Figure 3.3.

As with the un-scaled results, the correlation between the radiologist scores and the scaled quantitative metrics (shown in Figure 3.3) was analysed using the Graphpad Prism software [119]. The resulting correlation metrics are displayed in Table 3.6. The correlation metrics between the radiologist scores and the scaled contrast, SNR and spatial resolution scores remain similar to the un-scaled scores shown in Table 3.5 despite scaling. The correlation between the subjective radiologist scores and the scaled CNR/res score, comprising the scaled contrast, SNR and spatial resolution ratios, is significantly improved.

| Correlation Between Radiologist and Scaled Quantitative Scores | | | | |
|---|---|---|---|---|
| | Radiologist vs Contrast | Radiologist vs SNR | Radiologist vs Res | Radiologist vs CNR/res |
| Pearson r | 0.8532 | -0.6562 | 0.5220 | 0.9610 |
| P value (two tailed) | 0.0071 | 0.0772 | 0.1845 | 0.0001 |
| Significant? | Yes | No | No | Yes |

***Table 3.6:*** *Correlation metrics between the radiologist scores and each of the four scaled quantitative metrics plotted in Figure 3.3 calculated using Graphpad Prism [119]. The correlation is considered significant if the P-value is less than 0.05.*

Figure 3.3 and Table 3.6 demonstrate that a correlation has been established between the average radiologist scores and the average, scaled CNR/res scores. This suggests that it is possible to predict the PB-CT imaging conditions which radiologists generally prefer for a group of patients using the scaled CNR/res score. However, it is also important to predict which imaging conditions are preferred by radiologists for individual patients. Therefore, the ability of the scaled CNR/res score to predict radiologist scores for each sample also needs to be assessed. Figures A.1 - A.12 show the radiologist scores plot-

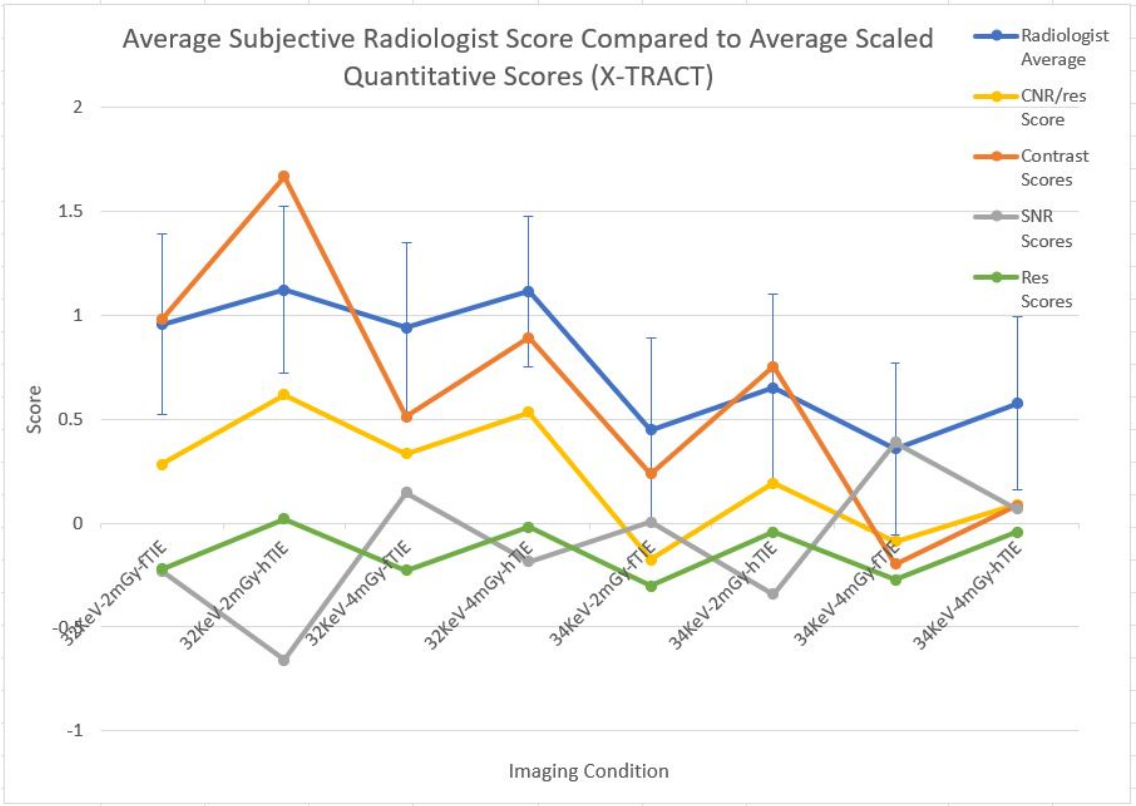


***Figure 3.2:*** *Plot of subjective radiologist scores (in blue) for each imaging condition averaged across all radiologists and samples (scores shown in Table 3.4), with error bars of ± one standard deviation (also shown in Table 3.4). The subjective radiologist score is compared to various scaled quantitative scores measured using X-TRACT including; CNR/res (yellow), contrast (red), SNR (grey) and spatial resolution (green).*

ted alongside the scaled contrast, SNR, spatial resolution and scaled and offset CNR/res scores for each of the 12 samples. The same previously mentioned scaling factors are used to arrive at the scaled CNR/res scores shown in Figures A.1 - A.12. The scaled CNR/res criterion is able to predict 89 of the 96 radiologist scores to within one standard deviation (93%) as shown in Tables A.6 and A.7. In these tables, the cells highlighted in green are within one standard deviation of the corresponding subjective radiologist score, and the cells highlighted in yellow are outside one standard deviation. An XY correlation analysis between all 96 scaled CNR/res scores and the corresponding subjective radiologist scores was performed using the GraphPad Prism software (see Section 2.3.4). Prior to the correlation analysis, a D'Agostino-Pearson normality test was performed on the data, which confirmed that the data, in this case, did not have a normal (Gaussian) distribution. As a result, the data cannot be assumed to be Gaussian, and the "compute nonparametric Spearman correlation" option was selected when performing the correlation analysis. The correlation metrics are shown in Table 3.7. The MAE (Equation 2.5) between the CNR/res scores and corresponding radiologist scores across all individual samples was 0.29.

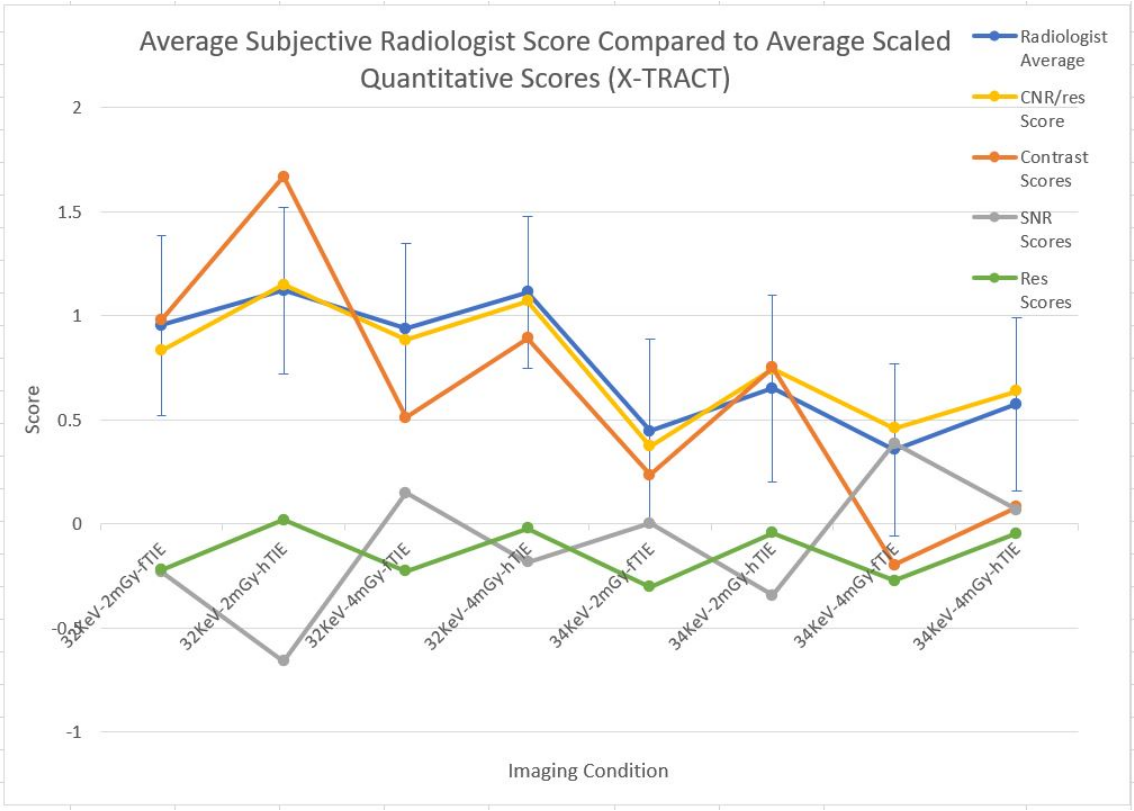


***Figure 3.3:*** *Plot of subjective radiologist scores (in blue) for each imaging condition averaged across all radiologists and samples (scores shown in Table 3.4), with error bars of ± one standard deviation (also shown in Table 3.4). The subjective radiologist score is compared to various scaled and offset quantitative scores measured using X-TRACT including; CNR/res (yellow), contrast or contrast (red), SNR (grey) and spatial resolution (green). The CNR/res scores have had an offset factor of 0.55 added to all values so that the height of the plot closely matches the radiologist scores.*

| Correlation Between Radiologist Scores and Scaled CNR/res Scores Across Individual Samples (X-TRACT) | |
|---|---|
| | Radiologist vs CNR/res |
| Spearman (rs) | 0.7898 |
| P value (two tailed) | <0.0001 |
| Significant? | Yes |

***Table 3.7:*** *Overall correlation metrics between the 96 scaled CNR/res scores plotted in Figures A.1 - A.12 and the corresponding radiologist scores calculated using Graphpad Prism [119]. The correlation is considered significant if the P-value is less than 0.05.*

## 3.3 3D Slicer Results

As with the X-TRACT results, the quantitative ratios measured using 3D Slicer for each imaging condition (averaged across all axial and sagittal image sets of all samples) were converted into quantitative "scores" (as described in Section 2.3.3). The un-scaled quantitative scores were tabulated in Table A.8 and plotted against the average radiologist score for each imaging condition (averaged across all radiologists and samples) in Figure 3.4. Note that the CNR/res score shown in yellow in Figure 3.4 was calculated using the "perceived" spatial resolution ratio in Equation 2.3.

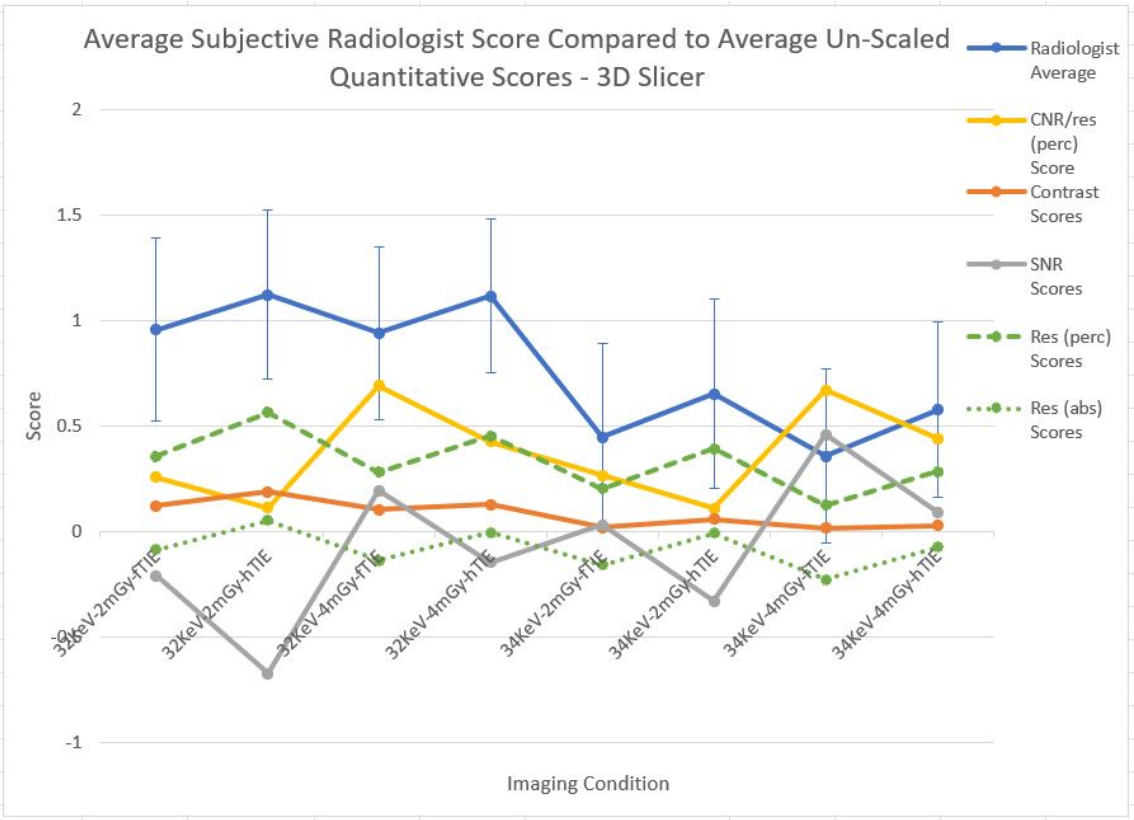


***Figure 3.4:*** *Plot of radiologist scores (in blue) for each imaging condition averaged across all radiologists and samples (scores shown in Table 3.4), with error bars of ± one standard deviation (also shown in Table 3.4). The radiologist score is compared to various un-scaled quantitative scores measured using 3D Slicer including; CNR/res (perc) (yellow), contrast (red), SNR (grey), "absolute" spatial resolution (green dotted) and "perceived" spatial resolution (green dashed). These results are tabulated in Table A.8. The CNR/res (perc) score shown in yellow was calculated using the "perceived" spatial resolution ratio in Equation 2.3.*

The correlation between the subjective radiologist scores and the five un-scaled quantitative "scores" (shown in Figure 3.4) was then analysed using the Graphpad Prism software [119]. The resulting correlation metrics are displayed in Table 3.8.

The contrast, SNR and spatial resolution ratios were then scaled using Equation 2.4 before being converted into a "score" as described in Section 2.3.3. The CNR/res "score"

| Correlation Between Subjective and Un-scaled Quantitative Scores (3D Slicer) | | | | | |
|---|---|---|---|---|---|
| | Radiologist vs Contrast | Radiologist vs SNR | Radiologist vs Res (perc) | Radiologist vs Res (abs) | Radiologist vs CNR/res (perc) |
| Pearson r | 0.9484 | -0.6474 | 0.8360 | 0.7075 | -0.2240 |
| P value | 0.0003 | 0.0826 | 0.0097 | 0.0497 | 0.5938 |
| Significant? | Yes | No | Yes | Yes | No |

***Table 3.8:*** *Correlation metrics between the radiologist scores and each of the five un-scaled quantitative metrics plotted in Figure 3.4 calculated using Graphpad Prism [119]. The correlation is considered significant if the P-value is less than 0.05.*

comprises the scaled contrast, SNR and spatial resolution components as shown in Equation 2.3. The final scaling factors which were used in Equation 2.4 to scale the ratio of each quantitative measure were; 1.2 for the contrast ratio, 0.35 for the SNR ratio and 2 for the "perceived" spatial resolution ratio. The scaled quantitative scores are shown in Figure 3.5 and tabulated in Table A.9.

The correlation between the radiologist scores and the five scaled quantitative metrics (shown in Figure 3.5) was analysed using the Graphpad Prism software [119]. The resulting correlation metrics are displayed in Table 3.9. The correlation metrics between the radiologist scores and the scaled contrast, SNR and spatial resolution scores are similar to the un-scaled scores shown in Table 3.8, despite scaling. The correlation between the radiologist scores and the CNR/res (perc) scores, which comprise the scaled contrast, SNR and "perceived" spatial resolution ratios, is significantly improved.

| Correlation Between Subjective and Scaled Quantitative Scores (3D Slicer) | | | | |
|---|---|---|---|---|
| | Radiologist vs Contrast | Radiologist vs SNR | Radiologist vs Res | Radiologist vs CNR/res |
| Pearson r | 0.9431 | -0.6494 | 0.8413 | 0.9551 |
| P value (two tailed) | 0.0004 | 0.0814 | 0.0088 | 0.0002 |
| Significant? | Yes | No | Yes | Yes |

***Table 3.9:*** *Correlation metrics between the subjective radiologist scores and each of the four scaled quantitative metrics, which are plotted in Figure 3.5, calculated using Graphpad Prism. The correlation is considered significant if the P value is less than 0.05.*

As discussed in Section 3.2 the ability of the scaled CNR/res score to predict the subjective radiologist scores for individual samples is also assessed. Figures A.13 - A.24 show the average radiologist scores (averaged over 11 radiologists) plotted alongside the scaled contrast, SNR, "perceived" spatial resolution and CNR/res (perc) scores for each of the 12 samples. The same previously mentioned scaling factors are used to arrive at the scaled CNR/res (perc) scores shown in Figures A.13 - A.24. The scaled CNR/res (perc) criterion is able to predict 94 of the 96 subjective radiologist scores to within one standard

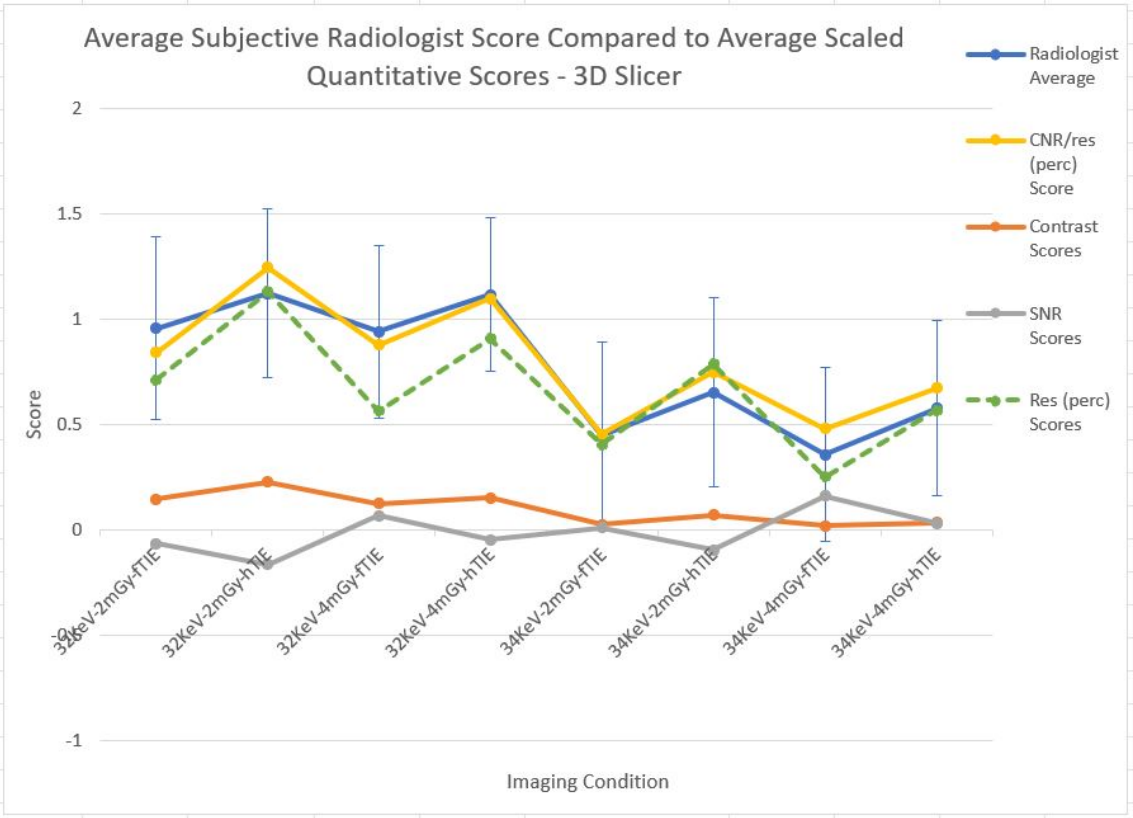


***Figure 3.5:*** *Plot of subjective radiologist scores (in blue) for each imaging condition averaged across all radiologists and samples (scores shown in Table 3.4), with error bars of ± one standard deviation (also shown in Table 3.4). The subjective radiologist score is compared to various scaled quantitative scores measured using 3D Slicer including; CNR/res (yellow), contrast (red), SNR (grey) and spatial resolution (green).*

deviation (98%) as shown in Tables A.10 and A.11. In these tables, the cells highlighted in green are within one standard deviation of the corresponding radiologist score, and the cells highlighted in yellow are outside one standard deviation. An XY correlation analysis between all 96 scaled CNR/res scores and the corresponding subjective radiologist scores was performed using the Graphpad Prism software [119]. The correlation metrics are shown in Table 3.10. The MAE (Equation 2.5) between the 96 individual weighted CNR/res scores and the corresponding radiologist scores across all individual samples was 0.20.

| Correlation Between Radiologist Scores and Scaled CNR/res Scores | |
|---|---|
| | Radiologist vs CNR/res (perc) |
| Spearman r | 0.8872 |
| P value (two tailed) | <0.0001 |
| Significant? | Yes |

***Table 3.10:*** *Overall correlation metrics between the 96 CNR/res scores plotted in Figures A.13 - A.24 and the corresponding radiologist scores calculated using Graphpad Prism. The correlation is considered significant if the P-value is less than 0.05.*

## 3.4 8-bit Image Pixel Value Analysis

The measurements in the previous sections were performed on the same 8-bit greyscale images, which were scored by the radiologists in the study by Taba et al. [97]. When analysing the images, it was noted that the MPVs within both the glandular and adipose regions of the 8-bit images differed considerably between images of the same mastectomy sample when using different imaging conditions. Conventional CT produces an image where the pixel values are expressed as HU. HU represent the linear attenuation coefficient of the imaged material relative to water (Equation 1.37). Therefore, the MPVs within the glandular and adipose regions are expected to stay relatively constant across all images acquired using the same X-ray energy. An example of considerable variation in MPVs is shown in Figure 3.6 which compares a 32keV-2mGy-hTIE 8-bit image with a 32keV-4mGy-hTIE 8-bit image of the same mastectomy sample. The only imaging parameter which differs between the two images is the radiation dose, so considerable variation in MPV is unexpected. The original coronal, 0.1mm slice thickness images of the mastectomy samples used a 32-bit greyscale. The pixel values in these original images represent the imaginary component of the complex refractive index ($\beta$ of Equation 1.14) of the material being imaged. These images were then used to create sagittal and axial reconstructions with a 1mm slice thickness as described in Section 2.2. The 32-bit greyscale was then converted into an 8-bit greyscale. The MPVs in the glandular and adipose regions of the original images used to create the retro-reconstructed images shown in Figure 3.6 were measured. Figure 3.7 shows that the MPVs remain relatively constant between the original 32keV-2mGy-hTIE and 32keV-4mGy-hTIE images. Furthermore, the MPVs are a good approximation of the expected $\beta$ values of 1.07 x $10^{-10}$ and 8.08 x $10^{-11}$ for glandular and adipose tissue, respectively at 32 keV [60]. It appears that the pixel values have not been scaled consistently when converting from 32-bit to 8-bit greyscale. It is postulated by the author that an automatic histogram-based scaling algorithm has been utilised, which scales the entire range of pixel values in the 32-bit image into an 8-bit greyscale. The 32-bit 2 mGy image shown on the left in Figure 3.7 has a pixel value range of -9.48 x $10^{-11}$ to 2.02 x $10^{-10}$, while the 4 mGy image shown on the right of Figure 3.7 has a range of -9.99 x $10^{-11}$ to 1.62 x $10^{-10}$. The larger pixel value range in the 2 mGy image is due to a higher presence of noise in the image. This difference in range has likely resulted

in an automatic, histogram-based conversion program generating inconsistent pixel values seen in the 8-bit images. The higher top end of the pixel value range in the 32-bit 2 mGy image have resulted in the MPVs of glandular and adipose tissue being lower in the 8-bit range compared to the 4 mGy image. As a result, the 2 mGy image appears darker than the 4 mGy image, as is evident in Figure 3.6. Contrast is defined as the ratio of the signal difference to the average signal (Equation 1.38). A small MPV difference becomes negligible if the average signal is large, while the same small difference is readily visible if the average signal is small [12]. Therefore, the inconsistencies in average pixel value in the 8-bit greyscale images add a false difference in contrast. This difference in contrast is due to the images being viewed at different windows and levels, rather than intrinsic physical processes between the different imaging conditions. Due to inconsistent image display, this false contrast has likely made it difficult for radiologists to effectively assess the differences in image quality due to physical differences in imaging conditions. Likewise, the perception of noise may change with differing grey levels between the 8-bit images.

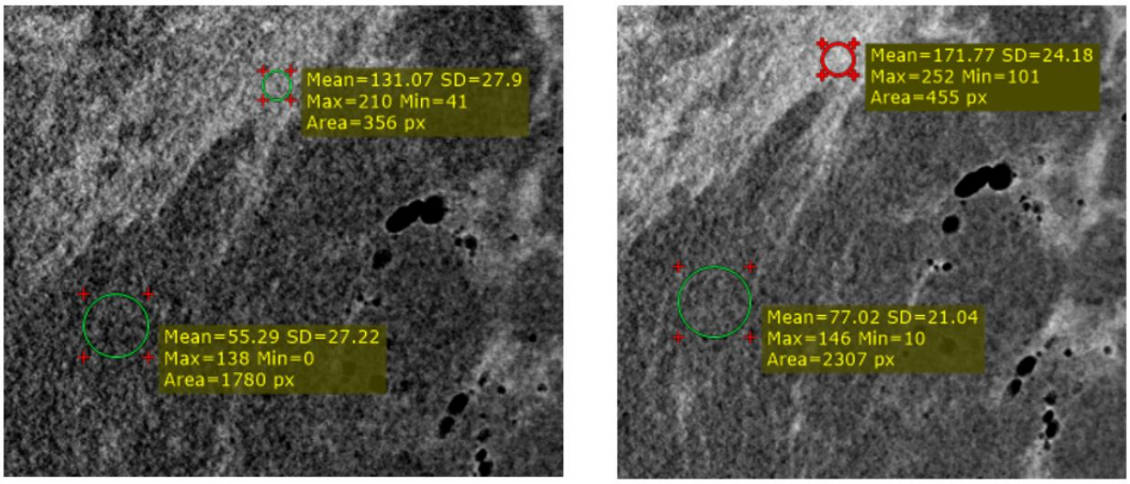


***Figure 3.6:*** *Comparison of the MPVs within glandular and adipose regions between a 32keV-2mGy-hTIE 8-bit image (left) and a 32keV-4mGy-hTIE 8-bit image (right) of sample 4247239. Considerable variations between MPVs were found between the images.*

It is proposed that the 32-bit greyscale images be converted to 8-bit greyscale images using a consistent window which depends on the X-ray energy used to acquire the scan. The two fixed windows for the 32 keV and 34 keV images should be chosen to preserve consistent MPVs between images of the same X-ray energy. Using a lower X-ray energy will result in higher contrast between glandular and adipose tissue. The conversion windows are chosen so that the average signal (average between the MPV in the gladular and adipose regions) is the same between the resultant 8-bit, 32 keV and 34 keV images. This allows the signal difference between glandular and adipose areas to be more easily compared visually in the 8-bit images which use different X-ray energies. The conversion windows are additionally chosen such that the ratio of the glandular/adipose contrast between the original 32-bit 32 keV image and 32-bit 34 keV images is maintained throughout

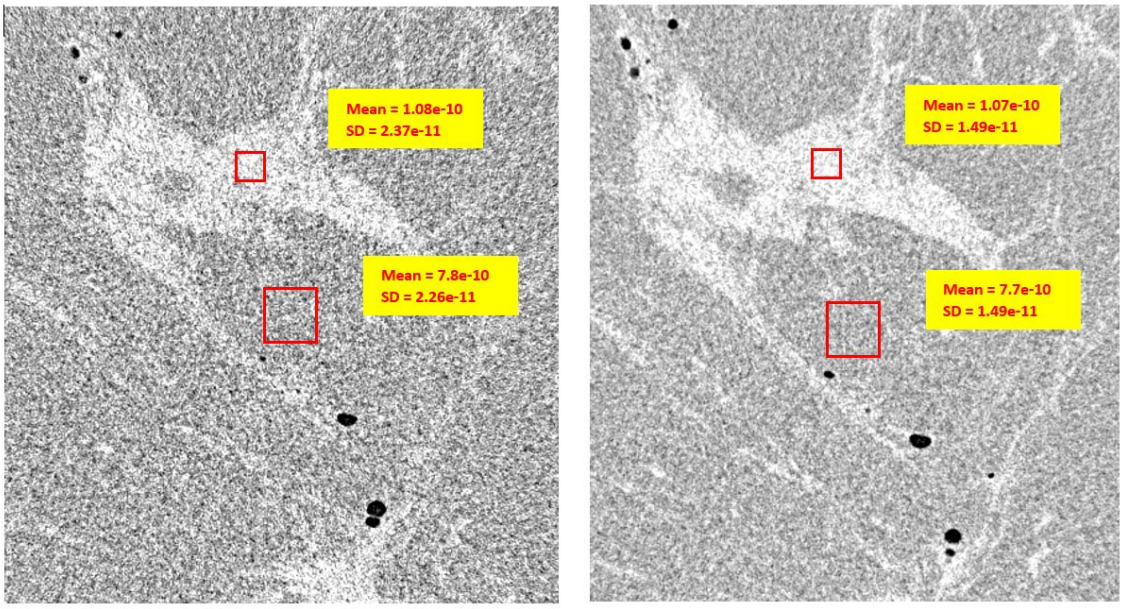


***Figure 3.7:*** *Comparison of the MPVs within glandular and adipose regions between a 32keV-2mGy-hTIE 32-bit image (left) and a 32keV-4mGy-hTIE 32-bit image (right) of sample 4247239. No considerable differences between MPVs were found between the images.*

the conversion. This preserves the contrast difference inherent to the imaging X-ray energy used. When viewed at consistent windows and levels, any contrast differences between the images are due only to the physical differences between imaging parameters. Figure 3.8 shows proposed 32-bit greyscale windows, calculated using Microsoft Excel, for both the 32 keV and 34 keV scans which are scaled into an 8-bit greyscale window of 0-255. The choice of window ensures that the average of the MPVs between the adipose and glandular tissues is kept constant (approx 146.4) between the resultant 8-bit images of different X-ray energy. The glandular contrast ratio between the 32 keV and 34 keV images (32 keV/34 keV) is maintained at 1.072 throughout the conversion.

The 32keV, 32-bit images were converted into 8-bit greyscale using the proposed conversion window shown in Figure 3.7 using the following Matlab code:

| 32keV | Original 32 bit Image | Resulting 8 Bit Image |
|---|---|---|
| Adipose MPV | 7.72E-11 | 105.46 |
| Glandular MPV | 1.06E-10 | 187.40 |
| Average MPV | 9.17E-11 | 146.43 |
| Visibility | 0.158 | 0.280 |
| | | |
| | Window Bounds | |
| Lower | 4.000E-11 | 0 |
| Upper | 1.300E-10 | 255 |
| | | |
| 34keV | Original 32 bit Image | Resulting 8 Bit Image |
| Adipose MPV | 6.95E-11 | 108.22 |
| Glandular MPV | 9.35E-11 | 184.62 |
| Average MPV | 8.15E-11 | 146.42 |
| Visibility | 0.147 | 0.261 |
| | | |
| | Window Bounds | |
| Lower | 3.555E-11 | 0 |
| Upper | 1.156E-10 | 255 |
| | | |
| | 32keV/34keV Visibility Ratios | |
| | 1.072 | 1.072 |

***Figure 3.8:*** *Microsoft Excel spreadsheet showing X-ray energy dependent 32-bit windows which are used to convert greyscale images from 32-bit to 8-bit greyscale. The windows are chosen so that the average of the MPVs in the glandular and adipose regions is maintained between the resultant 8-bit 32 keV and 34 keV images (at a pixel value of 146.4). The conversion windows are additionally chosen such that the ratio of the glandular/adipose contrast (or visibility) between the original 32-bit 32 keV image and 32-bit 34keV images (of 1.072) is maintained throughout the conversion. This is intended to ensure that any contrast differences between the 8-bit 32 keV and 34 keV images are due to physical differences between X-ray energies rather than inconsistent image display.*

```
function [Output] = ConvertEightBit(fullFileName)

Input = imread(fullFileName);

% Specify bounds of window
LowerBound = 4E-11; %4E-11 for 32 keV, 3.555E-11 for 34 keV
UpperBound = 1.3E-10; %1.3E-10 for 32 keV, 1.156E-10 for 34 keV

% Convert specified window to 0-255
Input = ((Input-LowerBound)/(UpperBound-LowerBound))*255;
% Convert to 8 bit integer values
Output = uint8(Input);
```

Which was called in the matlab window using the following entry:

```
>> dicomwrite(ConvertEightBit('32keV_2mGy_hTIE_0107.tif'),
'32keV_2mGy_hTIE_0107.dcm'),
```

where, 32keV_2mGy_hTIE_0107.tif is the name of the 32-bit image and 32keV_2mGy_hTIE_0107.dcm is the name assigned to the output 8-bit DICOM file. The resulting 8-bit images are shown in Figure 3.9. The MPVs in the glandular and adipose regions remain relatively constant between the two images. This ensures an equivalent display of the two images, eliminating the previously described false contrast differences between the two imaging conditions.

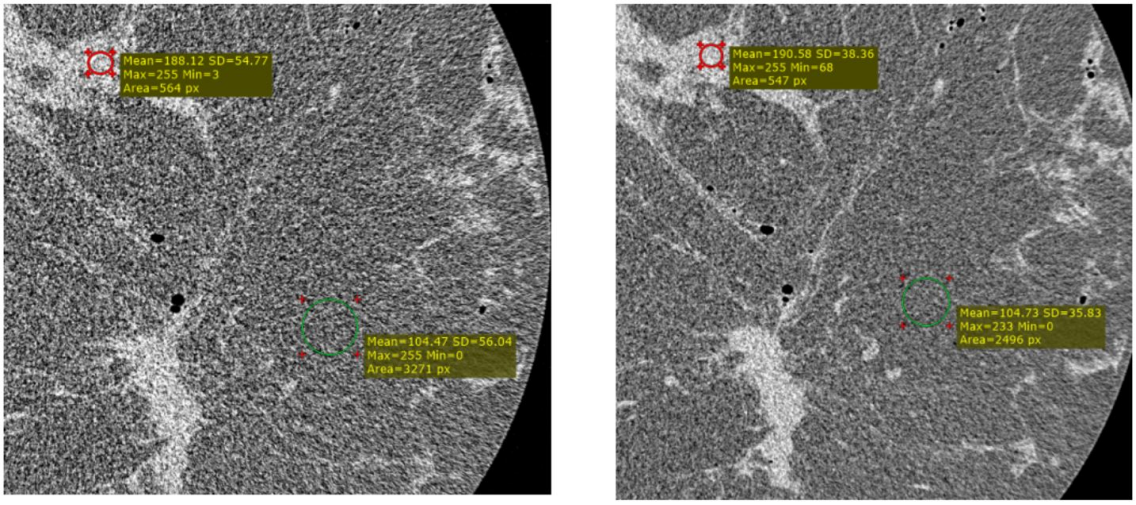


***Figure 3.9:*** *8-bit DICOM images converted from original 32-bit images using the proposed window for a 32 keV image which is shown in Figure 3.8. The 32keV-2mGy-hTIE image is shown on the left and the 32keV-4mGy-hTIE image is shown on the right. The MPVs in the glandular and adipose regions remain relatively constant between the two images.*

# Chapter 4

# Discussion

Mathematical models to predict subjective clinical image quality have been an area of research for many decades. Much of this research involves investigating relationships between imaging system characteristics such as NEQ and DQE and subjective clinical image quality. The success of establishing such a relationship is limited by the complex, variable anatomy found in clinical images. In thin slice breast CT imaging, the visibility of pathology is limited by system noise rather than anatomical background, unlike many projection radiographic images. Therefore, the likelihood of establishing a relationship between image-based objective measures and overall subjective clinical image quality is greatly improved. This study has successfully combined quantitative, image-based measures of three fundamental image quality attributes: contrast, noise and spatial resolution and weighted them appropriately to form a single predictive image quality metric (weighted CNR/res). Assuming radiologists' clinical image quality assessments correlate with diagnostic performance, this metric can be used to reduce the cost and time required for such assessments. Unlike previous objective image quality models [92, 104, 105, 106, 107, 108], this approach is based on the recently discovered fundamental physical principle of noise-resolution uncertainty [124]. This principle estimates the objective (Shannon) information contained in images that are collected at a given radiation dose [103]. The information is traced to the interaction of individual X-ray photons with matter in the imaged tissue. These interactions are the only real mechanism in X-ray imaging that provides information about the composition and density of the imaged sample at different points in three dimensions.

Of the three spatial resolution measurement methods, the "perceived" spatial resolution method implemented in 3D Slicer provides results that have the highest correlation with the subjective radiologist scores. This spatial resolution method also results in values that are closest (lowest MAE) to the subjective radiologist scores (as seen in Figure 3.4). As demonstrated in Figure 3.4, the "perceived" spatial resolution method provides results that indicate almost all PB-CT image sets have tissue interfaces that appear sharper, despite their absolute spatial resolution being either equal to, or less than, the corresponding AB-CT image sets. In this study, the radiologists indicated that almost every PB-CT image set had superior image quality compared to the corresponding AB-CT image sets. Use

of the "perceived" spatial resolution method readily allows the calculation of a CNR/res criterion which is consistently higher for the PB-CT images. The "absolute" spatial resolution method (implemented in 3D Slicer) provides a relative measure of PB-CT spatial resolution that shows similar results to the X-TRACT spatial resolution measurement method. This provides some validation to the experimental "absolute" spatial resolution method used in this study. The X-TRACT results indicate that a CNR/res criterion that uses a measure of the absolute spatial resolution can be used to adequately predict the subjective radiologist scores with the use of an offset factor added to all the CNR/res scores.

The un-scaled contrast scores measured using both methods showed a high correlation to the subjective radiologist scores, indicating that clinical image quality is limited more by contrast rather than other factors, which agrees well with previous studies [125, 126]. Both the spatial resolution methods implemented in 3D Slicer showed a significant correlation with the subjective radiologist scores, indicating that high spatial resolution is also a significant contributor to clinical image quality. Therefore, overall clinical image quality is dominated by contrast and spatial resolution. When the dose is fixed, the SNR is inversely related to spatial resolution. The measured SNR score using both methods had an insignificant, negative correlation to the subjective radiologist scores for groups of patients. This indicates that under the conditions of the considered experiments the SNR is the lowest valued component when assessing clinical image quality. However, it is necessary to include some weighting for SNR to optimise the correlation between the weighted CNR/res and subjective radiologist scores, indicating that it does influence clinical image quality.

Using appropriate weighting factors, the weighted CNR/res score (averaged across all samples) measured using X-TRACT has the highest correlation with the subjective radiologist scores averaged across all radiologists and samples. Additionally, with an offset value of 0.55, the CNR/res scores measured with X-TRACT can closely predict the absolute value of the radiologist scores averaged across all samples. This demonstrates the weighted CNR/res score has the potential to be an excellent predictor of the imaging conditions which are generally preferred by radiologists for groups of patients. A good correlation and small MAE was found between the weighted CNR/res (perc) scores (measured with 3D Slicer) and the radiologist scores for individual patients, indicating that this is a good predictor of preferred imaging conditions for individual patients.

Section 3.4 demonstrates that false contrast differences have been introduced between the images presented to radiologists for scoring in some cases. These contrast differences appear to be the result of suboptimal scaling when converting from the original 32-bit greyscale images to the 8-bit greyscale images used for presentation. This false contrast has likely affected the radiologist scores. With reference to the blue line in Figures 3.3 & 3.5, the average radiologist score (averaged across all samples) for both the

32keV-2mGy-hTIE and 32keV-4mGy-hTIE imaging conditions is almost identical. In theory, these images should have similar contrast and resolution, with the only difference being that the 4 mGy images should have significantly improved SNR. Therefore, the 4 mGy images should have a higher radiologist score compared to the 2 mGy images. With reference to the red lines in Figures 3.3 & 3.5, it can be seen that the 2 mGy images have higher contrast compared to the 4 mGy images. To the radiologists, the higher contrast visible in the 2 mGy images may have compensated for the lower SNR relative to the 4 mGy images. As previously mentioned, clinical image quality is limited mostly by contrast, indicating that any false contrast introduced through inconsistent display could significantly affect the radiologist scores. Likewise, artificial differences in pixel values have been introduced in the half and full TIE reconstructions, again possibly affecting the radiologists' preference between these two levels of phase-retrieval. Clinical image quality appears to be limited by spatial resolution rather than SNR resulting in radiologists preferring half TIE reconstructions. Section 3.4 proposes a method to convert the original 32-bit greyscale images into 8-bit greyscale images using fixed conversion windows. This method is intended to eliminate differences in contrast due to inconsistent image display while maintaining contrast differences due only to physical inherence such as X-ray energy.

Further research is required to investigate the feasibility of using this method for effectively predicting the clinical image quality assessed by radiologists in other areas of radiological examinations besides mammography. Thin slice breast CT, with reduced anatomical background presents a relatively simple case for the application of objective image quality assessment models. The scaling factors used in this study are evidently dependent on the software method used to calculate the contrast, SNR and spatial resolution. They are also likely dependent on the imaging modality and imaged anatomy. Although the subjective radiologist scores were collected in such a way as to reduce variability, the dependency of the weighting factors on the cohort of radiologists used to assess the images also requires further investigation. The automatic, relative spatial resolution measurement methods implemented in 3D Slicer are also unlikely to translate effectively to images of other types of anatomy and modalities. In breast imaging, the only two main tissue types present in an image are glandular and adipose. The presence of only two tissue types considerably simplifies automatic segmentation and implementation of automatic edge profile measurements. For images of other types of anatomy or modalities, the "perceived" spatial resolution method could be substituted with the use of an edge profile, or the average of several edge profiles, placed on sharp edges located on both test and reference images (such as the approach used to quantify rib sharpness in [105]). The use of "thick lines" which are averaged across a range of pixels (such as those available in the Fiji software [127]) may be useful to reduce the high level of noise generally found in standard edge profile plots. It is likely that the discrepancy between the "perceived" and "absolute" spatial resolution measurements will not be observed beyond the case where phase-contrast images are compared to attenuation-based images. A more systematic approach to optimising the weighting factors used to establish a correlation between the

weighted CNR/res score and the subjective radiologist scores could be investigated. It is also likely that the relationship between the image-based quantitative measures and subjective image quality is not linear [92], as is assumed in this study. The relationship between the quantitative image metrics and subjective image quality could be investigated further. A remaining limitation of this, and other proposed image quality assessment models, is the assumption that radiologist clinical image quality assessment will correlate with task-specific diagnostic performance. Further research is required to investigate the validity of this assumption, possibly allowing image quality assessment models to directly predict task-specific diagnostic performance.

# Chapter 5

# Conclusion

The scaled CNR/res criterion has been demonstrated as a quantitative image assessment model that effectively predicts the relative clinical image quality, as assessed by radiologists, in the context of PB-CT breast imaging. Furthermore, the scaled CNR/res criterion can predict the imaging conditions that are generally preferred for a group of patients and optimal imaging conditions for individual patient anatomy. This has the potential to allow optimisation of radiological imaging conditions at significantly reduced time and cost while improving consistency of results.

# Appendix A

# Additional Results

## A.1 Subjective Radiologist Assessment

| Standard Deviations of Radiologist Scores | | | | | | |
|---|---|---|---|---|---|---|
| Sample Number: | 2370691 | 4247239 | 4638975 | 4704628 | 7096050L | 709605R |
| 32keV-2mGy-fTIE | 0.45 | 0.50 | 0.79 | 0.99 | 0.66 | 0.88 |
| 32keV-2mGy-hTIE | 0.39 | 0.89 | 0.88 | 1.00 | 1.23 | 0.83 |
| 32keV-4mGy-fTIE | 0.51 | 0.64 | 0.83 | 0.50 | 0.50 | 0.57 |
| 32keV-4mGy-hTIE | 0.50 | 0.48 | 0.57 | 0.77 | 0.64 | 0.50 |
| 34keV-2mGy-fTIE | 0.79 | 0.74 | 0.89 | 0.74 | 0.79 | 0.51 |
| 34keV-2mGy-hTIE | 0.51 | 0.75 | 0.86 | 0.86 | 0.90 | 0.88 |
| 34keV-4mGy-fTIE | 0.66 | 0.72 | 0.50 | 0.75 | 0.39 | 0.77 |
| 34keV-4mGy-hTIE | 0.64 | 0.74 | 0.45 | 0.50 | 0.50 | 0.79 |

***Table A.1:*** *Standard deviations of radiologist scores for the first six samples*

| Standard Deviations of Radiologist Scores | | | | | | |
|---|---|---|---|---|---|---|
| Sample Number: | 7104092 | 7949430 | 8283541L | 8283541R | 8413420 | 8423990 |
| 32keV-2mGy-fTIE | 0.77 | 0.86 | 0.77 | 0.75 | 0.57 | 0.85 |
| 32keV-2mGy-hTIE | 1.14 | 1.11 | 0.85 | 0.89 | 1.28 | 1.14 |
| 32keV-4mGy-fTIE | 0.51 | 0.79 | 0.64 | 0.48 | 0.72 | 0.29 |
| 32keV-4mGy-hTIE | 0.57 | 0.57 | 0.64 | 0.48 | 0.62 | 0.77 |
| 34keV-2mGy-fTIE | 0.62 | 0.83 | 0.57 | 0.79 | 0.66 | 1.14 |
| 34keV-2mGy-hTIE | 0.90 | 0.99 | 0.86 | 0.86 | 0.98 | 0.74 |
| 34keV-4mGy-fTIE | 0.64 | 0.79 | 0.39 | 0.74 | 0.78 | 0.88 |
| 34keV-4mGy-hTIE | 0.64 | 0.66 | 0.39 | 0.45 | 0.48 | 0.66 |

***Table A.2:*** *Standard deviations of radiologist scores for the last six samples*

## A.2 Additional X-TRACT Results

| Subjective Scores Vs Un-scaled Quantitative "Scores" (X-TRACT) | | | | | |
|---|---|---|---|---|---|
| | Radiologist Average | Contrast Score | SNR Score | Resolution Score | CNR/res Score |
| 32keV-2mGy-fTIE | 0.95 | 0.26 | -0.27 | -0.04 | -0.04 |
| 32keV-2mGy-hTIE | 1.12 | 0.45 | -0.80 | 0.00 | -0.24 |
| 32keV-4mGy-fTIE | 0.94 | 0.15 | 0.16 | -0.04 | 0.26 |
| 32keV-4mGy-hTIE | 1.11 | 0.24 | -0.22 | 0.00 | 0.02 |
| 34keV-2mGy-fTIE | 0.45 | 0.09 | 0.00 | -0.05 | 0.03 |
| 34keV-2mGy-hTIE | 0.65 | 0.20 | -0.40 | -0.01 | -0.17 |
| 34keV-4mGy-fTIE | 0.36 | 0.02 | 0.43 | -0.05 | 0.35 |
| 34keV-4mGy-hTIE | 0.58 | 0.06 | 0.07 | -0.01 | 0.11 |

***Table A.3:*** *Subjective radiologist scores for each imaging condition averaged across all radiologists and all samples vs various un-scaled quantitative "scores" calculated using X-TRACT.*

| Subjective Scores Vs Scaled Quantitative "Scores" (X-TRACT) | | | | | |
|---|---|---|---|---|---|
| | Radiologist Average | Contrast Score | SNR Score | Resolution Score | CNR/res Score |
| 32keV-2mGy-fTIE | 0.95 | 0.98 | -0.23 | -0.22 | 0.83 |
| 32keV-2mGy-hTIE | 1.12 | 1.67 | -0.66 | 0.02 | 1.15 |
| 32keV-4mGy-fTIE | 0.94 | 0.51 | 0.15 | -0.23 | 0.88 |
| 32keV-4mGy-hTIE | 1.11 | 0.89 | -0.19 | -0.02 | 1.07 |
| 34keV-2mGy-fTIE | 0.45 | 0.24 | 0.00 | -0.30 | 0.37 |
| 34keV-2mGy-hTIE | 0.65 | 0.75 | -0.34 | -0.04 | 0.74 |
| 34keV-4mGy-fTIE | 0.36 | -0.20 | 0.39 | -0.27 | 0.46 |
| 34keV-4mGy-hTIE | 0.58 | 0.08 | 0.07 | -0.04 | 0.64 |

***Table A.4:*** *Subjective radiologist scores for each imaging condition averaged across all radiologists and all samples vs various scaled quantitative "scores" calculated using X-TRACT. The scaling factors applied to each ratio were; 3.4 for the contrast ratio, 0.9 for the SNR ratio and 6 for the spatial resolution ratio.*

| Subjective Scores Vs Scaled & Offset Quantitative "Scores" (X-TRACT) | | | | | |
|---|---|---|---|---|---|
| | Radiologist Average | Contrast Score | SNR Score | Resolution Score | CNR/res Score |
| 32keV-2mGy-fTIE | 0.95 | 0.98 | -0.23 | -0.22 | 0.28 |
| 32keV-2mGy-hTIE | 1.12 | 1.67 | -0.66 | 0.02 | 0.62 |
| 32keV-4mGy-fTIE | 0.94 | 0.51 | 0.15 | -0.23 | 0.33 |
| 32keV-4mGy-hTIE | 1.11 | 0.89 | -0.19 | -0.02 | 0.53 |
| 34keV-2mGy-fTIE | 0.45 | 0.24 | 0.00 | -0.30 | -0.18 |
| 34keV-2mGy-hTIE | 0.65 | 0.75 | -0.34 | -0.04 | 0.19 |
| 34keV-4mGy-fTIE | 0.36 | -0.20 | 0.39 | -0.27 | -0.09 |
| 34keV-4mGy-hTIE | 0.58 | 0.08 | 0.07 | -0.04 | 0.09 |

***Table A.5:*** *Subjective radiologist scores for each imaging condition averaged across all radiologists and all samples vs various scaled quantitative "scores" calculated using X-TRACT. The scaling factors applied to each ratio were; 3.4 for the contrast ratio, 0.9 for the SNR ratio and 6 for the spatial resolution ratio. An offset of 0.55 was applied to the CNR/res scores.*

### A.2.1 X-TRACT Plots for Individual Samples

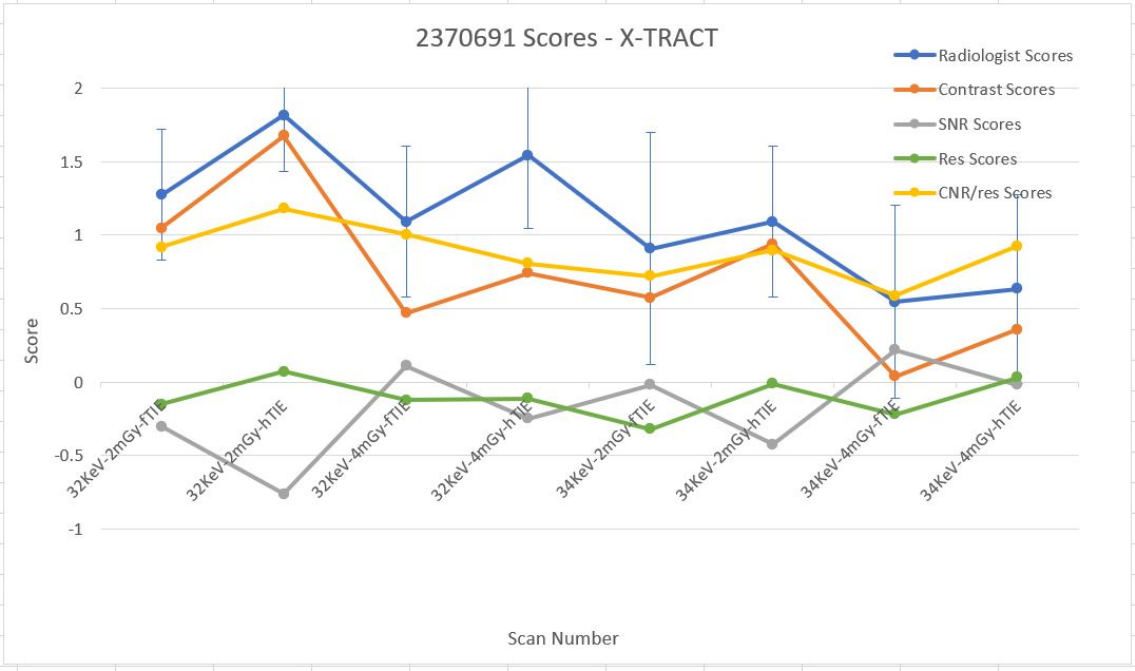


***Figure A.1:*** *Plot of subjective radiologist scores (in blue) for each imaging condition for sample 2370691 (shown in Table 3.2), with error bars of ± one standard deviation (shown in Table A.1). The subjective radiologist score is compared to various scaled quantitative scores measured using X-TRACT including; CNR/res (yellow), contrast (red), SNR (grey) and spatial resolution (green) for sample 2370691.*

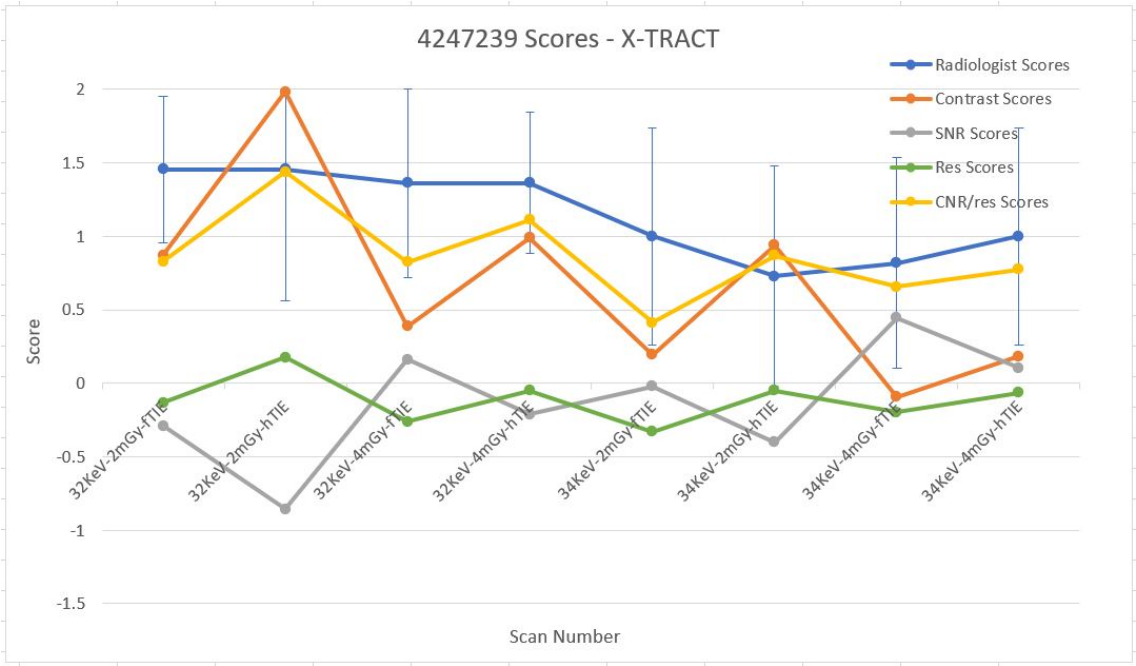


***Figure A.2:*** *Plot of subjective radiologist scores (in blue) for each imaging condition for sample 4247239 (shown in Table 3.2), with error bars of ± one standard deviation (shown in Table A.1). The subjective radiologist score is compared to various scaled quantitative scores measured using X-TRACT including; CNR/res (yellow), contrast (red), SNR (grey) and spatial resolution (green) for sample 4247239.*

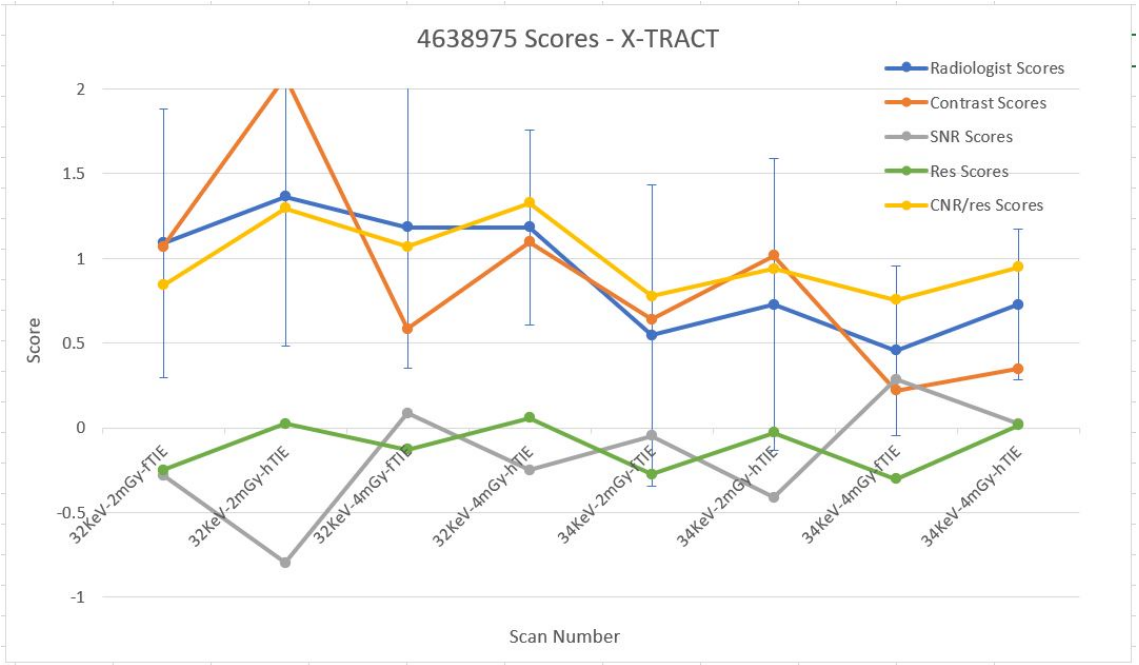


***Figure A.3:*** *Plot of subjective radiologist scores (in blue) for each imaging condition for sample 4638975 (shown in Table 3.2), with error bars of ± one standard deviation (shown in Table A.1). The subjective radiologist score is compared to various scaled quantitative scores measured using X-TRACT including; CNR/res (yellow), contrast (red), SNR (grey) and spatial resolution (green) for sample 4638975.*

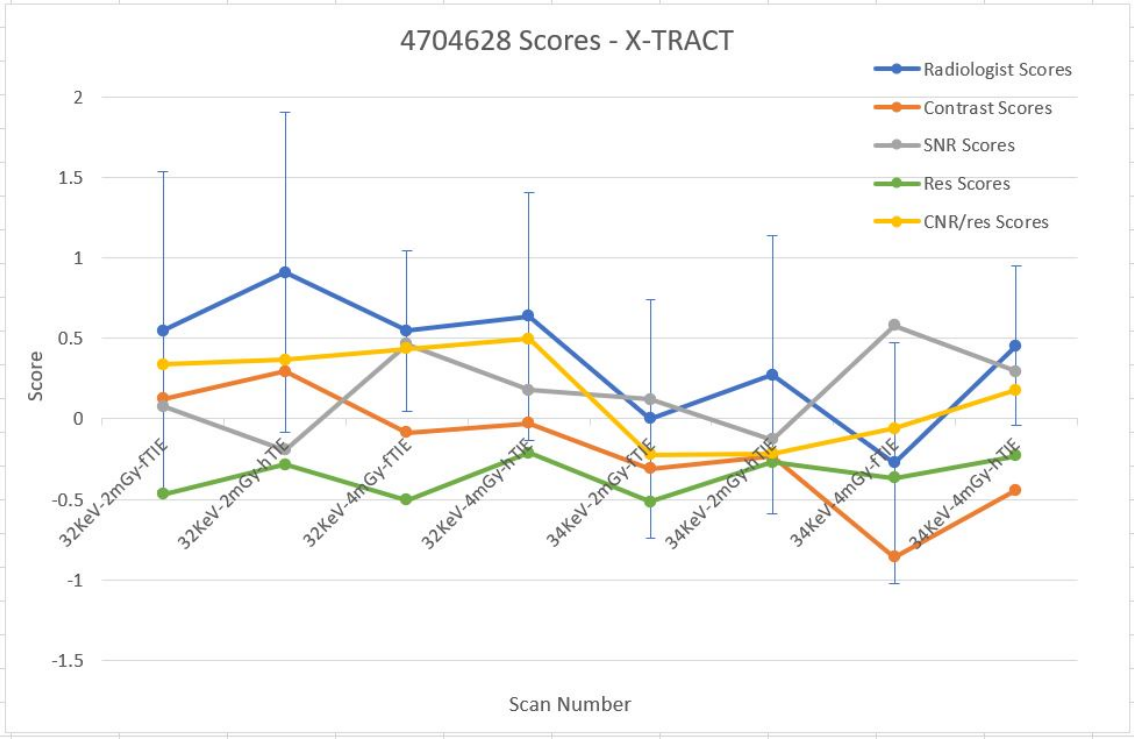


***Figure A.4:*** *Plot of subjective radiologist scores (in blue) for each imaging condition for sample 4704628 (shown in Table 3.2), with error bars of ± one standard deviation (shown in Table A.1). The subjective radiologist score is compared to various scaled quantitative scores measured using X-TRACT including; CNR/res (yellow), contrast (red), SNR (grey) and spatial resolution (green) for sample 4704628.*

| Scaled CNR/res Scores - X-TRACT | | | | | | |
|---|---|---|---|---|---|---|
| Imaging Condition | 2370691 | 4247239 | 4638975 | 4704628 | 7096050L | 709605R |
| 32KeV-2mGy-fTIE | 0.92 | 0.83 | 0.84 | 0.34 | 0.56 | 1.22 |
| 32KeV-2mGy-hTIE | 1.18 | 1.44 | 1.30 | 0.37 | 0.95 | 1.31 |
| 32KeV-4mGy-fTIE | 1.01 | 0.83 | 1.07 | 0.44 | 0.81 | 1.12 |
| 32KeV-4mGy-hTIE | 0.81 | 1.11 | 1.33 | 0.50 | 0.99 | 1.41 |
| 34KeV-2mGy-fTIE | 0.72 | 0.41 | 0.78 | -0.22 | 0.45 | 0.77 |
| 34KeV-2mGy-hTIE | 0.90 | 0.87 | 0.94 | -0.21 | 0.67 | 0.92 |
| 34KeV-4mGy-fTIE | 0.59 | 0.65 | 0.75 | -0.06 | 0.00 | 0.90 |
| 34KeV-4mGy-hTIE | 0.93 | 0.78 | 0.95 | 0.18 | 0.36 | 0.97 |

***Table A.6:*** *Scaled CNR/res scores measured using X-TRACT for the first six samples. A green colored cell indicates that the scaled CNR/res score is within 1 standard deviation of the corresponding subjective radiologist score, while a yellow cell indicates that the scaled CNR/res score is outside 1 standard deviation.*

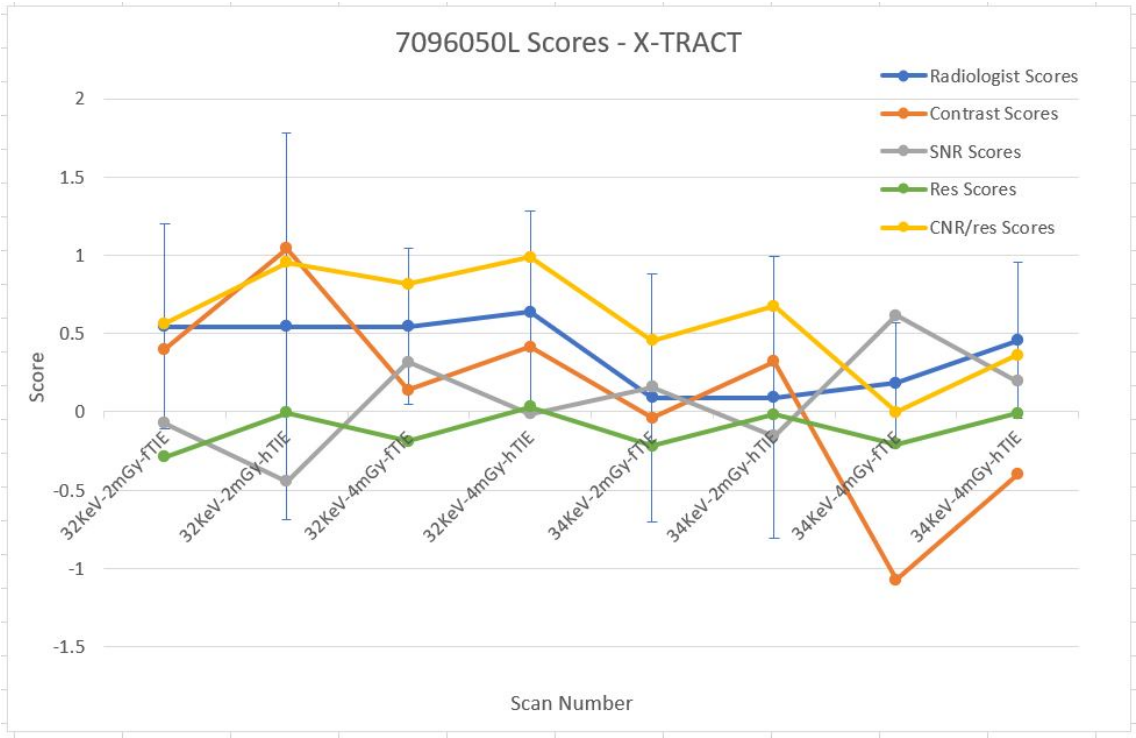


***Figure A.5:*** *Plot of subjective radiologist scores (in blue) for each imaging condition for sample 7096050L (shown in Table 3.2), with error bars of ± one standard deviation (shown in Table A.1). The subjective radiologist score is compared to various scaled quantitative scores measured using X-TRACT including; CNR/res (yellow), contrast (red), SNR (grey) and spatial resolution (green) for sample 7096050L.*

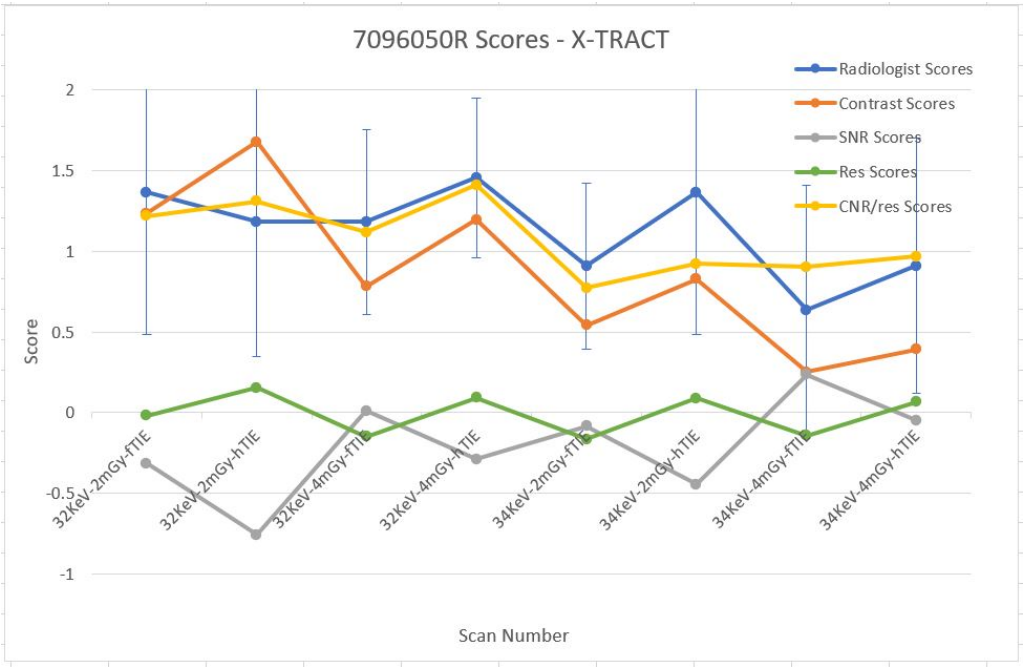


***Figure A.6:*** *Plot of subjective radiologist scores (in blue) for each imaging condition for sample 7096050R (shown in Table 3.2), with error bars of ± one standard deviation (shown in Table A.1). The subjective radiologist score is compared to various scaled quantitative scores measured using X-TRACT including; CNR/res (yellow), contrast (red), SNR (grey) and spatial resolution (green) for sample 7096050R.*

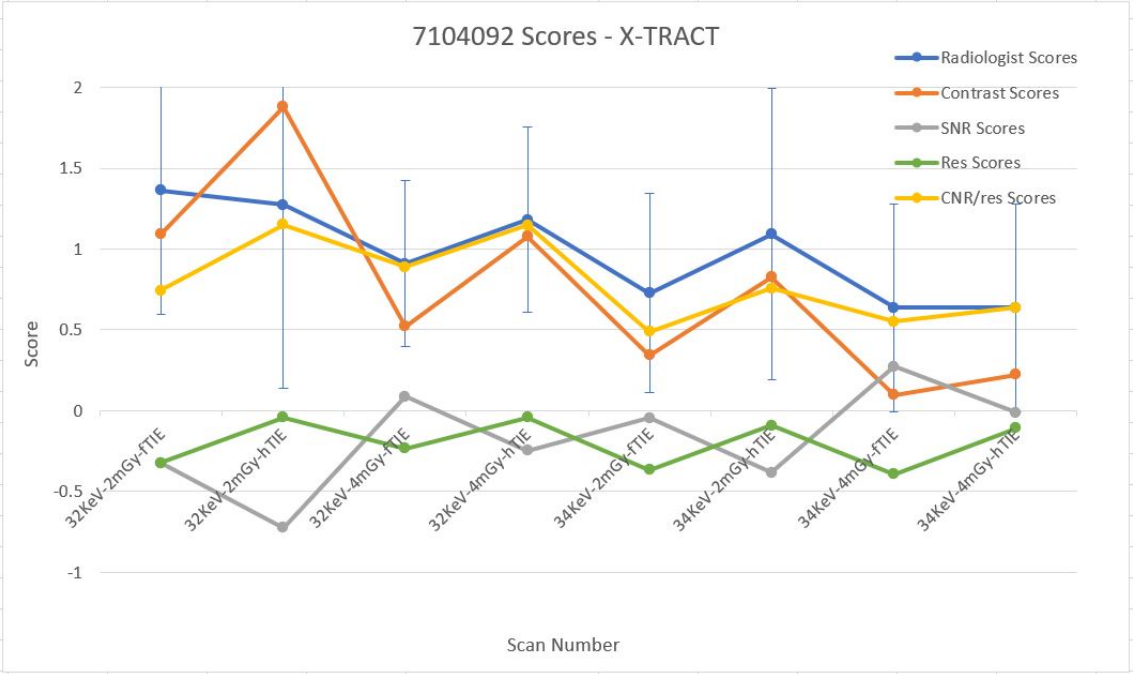


***Figure A.7:*** *Plot of subjective radiologist scores (in blue) for each imaging condition for sample 7104092 (shown in Table 3.2), with error bars of ± one standard deviation (shown in Table A.1). The subjective radiologist score is compared to various scaled quantitative scores measured using X-TRACT including; CNR/res (yellow), contrast (red), SNR (grey) and spatial resolution (green) for sample 7104092.*

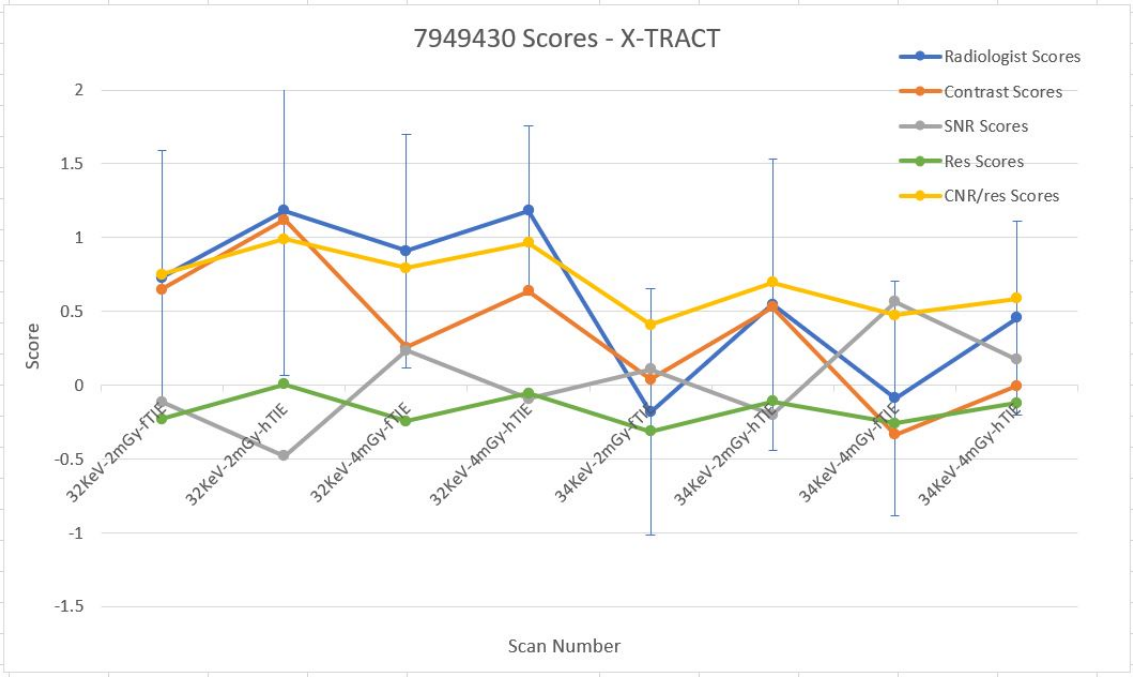


***Figure A.8:*** *Plot of subjective radiologist scores (in blue) for each imaging condition for sample 7949430 (shown in Table 3.2), with error bars of ± one standard deviation (shown in Table A.1). The subjective radiologist score is compared to various scaled quantitative scores measured using X-TRACT including; CNR/res (yellow), contrast (red), SNR (grey) and spatial resolution (green) for sample 7949430.*

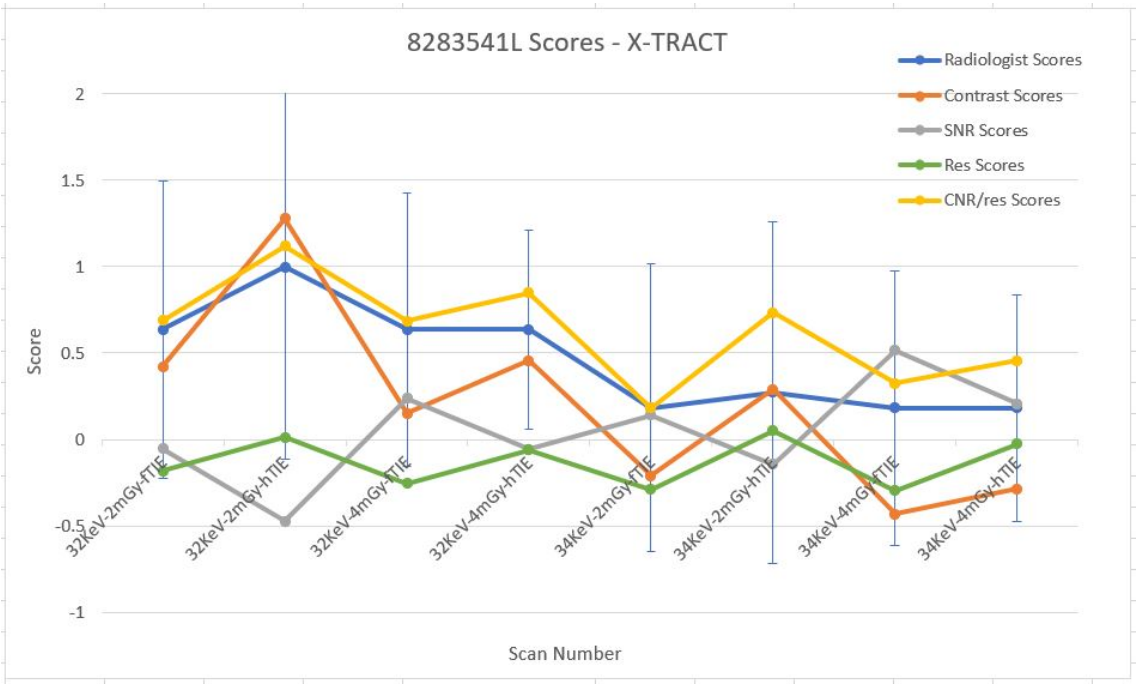


***Figure A.9:*** *Plot of subjective radiologist scores (in blue) for each imaging condition for sample 8283541L (shown in Table 3.2), with error bars of ± one standard deviation (shown in Table A.1). The subjective radiologist score is compared to various scaled quantitative scores measured using X-TRACT including; CNR/res (yellow), contrast (red), SNR (grey) and spatial resolution (green) for sample 8283541L.*

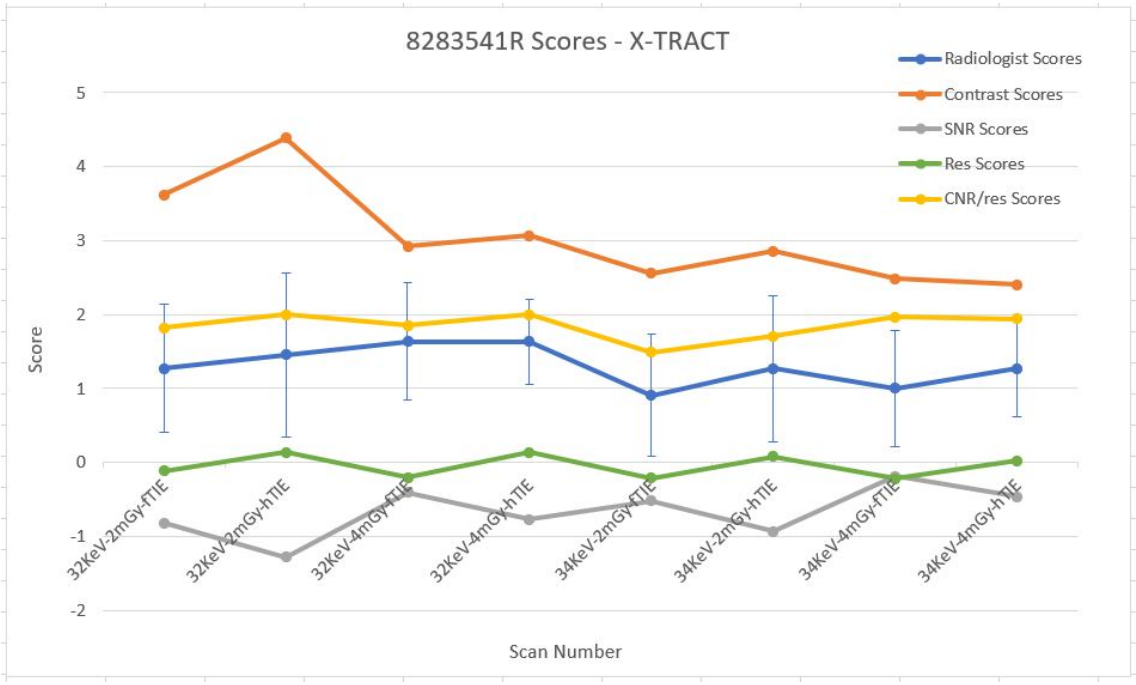


***Figure A.10:*** *Plot of subjective radiologist scores (in blue) for each imaging condition for sample 8283541R (shown in Table 3.2), with error bars of ± one standard deviation (shown in Table A.1). The subjective radiologist score is compared to various scaled quantitative scores measured using X-TRACT including; CNR/res (yellow), contrast (red), SNR (grey) and spatial resolution (green) for sample 8283541R.*

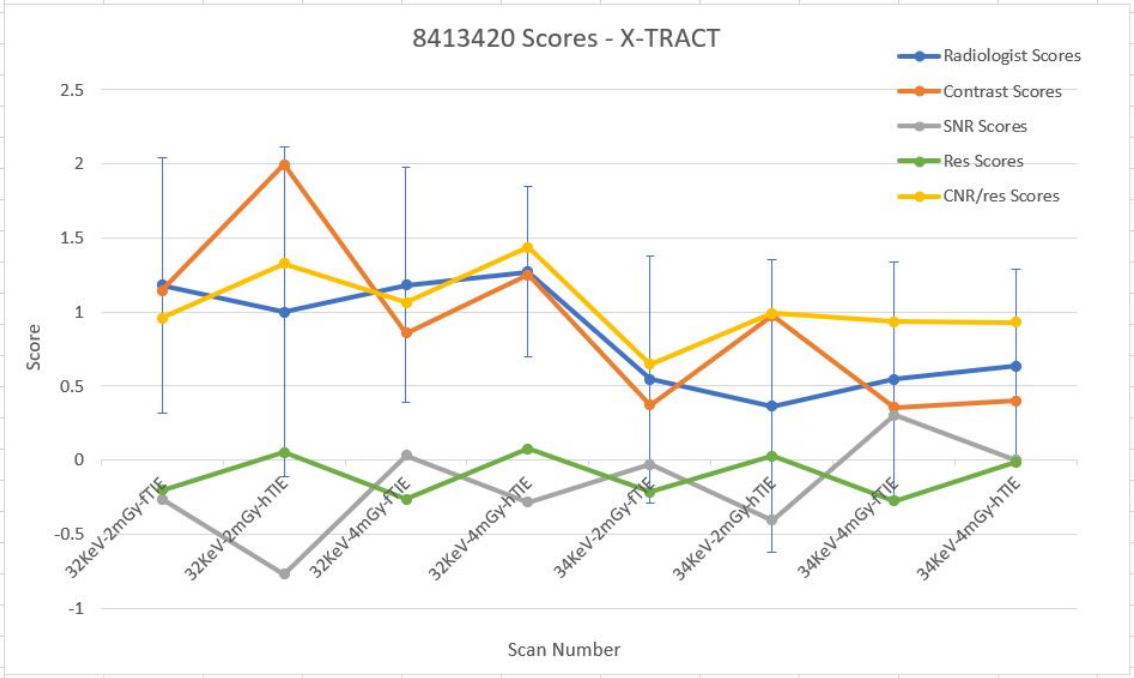


***Figure A.11:*** *Plot of subjective radiologist scores (in blue) for each imaging condition for sample 8413420 (shown in Table 3.2), with error bars of ± one standard deviation (shown in Table A.1). The subjective radiologist score is compared to various scaled quantitative scores measured using X-TRACT including; CNR/res (yellow), contrast (red), SNR (grey) and spatial resolution (green) for sample 8413420.*

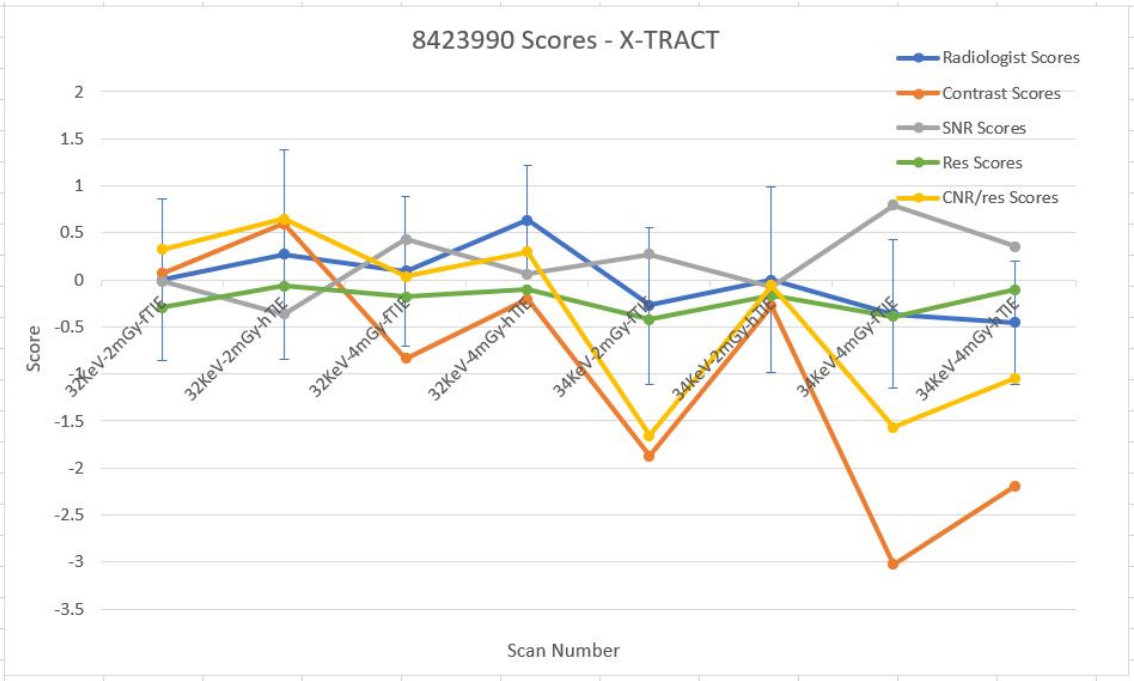


***Figure A.12:*** *Plot of subjective radiologist scores (in blue) for each imaging condition for sample 8423990 (shown in Table 3.2), with error bars of ± one standard deviation (shown in Table A.1). The subjective radiologist score is compared to various scaled quantitative scores measured using X-TRACT including; CNR/res (yellow), contrast (red), SNR (grey) and spatial resolution (green) for sample 8423990.*

| Scaled CNR/res Scores - X-TRACT | | | | | | |
|---|---|---|---|---|---|---|
| Imaging Condition | 7104092 | 7949430 | 8283541L | 8283541R | 8413420 | 8423990 |
| 32KeV-2mGy-fTIE | 0.74 | 0.75 | 0.69 | 1.82 | 0.96 | 0.32 |
| 32KeV-2mGy-hTIE | 1.15 | 0.99 | 1.12 | 2.00 | 1.33 | 0.65 |
| 32KeV-4mGy-fTIE | 0.89 | 0.79 | 0.69 | 1.86 | 1.07 | 0.04 |
| 32KeV-4mGy-hTIE | 1.15 | 0.96 | 0.85 | 2.00 | 1.44 | 0.30 |
| 34KeV-2mGy-fTIE | 0.49 | 0.41 | 0.18 | 1.49 | 0.65 | -1.66 |
| 34KeV-2mGy-hTIE | 0.76 | 0.70 | 0.74 | 1.71 | 0.99 | -0.06 |
| 34KeV-4mGy-fTIE | 0.55 | 0.47 | 0.33 | 1.96 | 0.93 | -1.57 |
| 34KeV-4mGy-hTIE | 0.64 | 0.59 | 0.46 | 1.94 | 0.93 | -1.04 |

***Table A.7:*** *Scaled CNR/res scores measured using X-TRACT for the first six samples. A green colored cell indicates that the scaled CNR/res score is within 1 standard deviation of the corresponding subjective radiologist score, while a yellow cell indicates that the scaled CNR/res score is outside 1 standard deviation.*

## A.3 Additional 3D Slicer Results

| Subjective Scores Vs Un-scaled Quantitative "Scores" (3D Slicer) | | | | | | |
|---|---|---|---|---|---|---|
| Imaging Condition | Radiologist Average | Contrast Score | SNR Score | Res (perc) Score | Res (abs) Score | CNR/res (perc) Score |
| 32keV-2mGy-fTIE | 0.95 | 0.12 | -0.21 | 0.33 | -0.09 | 0.26 |
| 32keV-2mGy-hTIE | 1.12 | 0.19 | -0.67 | 0.55 | 0.05 | 0.11 |
| 32keV-4mGy-fTIE | 0.94 | 0.10 | 0.19 | 0.25 | -0.14 | 0.69 |
| 32keV-4mGy-hTIE | 1.11 | 0.13 | -0.15 | 0.43 | 0.00 | 0.43 |
| 34keV-2mGy-fTIE | 0.45 | 0.02 | 0.03 | 0.17 | -0.16 | 0.26 |
| 34keV-2mGy-hTIE | 0.65 | 0.06 | -0.33 | 0.37 | -0.01 | 0.11 |
| 34keV-4mGy-fTIE | 0.36 | 0.02 | 0.46 | 0.10 | -0.23 | 0.67 |
| 34keV-4mGy-hTIE | 0.58 | 0.03 | 0.09 | 0.26 | -0.07 | 0.44 |

***Table A.8:*** *Subjective radiologist scores for each imaging condition averaged across all radiologists and all samples vs various un-scaled quantitative "scores" calculated using 3D Slicer.*

| Subjective Scores Vs Scaled Quantitative "Scores" (3D Slicer) | | | | | |
|---|---|---|---|---|---|
| Imaging Condition | Radiologist Average | Contrast Score | SNR Score | Res (perc) Score | CNR/res (perc) Score |
| 32keV-2mGy-fTIE | 0.95 | 0.15 | -0.06 | 0.71 | 0.84 |
| 32keV-2mGy-hTIE | 1.12 | 0.23 | -0.16 | 1.13 | 1.24 |
| 32keV-4mGy-fTIE | 0.94 | 0.12 | 0.07 | 0.56 | 0.88 |
| 32keV-4mGy-hTIE | 1.11 | 0.15 | -0.05 | 0.91 | 1.10 |
| 34keV-2mGy-fTIE | 0.45 | 0.02 | 0.01 | 0.40 | 0.45 |
| 34keV-2mGy-hTIE | 0.65 | 0.07 | -0.09 | 0.79 | 0.75 |
| 34keV-4mGy-fTIE | 0.36 | 0.02 | 0.16 | 0.25 | 0.48 |
| 34keV-4mGy-hTIE | 0.58 | 0.03 | 0.03 | 0.57 | 0.67 |

***Table A.9:*** *Subjective radiologist scores for each imaging condition averaged across all radiologists and all samples vs various scaled quantitative "scores" calculated using 3D Slicer. The scaling factors applied to each ratio were; 1.2 for the contrast ratio, 0.35 for the SNR ratio and 2 for the "perceived" spatial resolution ratio.*

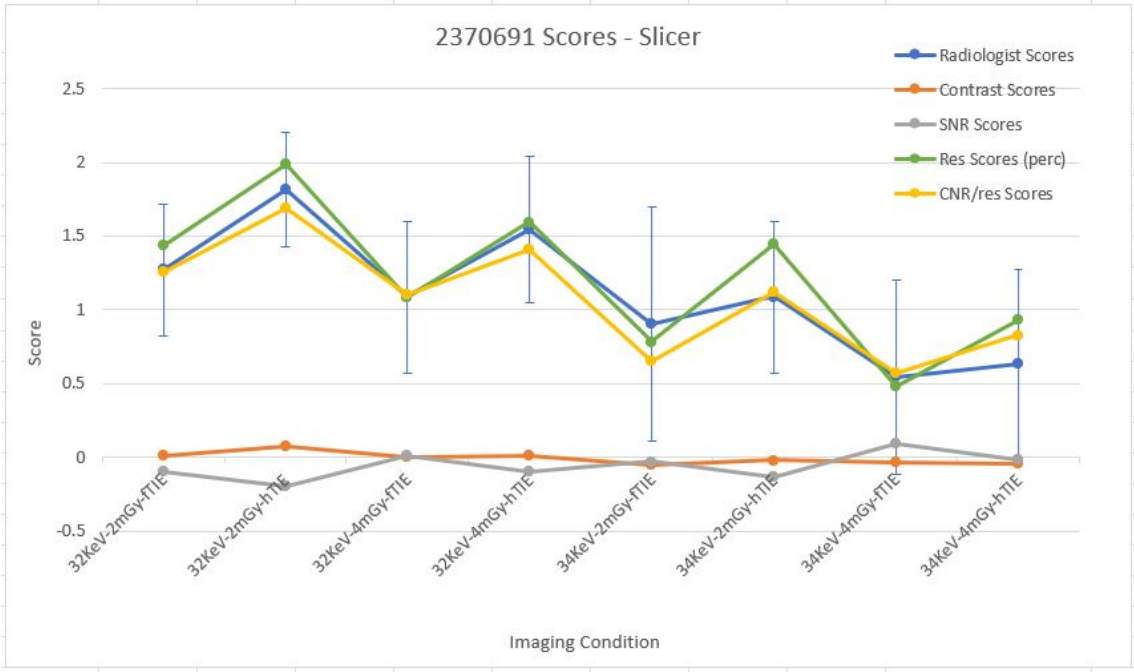


***Figure A.13:*** *Plot of subjective radiologist scores (in blue) for each imaging condition for sample 2370691 (shown in Table 3.2), with error bars of ± one standard deviation (shown in Table A.1). The subjective radiologist score is compared to various scaled quantitative scores measured using 3D Slicer including; CNR/res (yellow), contrast (red), SNR (grey) and spatial resolution (green) for sample 2370691.*

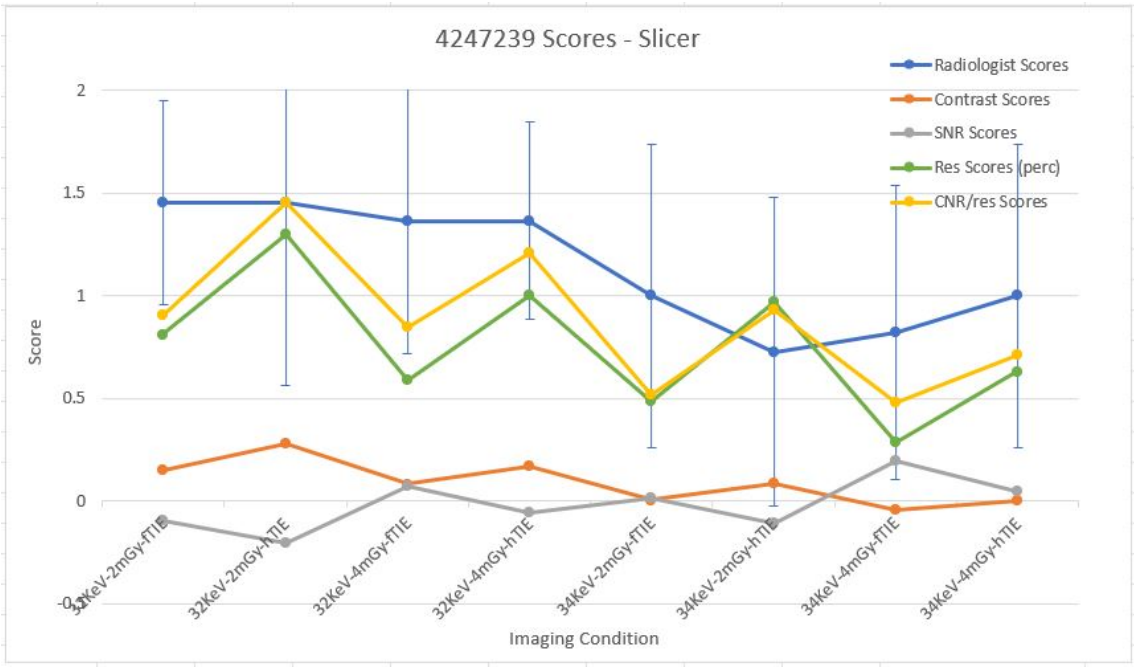


***Figure A.14:*** *Plot of subjective radiologist scores (in blue) for each imaging condition for sample 4247239 (shown in Table 3.2), with error bars of ± one standard deviation (shown in Table A.1). The subjective radiologist score is compared to various scaled quantitative scores measured using 3D Slicer including; CNR/res (yellow), contrast (red), SNR (grey) and spatial resolution (green) for sample 4247239.*

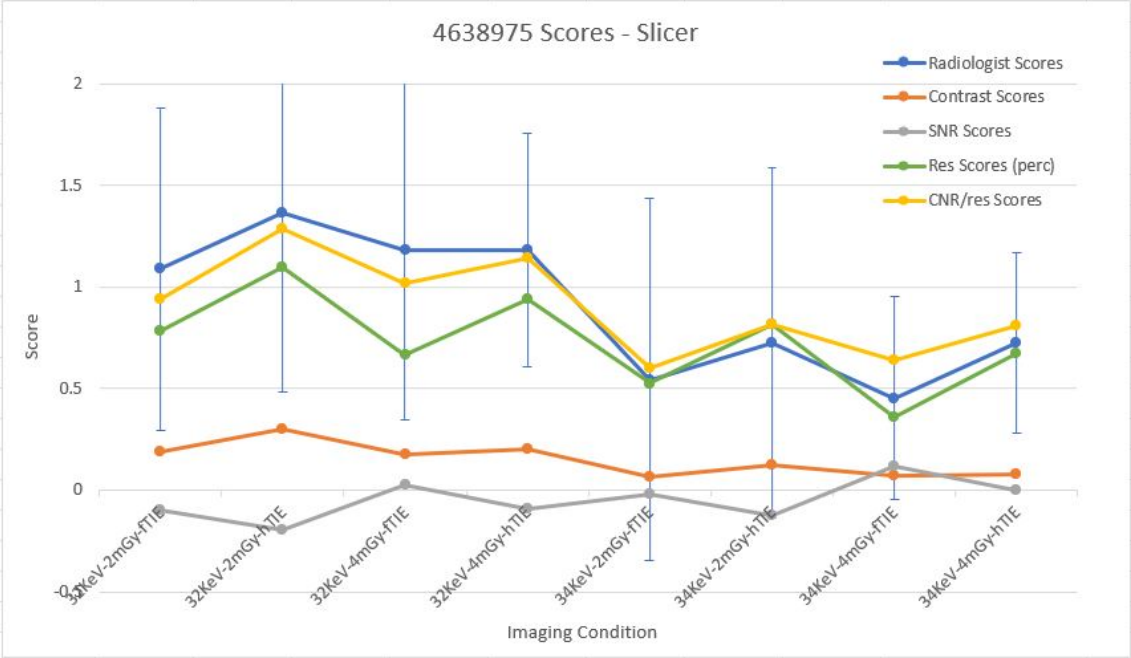


***Figure A.15:*** *Plot of subjective radiologist scores (in blue) for each imaging condition for sample 4638975 (shown in Table 3.2), with error bars of ± one standard deviation (shown in Table A.1). The subjective radiologist score is compared to various scaled quantitative scores measured using 3D Slicer including; CNR/res (yellow), contrast (red), SNR (grey) and spatial resolution (green) for sample 4638975.*

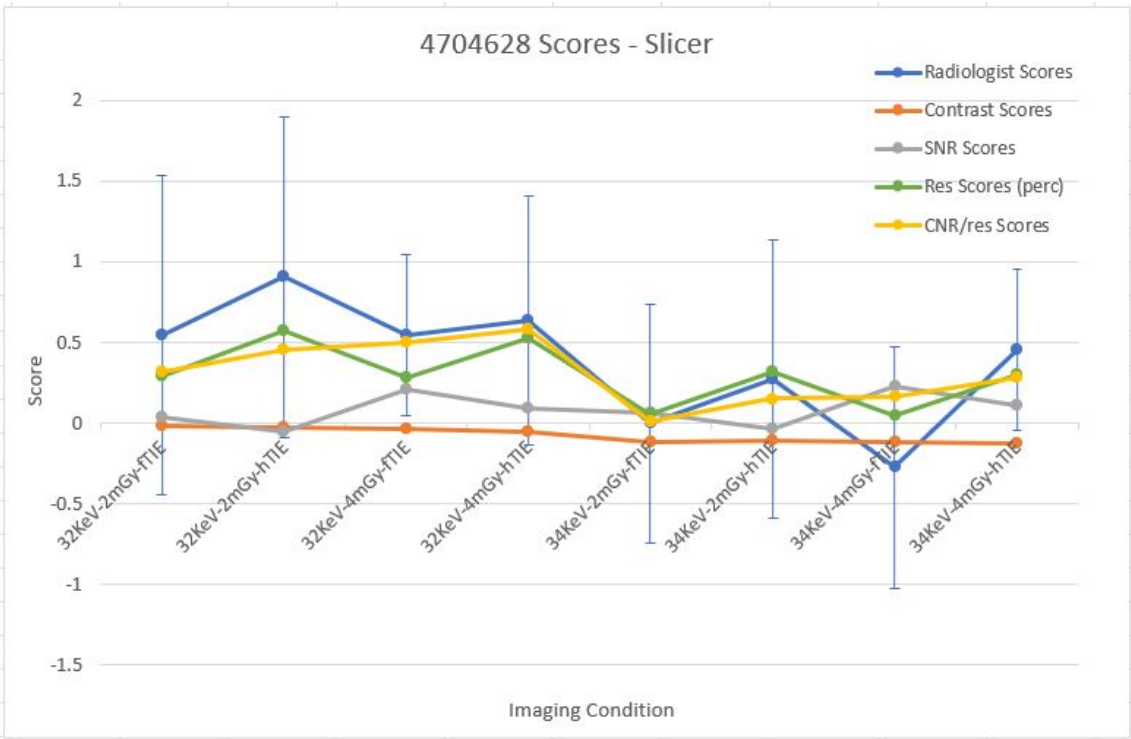


***Figure A.16:*** *Plot of subjective radiologist scores (in blue) for each imaging condition for sample 4704628 (shown in Table 3.2), with error bars of ± one standard deviation (shown in Table A.1). The subjective radiologist score is compared to various scaled quantitative scores measured using 3D Slicer including; CNR/res (yellow), contrast (red), SNR (grey) and spatial resolution (green) for sample 4704628.*

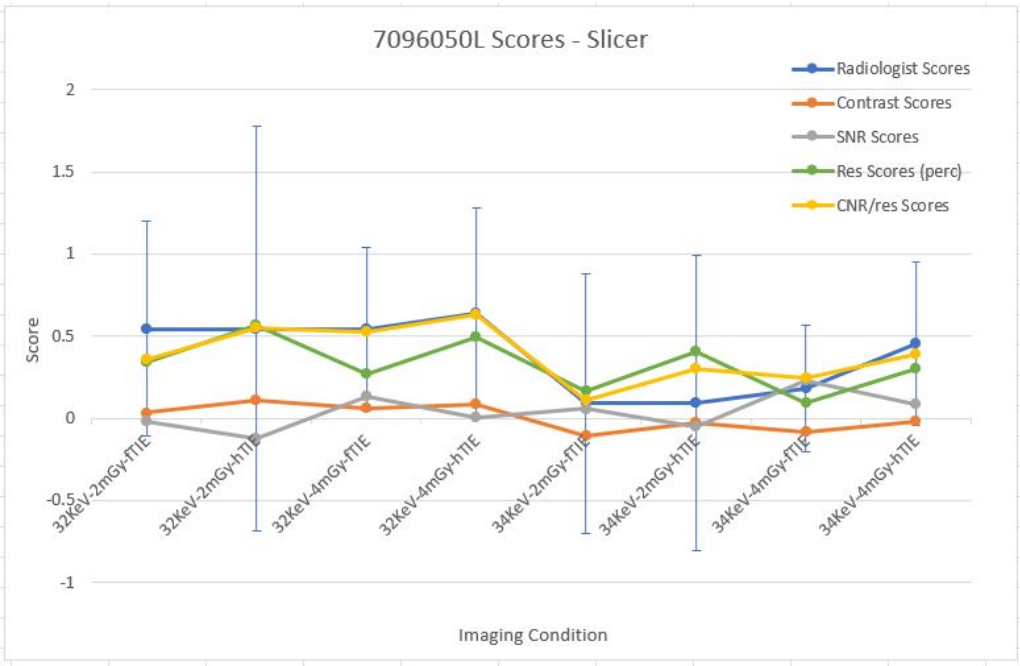


***Figure A.17:*** *Plot of subjective radiologist scores (in blue) for each imaging condition for sample 7096050L (shown in Table 3.2), with error bars of ± one standard deviation (shown in Table A.1). The subjective radiologist score is compared to various scaled quantitative scores measured using 3D Slicer including; CNR/res (yellow), contrast (red), SNR (grey) and spatial resolution (green) for sample 7096050L.*


***Figure A.18:*** *Plot of subjective radiologist scores (in blue) for each imaging condition for sample 7096050R (shown in Table 3.2), with error bars of ± one standard deviation (shown in Table A.1). The subjective radiologist score is compared to various scaled quantitative scores measured using 3D Slicer including; CNR/res (yellow), contrast (red), SNR (grey) and spatial resolution (green) for sample 7096050R.*

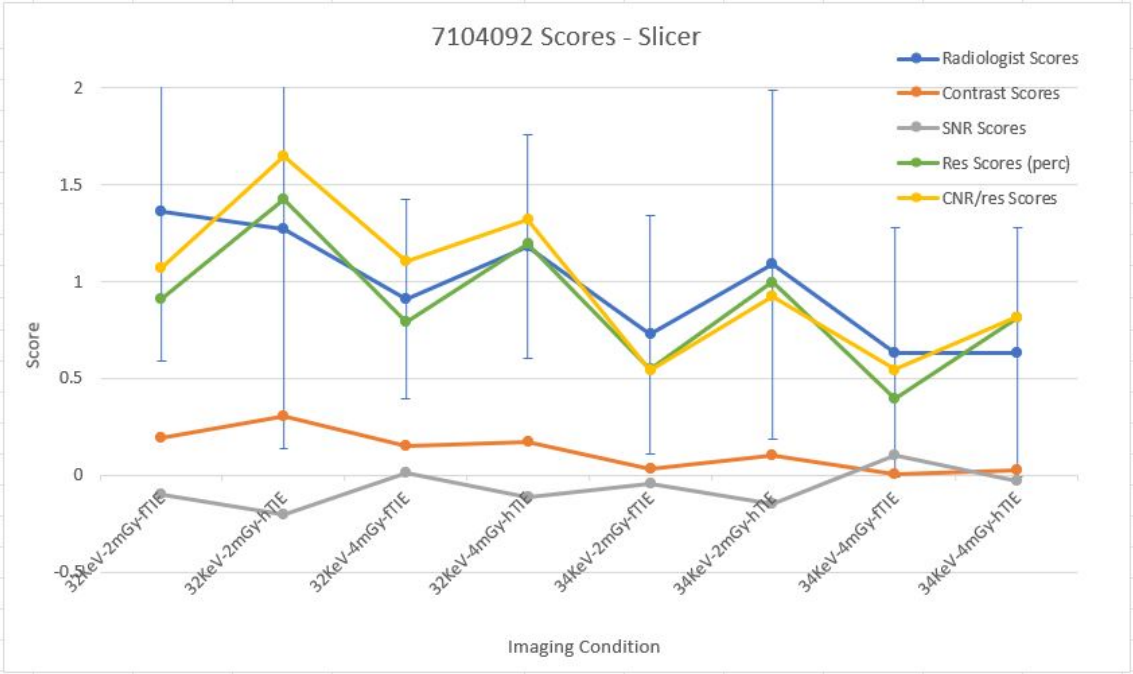


***Figure A.19:*** *Plot of subjective radiologist scores (in blue) for each imaging condition for sample 7104092 (shown in Table 3.3), with error bars of ± one standard deviation (shown in Table A.2). The subjective radiologist score is compared to various scaled quantitative scores measured using 3D Slicer including; CNR/res (yellow), contrast (red), SNR (grey) and spatial resolution (green) for sample 7104092.*

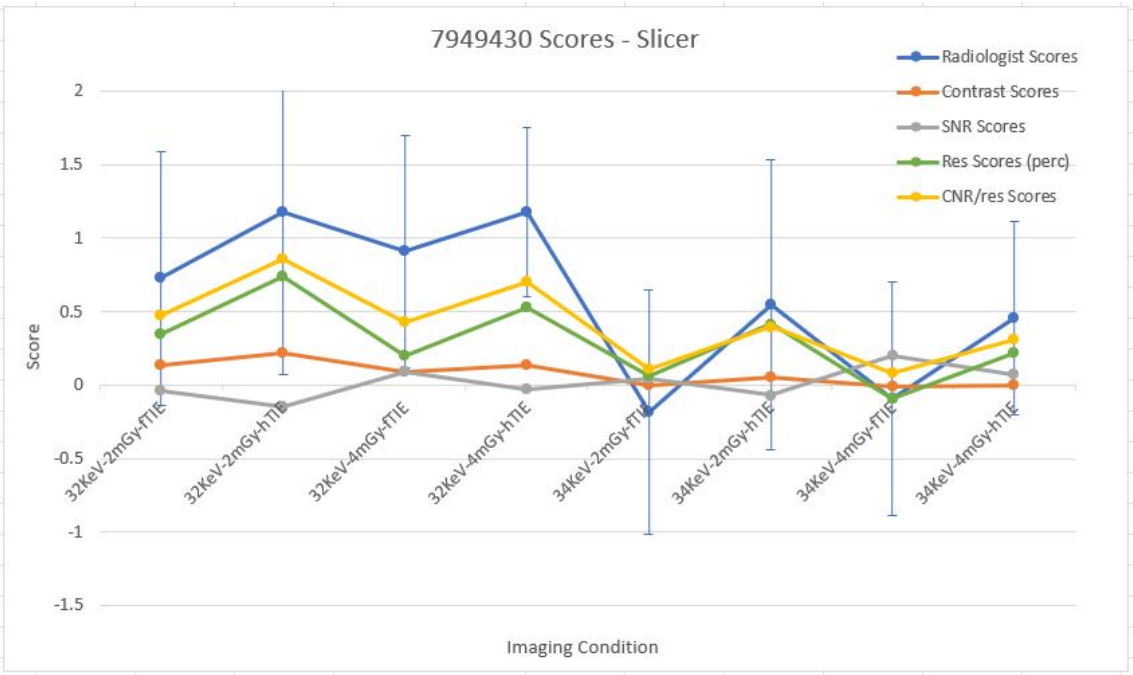


***Figure A.20:*** *Plot of subjective radiologist scores (in blue) for each imaging condition for sample 7949430 (shown in Table 3.3), with error bars of ± one standard deviation (shown in Table A.2). The subjective radiologist score is compared to various scaled quantitative scores measured using 3D Slicer including; CNR/res (yellow), contrast (red), SNR (grey) and spatial resolution (green) for sample 7949430.*

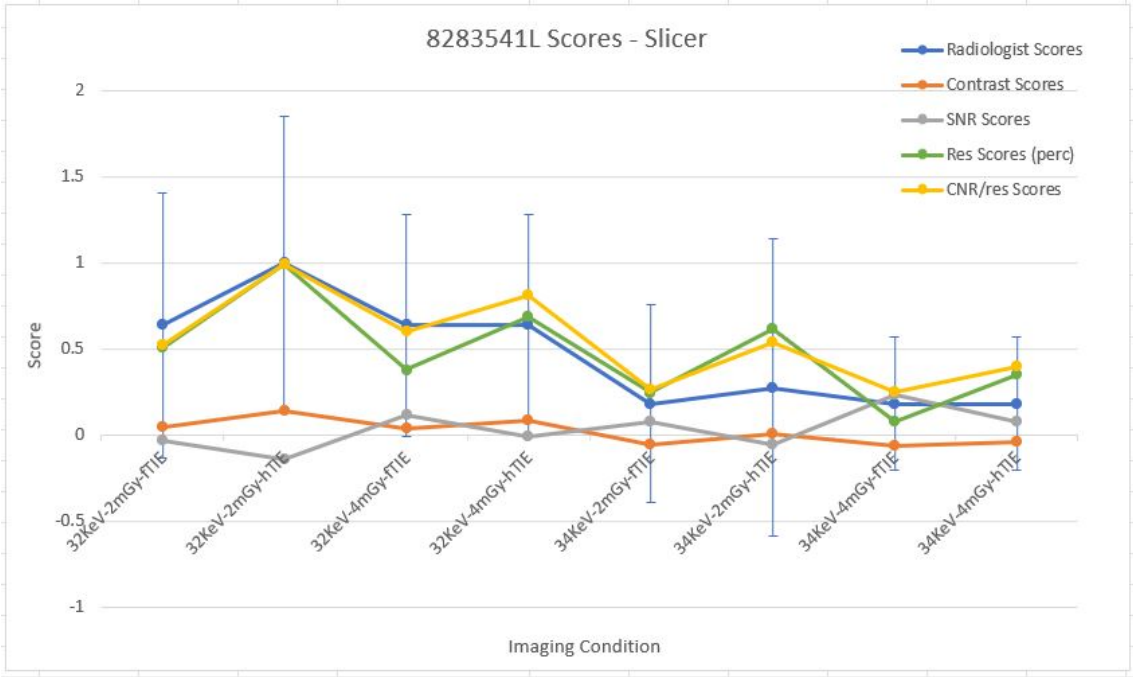


***Figure A.21:*** *Plot of subjective radiologist scores (in blue) for each imaging condition for sample 8283541L (shown in Table 3.3), with error bars of ± one standard deviation (shown in Table A.2). The subjective radiologist score is compared to various scaled quantitative scores measured using 3D Slicer including; CNR/res (yellow), contrast (red), SNR (grey) and spatial resolution (green) for sample 8283541L.*

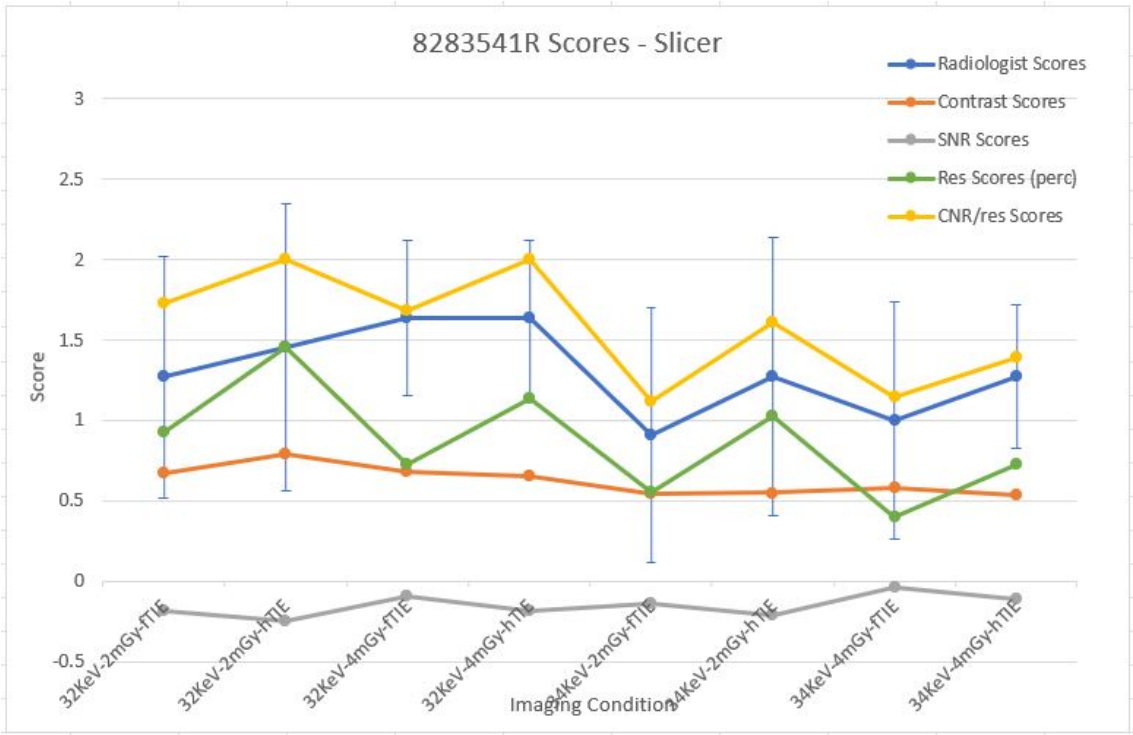


***Figure A.22:*** *Plot of subjective radiologist scores (in blue) for each imaging condition for sample 8283541R (shown in Table 3.3), with error bars of ± one standard deviation (shown in Table A.2). The subjective radiologist score is compared to various scaled quantitative scores measured using 3D Slicer including; CNR/res (yellow), contrast (red), SNR (grey) and spatial resolution (green) for sample 8283541R.*

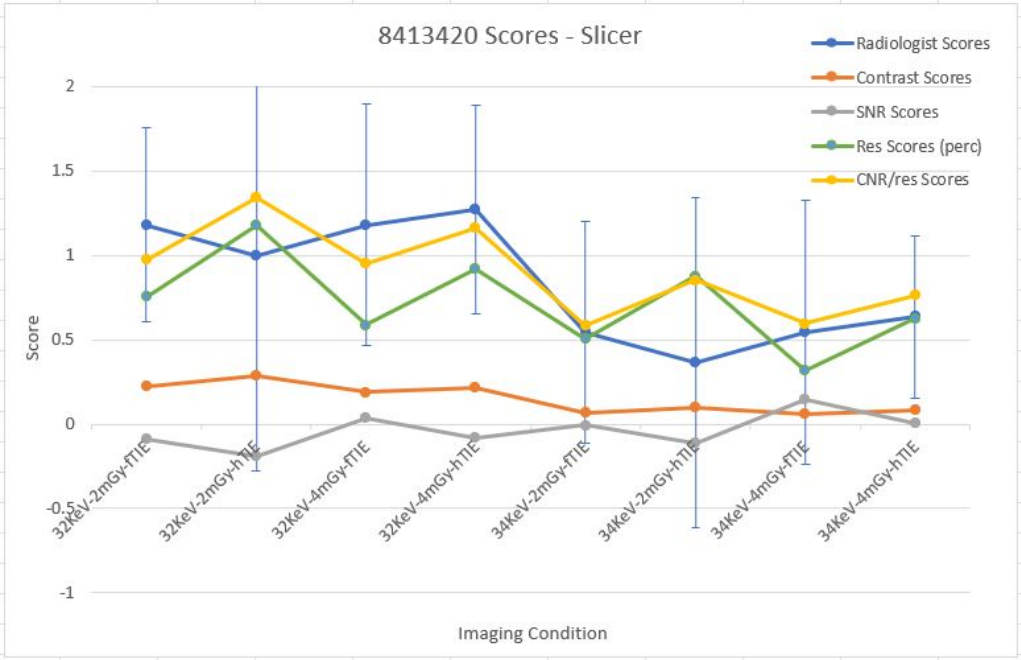


***Figure A.23:*** *Plot of subjective radiologist scores (in blue) for each imaging condition for sample 8413420 (shown in Table 3.3), with error bars of ± one standard deviation (shown in Table A.2). The subjective radiologist score is compared to various scaled quantitative scores measured using 3D Slicer including; CNR/res (yellow), contrast (red), SNR (grey) and spatial resolution (green) for sample 8413420.*

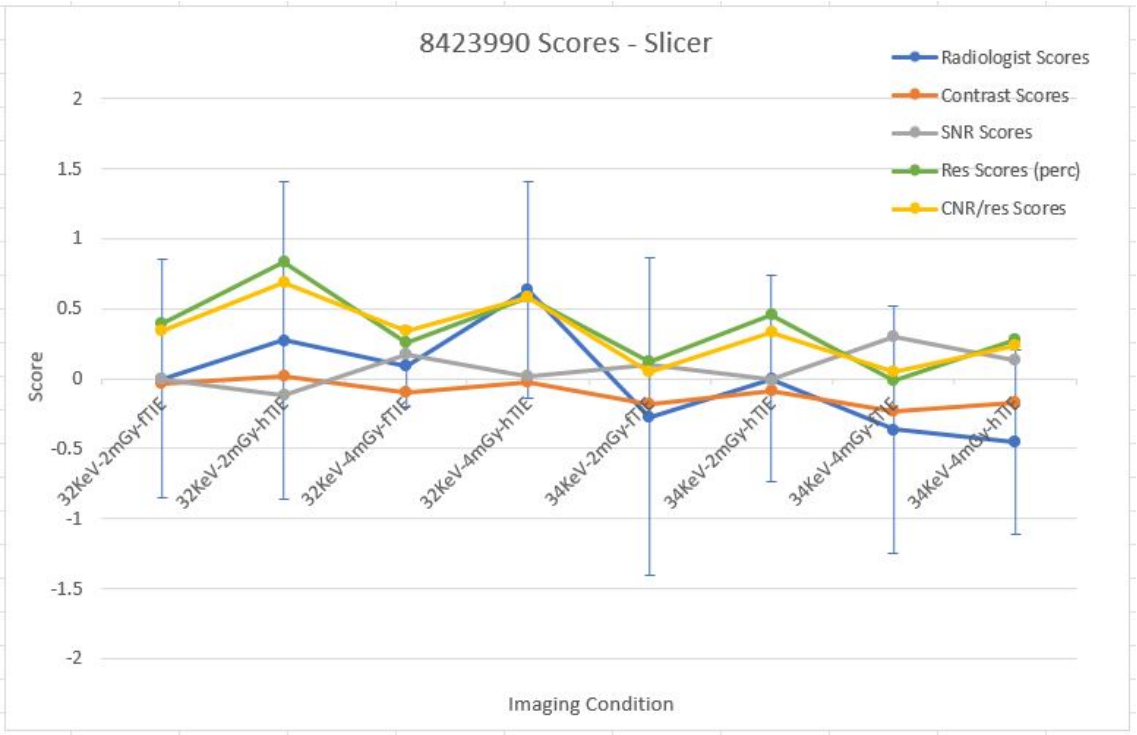


***Figure A.24:*** *Plot of subjective radiologist scores (in blue) for each imaging condition for sample 8423990 (shown in Table 3.3), with error bars of ± one standard deviation (shown in Table A.2). The subjective radiologist score is compared to various scaled quantitative scores measured using 3D Slicer including; CNR/res (yellow), contrast (red), SNR (grey) and spatial resolution (green) for sample 8423990.*

| Scaled CNR/res Scores - 3D Slicer | | | | | | |
|---|---|---|---|---|---|---|
| Imaging Condition | 2370691 | 4247239 | 4638975 | 4704628 | 7096050L | 709605R |
| 32KeV-2mGy-fTIE | 1.26 | 0.90 | 0.94 | 0.32 | 0.36 | 1.12 |
| 32KeV-2mGy-hTIE | 1.69 | 1.45 | 1.29 | 0.46 | 0.55 | 1.42 |
| 32KeV-4mGy-fTIE | 1.11 | 0.84 | 1.02 | 0.51 | 0.53 | 1.18 |
| 32KeV-4mGy-hTIE | 1.41 | 1.21 | 1.14 | 0.59 | 0.63 | 1.40 |
| 34KeV-2mGy-fTIE | 0.66 | 0.52 | 0.60 | 0.01 | 0.11 | 0.78 |
| 34KeV-2mGy-hTIE | 1.12 | 0.93 | 0.82 | 0.15 | 0.30 | 0.94 |
| 34KeV-4mGy-fTIE | 0.58 | 0.48 | 0.64 | 0.16 | 0.24 | 0.87 |
| 34KeV-4mGy-hTIE | 0.83 | 0.71 | 0.81 | 0.29 | 0.39 | 1.01 |

***Table A.10:*** *Scaled CNR/res scores measured using 3D Slicer for the first six samples. A green colored cell indicates that the scaled CNR/res score is within 1 standard deviation of the corresponding subjective radiologist score, while a yellow cell indicates that the scaled CNR/res score is outside 1 standard deviation.*

| Scaled CNR/res Scores - 3D Slicer | | | | | | |
|---|---|---|---|---|---|---|
| Imaging Condition | 7104092 | 7949430 | 8283541L | 8283541R | 8413420 | 8423990 |
| 32KeV-2mGy-fTIE | 1.07 | 0.48 | 0.52 | 1.73 | 0.97 | 0.34 |
| 32KeV-2mGy-hTIE | 1.65 | 0.85 | 0.99 | 2.00 | 1.35 | 0.68 |
| 32KeV-4mGy-fTIE | 1.10 | 0.43 | 0.60 | 1.68 | 0.95 | 0.34 |
| 32KeV-4mGy-hTIE | 1.32 | 0.70 | 0.81 | 2.00 | 1.16 | 0.59 |
| 34KeV-2mGy-fTIE | 0.54 | 0.11 | 0.26 | 1.12 | 0.59 | 0.05 |
| 34KeV-2mGy-hTIE | 0.92 | 0.40 | 0.54 | 1.61 | 0.85 | 0.33 |
| 34KeV-4mGy-fTIE | 0.55 | 0.08 | 0.25 | 1.15 | 0.59 | 0.04 |
| 34KeV-4mGy-hTIE | 0.82 | 0.31 | 0.40 | 1.39 | 0.77 | 0.23 |

***Table A.11:*** *Scaled CNR/res scores measured using 3D Slicer for the first six samples. A green colored cell indicates that the scaled CNR/res score is within 1 standard deviation of the corresponding subjective radiologist score, while a yellow cell indicates that the scaled CNR/res score is outside 1 standard deviation.*

# Appendix B

# Journal Article

At the time of writing, this article is under review. The article (pages 102-116) has been extracted from this version of the thesis due to possible copyright implications.

FULL PAPER
A Robust Computational Image Metric to Assist with Radiological Image Assessment
1Jesse M. Reynolds, B.E.(Hons), 2Patrick C. Brennan, PhD, 3,4Timur E. Gureyev, PhD and 1,4,5Konstantin M. Pavlov, PhD
1School of Physical and Chemical Sciences, University of Canterbury, Christchurch, 8041, New Zealand
2Faculty of Health Sciences, The University of Sydney, Lidcombe 2141, Australia
3School of Physics, The University of Melbourne, Parkville 3010, Australia
4School of Physics and Astronomy, Monash University, Clayton 3800, Australia
5School of Science and Technology, University of New England, Armidale 2351, Australia

# Appendix C

# 3D Slicer Code

## C.1 "Perceived" Spatial Resolution Code

The following code was used in the Python interactor in the 3D Slicer [117] software to calculate a FWHM of the LSF using the "perceived" spatial resolution method. The images were loaded into 3D Slicer using the DICOM module. The glandular tissue was then segmented as described in Section 2.3.2. The following code was then copy and pasted into the Python interactor window. The FWHM is read from the Python interactor window and recorded.

```
import numpy as np
import SegmentStatistics
import SimpleITK as sitk
import sitkUtils
from scipy import optimize
# Set voxel size in mm
voxelSize = 1
# How many pixels past the edge does the segment expand?
pixelsOut = 8
# How many pixels in from the edge does the segment shrink?
pixelsIn = 8
# Get current volume and segment node
volume = slicer.util.getNode('vtkMRMLScalarVolumeNode1')
segmentationNode = slicer.util.getNode('vtkMRMLSegmentationNode1')
# Compute global mean pixel values in the existing gladular and adipose segments
segStatLogic = SegmentStatistics.SegmentStatisticsLogic()
segStatLogic.getParameterNode().SetParameter("Segmentation", segmentationNode.GetID())
segStatLogic.getParameterNode().SetParameter("ScalarVolume", volume.GetID())
```

```
segStatLogic.getParameterNode().SetParameter("ScalarVolumeSegmentStatisticsPlugin.mean.enabled",str(True))
segStatLogic.getParameterNode().SetParameter("LabelmapSegmentStatisticsPlugin.enabled","True")
segStatLogic.getParameterNode().SetParameter("ScalarVolumeSegmentStatisticsPlugin.voxel_count.enabled","True")
segStatLogic.getParameterNode().SetParameter("ScalarVolumeSegmentStatisticsPlugin.volume_mm3.enabled","True")
#
segStatLogic.computeStatistics()
stats = segStatLogic.getStatistics()
#
originalSegments = stats["SegmentIDs"]
glandularMean = stats[originalSegments[0],"ScalarVolumeSegmentStatisticsPlugin.mean"]
adiposeMean = stats[originalSegments[1],"ScalarVolumeSegmentStatisticsPlugin.mean"]
# Get the number of slices in the volume
slices = volume.GetImageData().GetDimensions()[2]
# Set up numpy arrays for total mean values across the edges of every slice
# This will be converted to vtk arrays to be entered into a table.
numpyMeanValsTotal = np.zeros(shape=[pixelsIn + pixelsOut])
# Variable to keep track of any slices which are skipped due to full erosion of the segments
skippedSlices = 0
# Get volume as array
voxelArray = slicer.util.arrayFromVolume(volume)
# Loop through all the slices
for sliceIndex in range(slices):
  # Isolate a slice of the original volume as a new one-slice volume
  voxelSliceArray = voxelArray[sliceIndex]
  sliceImage = sitk.GetImageFromArray(voxelSliceArray)
  outputVolumeNode = slicer.mrmlScene.AddNewNodeByClass("vtkMRMLScalarVolumeNode", "SliceVolume")
  sitkUtils.PushVolumeToSlicer(sliceImage, outputVolumeNode)
  # Isolate a slice of the original segments as new segments
  newSegment = slicer.mrmlScene.AddNewNodeByClass("vtkMRMLSegmentationNode")
  #
  for segmentName in originalSegments:
```

```
50      labelmapVolumeNode =
        ↪ slicer.mrmlScene.AddNewNodeByClass("vtkMRMLLabelMapVolumeNode")
51      segmentIds = vtk.vtkStringArray()
52      segmentIds.InsertNextValue(segmentName)
53      #
54      slicer.vtkSlicerSegmentationsModuleLogic.ExportSegmentsToLabelmapNode
        ↪ (segmentationNode, segmentIds, labelmapVolumeNode,
        ↪ volume)
55      #
56      segmentArray = slicer.util.arrayFromVolume(labelmapVolumeNode)
57      segmentSliceArray = segmentArray[sliceIndex]
58      #
59      segmentSliceImage = sitk.GetImageFromArray(segmentSliceArray)
60      outputLabelmapVolumeNode =
        ↪ slicer.mrmlScene.AddNewNodeByClass("vtkMRMLLabelMapVolumeNode",
        ↪ segmentName)
61      sitkUtils.PushVolumeToSlicer(segmentSliceImage,
        ↪ outputLabelmapVolumeNode)
62      #
63      slicer.modules.segmentations.logic().ImportLabelmapToSegmentationNode
        ↪ (outputLabelmapVolumeNode,
        ↪ newSegment)
64      #
65      slicer.mrmlScene.RemoveNode(labelmapVolumeNode)
66      slicer.mrmlScene.RemoveNode(outputLabelmapVolumeNode)
67  #
68  # Setup segment statisitcs for new segment and volume
69  segStatLogic.getParameterNode().SetParameter("Segmentation",
    ↪ newSegment.GetID())
70  segStatLogic.getParameterNode().SetParameter("ScalarVolume",
    ↪ outputVolumeNode.GetID())
71  # Compute statisitcs to establish whether there is a segment present
72  segStatLogic.computeStatistics()
73  stats = segStatLogic.getStatistics()
74  segment = stats["SegmentIDs"]
75  if "Segment_1" not in segment:
76      print('No glandular segment present on this slice')
77      # The this slice will not contribute to total mean values
78      numpyMeanVals = np.zeros(shape=[pixelsOut + pixelsIn])
79      # Keep track of how many slices have been skipped
80      skippedSlices += 1
81  else:
```

```
82        # Setup temporary segment editor node to access effects
83        segmentEditorWidget = slicer.qMRMLSegmentEditorWidget()
84        segmentEditorWidget.setMRMLScene(slicer.mrmlScene)
85        segmentEditorNode =
          ↪  slicer.mrmlScene.AddNewNodeByClass("vtkMRMLSegmentEditorNode")
86        segmentEditorWidget.setMRMLSegmentEditorNode(segmentEditorNode)
87        segmentEditorWidget.setSegmentationNode(newSegment)
88        segmentEditorWidget.setMasterVolumeNode(outputVolumeNode)
89        # Expand margin of segment by a number of voxels (specified at top)
90        segmentEditorWidget.setActiveEffectByName("Margin")
91        effect = segmentEditorWidget.activeEffect()
92        effect.setParameter("MarginSizeMm", str(voxelSize*pixelsOut))
93        effect.self().onApply()
94        # Create first 1 pixel thick hollow segment
95        segmentEditorWidget.setActiveEffectByName("Hollow")
96        effect = segmentEditorWidget.activeEffect()
97        effect.setParameter("ShellMode", 'INSIDE_SURFACE')
98        effect.setParameter("ShellThicknessMm", str(voxelSize))
99        effect.self().onApply()
100       # Calculate mean of first pixel ring
101       segStatLogic.computeStatistics()
102       stats = segStatLogic.getStatistics()
103       segment = stats["SegmentIDs"]
104       mean = stats[segment[0],"ScalarVolumeSegmentStatisticsPlugin.mean"]
105       # Set up Numpy array to store mean values
106       numpyMeanVals = np.array([mean])
107       # Move ring in through a number of iterations across the edge
          ↪  (specified at top of code)
108       for i in range((pixelsOut + pixelsIn)-1):
109         # Undo hollow command to make segment solid again
110         segmentEditorWidget.undo()
111         # Shrink the segment by one pixel
112         segmentEditorWidget.setActiveEffectByName("Margin")
113         effect = segmentEditorWidget.activeEffect()
114         effect.setParameter("MarginSizeMm", str(-1*voxelSize))
115         effect.self().onApply()
116         # Make the segment hollow again
117         segmentEditorWidget.setActiveEffectByName("Hollow")
118         effect = segmentEditorWidget.activeEffect()
119         effect.setParameter("ShellMode", 'INSIDE_SURFACE')
120         effect.setParameter("ShellThicknessMm", str(voxelSize))
121         effect.self().onApply()
```

```
122         # Calculate mean value of current ring
123         segStatLogic.computeStatistics()
124         stats = segStatLogic.getStatistics()
125         segment = stats["SegmentIDs"]
126         # Calculate number of voxels in current ring.
127         # In slices with a small quantity of gladular tissue the segments
            ↪ can completely erode.
128         voxelNo = stats[segment[0],"LabelmapSegmentStatisticsPlugin.voxel
            ↪ _count"]
129         if voxelNo == 0:
130           print('No voxels left in glandular segment after ' + str(i -
              ↪ pixelsOut) + ' pixels inside edge on slice ' +
              ↪ str(sliceIndex))
131           # This slice will not contribute to total mean values
132           numpyMeanVals = np.zeros(shape=[pixelsOut + pixelsIn])
133           # Keep track of how many slices have been skipped
134           skippedSlices += 1
135           break
136         else:
137           mean =
              ↪ stats[segment[0],"ScalarVolumeSegmentStatisticsPlugin.mean"]
138           # Insert mean values in numpy arrays
139           numpyMeanVals = np.append(numpyMeanVals, mean)
140   # Add current value to running total
141   numpyMeanValsTotal += numpyMeanVals
142   # Clear temporary nodes used to isolate a slice
143   segmentEditorWidget = None
144   slicer.mrmlScene.RemoveNode(newSegment)
145   slicer.mrmlScene.RemoveNode(outputVolumeNode)
146   #
147
148
149 # Calculate mean edge values across all slices, taking into account
    ↪ skipped slices.
150 numpyMeanValsTotal /= (slices - skippedSlices)
151 # Create sequential pixel numbers to plot mean edge values against
152 numpyXVals = np.arange(pixelsIn + pixelsOut)
153 # Take derivative of edge spread function (ESF) to calculate point spread
    ↪ function (PSF)
154 dy = np.diff(numpyMeanValsTotal)
155 # Make offset x values to plot the PSF against
156 xpsf = np.linspace(0.5, len(dy)-0.5, len(dy))
```

```
157 # Set up Numpy array to store mean gladular values. These are put into an
    ↪  array to plot as a line with the ESF
158 numpyGlandularMeanVals = np.ones(shape=[(pixelsIn + pixelsOut)])
159 numpyGlandularMeanVals *= glandularMean
160 # Set up Numpy array to store mean adipose values. "
    ↪                                                 "
161 numpyAdiposeMeanVals = np.ones(shape=[(pixelsIn + pixelsOut)])
162 numpyAdiposeMeanVals *= adiposeMean
163 # Set up vtk array to store x values (number of pixel across the edge)
164 xVals = vtk.vtkIntArray()
165 xVals.SetName("Pixel Number")
166 # Set up other vtk arrays to put values into table
167 meanVals = vtk.vtkDoubleArray()
168 meanVals.SetName("Mean Pixel Value (MPV)")
169 #
170 gladularMeanVals = vtk.vtkDoubleArray()
171 gladularMeanVals.SetName("Glandular MPV")
172 #
173 adiposeMeanVals = vtk.vtkDoubleArray()
174 adiposeMeanVals.SetName("Adipose MPV")
175 #
176 psfvtk = vtk.vtkDoubleArray()
177 psfvtk.SetName("Point Spread Function")
178 #
179 xpsfvtk = vtk.vtkDoubleArray()
180 xpsfvtk.SetName("Pixel Number (PSF)")
181 # Convert numpy arrays to vtk arrays
182 for i in range((pixelsIn + pixelsOut)):
183   meanVals.InsertNextValue(numpyMeanValsTotal[i])
184   gladularMeanVals.InsertNextValue(numpyGlandularMeanVals[i])
185   adiposeMeanVals.InsertNextValue(numpyAdiposeMeanVals[i])
186   psfvtk.InsertNextValue(dy[i])
187   xpsfvtk.InsertNextValue(xpsf[i])
188   xVals.InsertNextValue(numpyXVals[i])
189
190
191 # Define Gaussian function to fit gaussian curve to edge gradient plot
192 def gaus(x,a,x0,sigma):
193     return a*np.exp(-(x-x0)**2/(2*sigma**2))
194
195
196 # Fit Gaussian curve to edge gradient plot
```

```
197 popt, _ = optimize.curve_fit(gaus, xpsf, dy)
198 # Create high resolution x array to plot the Gaussian curve against edge
    ↪ gradient
199 gausX = np.linspace(xpsf.min(), xpsf.max(), 100)
200 # Create Gaussian Curve Y values using Gaussian function
201 gausY = gaus(gausX, *popt)
202 # Create vtk arrays for plotting
203 gausXVTK = vtk.vtkDoubleArray()
204 gausXVTK.SetName('Gaussian x Values')
205 gausYVTK = vtk.vtkDoubleArray()
206 gausYVTK.SetName('Gaussian y Values')
207
208 # Convert numpy arrays to vtk arrays
209 for i in gausX:
210   gausXVTK.InsertNextValue(i)
211
212
213 for i in gausY:
214   gausYVTK.InsertNextValue(i)
215
216
217 # Create a table from result arrays
218 resultTableNode = slicer.mrmlScene.AddNewNodeByClass("vtkMRMLTableNode",
    ↪ "Edge Pixel Values")
219 resultTableNode.AddColumn(xVals)
220 resultTableNode.AddColumn(meanVals)
221 resultTableNode.AddColumn(gladularMeanVals)
222 resultTableNode.AddColumn(adiposeMeanVals)
223 # Create a table from result arrays
224 psfResultTableNode =
    ↪ slicer.mrmlScene.AddNewNodeByClass("vtkMRMLTableNode", "Point Spread
    ↪ Function (PSF)")
225 psfResultTableNode.AddColumn(xpsfvtk)
226 psfResultTableNode.AddColumn(psfvtk)
227 # Create a table for Gaussian fit curve
228 gausResultTableNode =
    ↪ slicer.mrmlScene.AddNewNodeByClass("vtkMRMLTableNode", "Point Spread
    ↪ Function (PSF)")
229 gausResultTableNode.AddColumn(gausXVTK)
230 gausResultTableNode.AddColumn(gausYVTK)
231 # Create plot series node edge means
```

```
232 plotSeriesNode1 =
    ↪ slicer.mrmlScene.AddNewNodeByClass("vtkMRMLPlotSeriesNode", "Pixel
    ↪ Values Plot")
233 plotSeriesNode1.SetAndObserveTableNodeID(resultTableNode.GetID())
234 plotSeriesNode1.SetXColumnName("Pixel Number")
235 plotSeriesNode1.SetYColumnName("Mean Pixel Value (MPV)")
236 plotSeriesNode1.SetPlotType(slicer.vtkMRMLPlotSeriesNode.PlotTypeLine)
237 plotSeriesNode1.SetUniqueColor()
238 # Create plot series node glandular means to plot as a line
239 plotSeriesNode2 =
    ↪ slicer.mrmlScene.AddNewNodeByClass("vtkMRMLPlotSeriesNode",
    ↪ "Glandular Plot")
240 plotSeriesNode2.SetAndObserveTableNodeID(resultTableNode.GetID())
241 plotSeriesNode2.SetXColumnName("Pixel Number")
242 plotSeriesNode2.SetYColumnName("Glandular MPV")
243 plotSeriesNode2.SetPlotType(slicer.vtkMRMLPlotSeriesNode.PlotTypeScatter)
244 plotSeriesNode2.SetUniqueColor()
245 # Create plot series node adipose means to plot as a line
246 plotSeriesNode3 =
    ↪ slicer.mrmlScene.AddNewNodeByClass("vtkMRMLPlotSeriesNode", "Adipose
    ↪ Plot")
247 plotSeriesNode3.SetAndObserveTableNodeID(resultTableNode.GetID())
248 plotSeriesNode3.SetXColumnName("Pixel Number")
249 plotSeriesNode3.SetYColumnName("Adipose MPV")
250 plotSeriesNode3.SetPlotType(slicer.vtkMRMLPlotSeriesNode.PlotTypeScatter)
251 plotSeriesNode3.SetUniqueColor()
252 # Create plot series PSF
253 plotSeriesNode4 =
    ↪ slicer.mrmlScene.AddNewNodeByClass("vtkMRMLPlotSeriesNode", "Point
    ↪ Spread Function")
254 plotSeriesNode4.SetAndObserveTableNodeID(psfResultTableNode.GetID())
255 plotSeriesNode4.SetXColumnName("Pixel Number (PSF)")
256 plotSeriesNode4.SetYColumnName("Point Spread Function")
257 plotSeriesNode4.SetPlotType(slicer.vtkMRMLPlotSeriesNode.PlotTypeScatter)
258 plotSeriesNode4.SetUniqueColor()
259 # Create plot series for Gaussian Curve
260 plotSeriesNode5 =
    ↪ slicer.mrmlScene.AddNewNodeByClass("vtkMRMLPlotSeriesNode", "Gaussian
    ↪ Fit")
261 plotSeriesNode5.SetAndObserveTableNodeID(gausResultTableNode.GetID())
262 plotSeriesNode5.SetXColumnName("Gaussian x Values")
263 plotSeriesNode5.SetYColumnName("Gaussian y Values")
```

```
plotSeriesNode5.SetPlotType(slicer.vtkMRMLPlotSeriesNode.PlotTypeScatter)
plotSeriesNode5.SetUniqueColor()
# Create plot chart node for edge profile
plotChartNode = slicer.mrmlScene.AddNewNodeByClass("vtkMRMLPlotChartNode")
plotChartNode.AddAndObservePlotSeriesNodeID(plotSeriesNode1.GetID())
plotChartNode.AddAndObservePlotSeriesNodeID(plotSeriesNode2.GetID())
plotChartNode.AddAndObservePlotSeriesNodeID(plotSeriesNode3.GetID())
plotChartNode.SetTitle('Edge Profile')
plotChartNode.SetXAxisTitle('Pixel Number')
plotChartNode.SetYAxisTitle('Mean Pixel Value')
# Create plot chart node
plotChartNode = slicer.mrmlScene.AddNewNodeByClass("vtkMRMLPlotChartNode")
plotChartNode.AddAndObservePlotSeriesNodeID(plotSeriesNode4.GetID())
plotChartNode.AddAndObservePlotSeriesNodeID(plotSeriesNode5.GetID())
plotChartNode.SetTitle('Edge Gradient')
plotChartNode.SetXAxisTitle('Pixel Number')
plotChartNode.SetYAxisTitle('Gradient')
# Switch to a layout that contains a plot view to create a plot widget
layoutManager = slicer.app.layoutManager()
layoutWithPlot =
↪  slicer.modules.plots.logic().GetLayoutWithPlot(layoutManager.layout)
layoutManager.setLayout(layoutWithPlot)
# Select chart in plot view
plotWidget = layoutManager.plotWidget(0)
plotViewNode = plotWidget.mrmlPlotViewNode()
plotViewNode.SetPlotChartNodeID(plotChartNode.GetID())
#
# Compute segment volumes
resultsTableNode = slicer.mrmlScene.AddNewNodeByClass('vtkMRMLTableNode')
segStatLogic = SegmentStatistics.SegmentStatisticsLogic()
segStatLogic.getParameterNode().SetParameter("Segmentation",
↪  segmentationNode.GetID())
segStatLogic.getParameterNode().SetParameter("ScalarVolume",
↪  volume.GetID())
segStatLogic.getParameterNode().SetParameter("LabelmapSegmentStatisticsPl
↪  ugin.enabled","False")
segStatLogic.getParameterNode().SetParameter("ScalarVolumeSegmentStatisti
↪  csPlugin.voxel_count.enabled","False")
segStatLogic.getParameterNode().SetParameter("ScalarVolumeSegmentStatisti
↪  csPlugin.volume_mm3.enabled","False")
segStatLogic.computeStatistics()
segStatLogic.exportToTable(resultsTableNode)
```

```
segStatLogic.showTable(resultsTableNode)
#
print(skippedSlices)
print("Full Width at Half Maximum = " + str(popt[2]*2.355))
#
```

## C.2 "Absolute" Spatial Resolution Code

The following code was used in the Python interactor in the 3D Slicer [117] software to calculate a FWHM of the LSF using the "absolute" spatial resolution method. The images were loaded into 3D Slicer using the DICOM module. The glandular and adipose tissue was painted as shown in Figure 2.3 and described in Section 2.3.2 under the "Contrast and Signal to Noise Ratio Calculation" heading. The following code was then copy and pasted into the Python interactor window. The FWHM is read from the Python interactor window and recorded.

```
import numpy as np
import SegmentStatistics
import SimpleITK as sitk
import sitkUtils
from scipy import optimize
# Set voxel size in mm
voxelSize = 1
# How many pixels past the edge does the segment expand/contract
pixelsOut = 4
# Counter used to iterate through slices for resolution measurement
resSliceNo = 0
# How many slices to skip through for resolution measurements
sliceSkip = 10
# Variable to keep track of any slices which are skipped due to full
↪  erosion of the segments
skippedSlices = 0
# Set max threshold value for glandular segment
thresholdMax = 255
# Set length (in number of pixels) to trim off bottom of volume
cropOffset = 37

# Get current volume
volumeNode = slicer.util.getNode('vtkMRMLScalarVolumeNode1')

# Create ROI around volume in order to trim the lower part of the volume
↪  which usually contains unwanted artefacts
```

```
roiNode = slicer.mrmlScene.AddNewNodeByClass("vtkMRMLAnnotationROINode")
# Use crop volume module functionality to fit ROI to volume
crop_module = slicer.vtkMRMLCropVolumeParametersNode()
slicer.mrmlScene.AddNode(crop_module)
crop_module.SetInputVolumeNodeID(volumeNode.GetID())
crop_module.SetOutputVolumeNodeID(volumeNode.GetID())
crop_module.SetROINodeID(roiNode.GetID())
crop_module.SetVoxelBased(1)
slicer.modules.cropvolume.logic().FitROIToInputVolume(crop_module)
# Move bottom of ROI up by the specified cropOffset to trim bottom of
↪ volume
xyz = [0,0,0]
radius = [0,0,0]
roiNode.GetXYZ(xyz)
roiNode.GetRadiusXYZ(radius)
xyz[1] = xyz[1] + (cropOffset/2)
radius[1] = radius[1] - (cropOffset/2)
roiNode.SetXYZ(xyz)
roiNode.SetRadiusXYZ(radius)

# Use crop volume module functionality to trim volume
crop_module.SetROINodeID(roiNode.GetID())
slicer.modules.cropvolume.logic().Apply(crop_module)
roiNode.SetDisplayVisibility(0)

# Calculate minimum threshold to segment glandular tissue from segment
↪ paint samples
sampleSegmentNode = slicer.util.getNode('vtkMRMLSegmentationNode1')
segStatLogic = SegmentStatistics.SegmentStatisticsLogic()
segStatLogic.getParameterNode().SetParameter("LabelmapSegmentStatisticsPl
↪ ugin.enabled","True")
segStatLogic.getParameterNode().SetParameter("ScalarVolumeSegmentStatisti
↪ csPlugin.voxel_count.enabled","True")
segStatLogic.getParameterNode().SetParameter("ScalarVolumeSegmentStatisti
↪ csPlugin.volume_mm3.enabled","True")
segStatLogic.getParameterNode().SetParameter("Segmentation",
↪ sampleSegmentNode.GetID())
segStatLogic.getParameterNode().SetParameter("ScalarVolume",
↪ volumeNode.GetID())
segStatLogic.computeStatistics()
stats = segStatLogic.getStatistics()
originalSegments = stats["SegmentIDs"]
```

```
sampleGlandularMean = stats[originalSegments[0],"ScalarVolumeSegmentStatisticsPlugin.mean"]
sampleAdiposeMean = stats[originalSegments[1],"ScalarVolumeSegmentStatisticsPlugin.mean"]
thresholdMin = (sampleGlandularMean + sampleAdiposeMean) / 2

# Get volume as array
voxelArray = slicer.util.arrayFromVolume(volumeNode)
# Get the number of slices in the volume
slices = volumeNode.GetImageData().GetDimensions()[2]
# This will be converted to vtk arrays to be entered into a table.
numpyMeanValsTotal = np.zeros(shape=[pixelsOut*2])

# First slice used is specifed by the sliceSkip variable
resSliceNo += sliceSkip
while resSliceNo < slices:
    # Isolate a slice of the original volume as a new one-slice volume
    voxelSliceArray = voxelArray[resSliceNo]
    sliceImage = sitk.GetImageFromArray(voxelSliceArray)
    outputVolumeNode = slicer.mrmlScene.AddNewNodeByClass("vtkMRMLScalarVolumeNode", "SliceVolume")
    sitkUtils.PushVolumeToSlicer(sliceImage, outputVolumeNode)
    # Create a new segment node for the isolated slice
    newSegment = slicer.mrmlScene.AddNewNodeByClass("vtkMRMLSegmentationNode")
    newSegment.CreateDefaultDisplayNodes() # only needed for display
    newSegment.SetReferenceImageGeometryParameterFromVolumeNode(outputVolumeNode)
    # Setup temporary segment editor node to access effects
    segmentEditorWidget = slicer.qMRMLSegmentEditorWidget()
    segmentEditorWidget.setMRMLScene(slicer.mrmlScene)
    segmentEditorNode = slicer.mrmlScene.AddNewNodeByClass("vtkMRMLSegmentEditorNode")
    segmentEditorWidget.setMRMLSegmentEditorNode(segmentEditorNode)
    segmentEditorWidget.setSegmentationNode(newSegment)
    segmentEditorWidget.setMasterVolumeNode(outputVolumeNode)
    # Create segments
    sliceAddedSegmentID = newSegment.GetSegmentation().AddEmptySegment()
    segmentEditorNode.SetSelectedSegmentID(sliceAddedSegmentID)
    # Fill by thresholding
    segmentEditorWidget.setActiveEffectByName("Threshold")
```

```
95      effect = segmentEditorWidget.activeEffect()
96      effect.setParameter("MinimumThreshold",str(thresholdMin))
97      effect.setParameter("MaximumThreshold",str(thresholdMax))
98      effect.self().onApply()
99      # Remove Small Islands
100     segmentEditorWidget.setActiveEffectByName("Islands")
101     effect = segmentEditorWidget.activeEffect()
102     effect.setParameter("Operation","REMOVE_SMALL_ISLANDS")
103     effect.setParameter("MinimumSize","10")
104     effect.self().onApply()
105     # Close Small Holes
106     segmentEditorWidget.setActiveEffectByName("Smoothing")
107     effect = segmentEditorWidget.activeEffect()
108     effect.setParameter("SmoothingMethod","MORPHOLOGICAL_CLOSING")
109     effect.setParameter("KernelSizeMm","2")
110     effect.self().onApply()
111     # Setup segment statisitcs for new segment and volume
112     segStatLogic.getParameterNode().SetParameter("Segmentation",
        ↪  newSegment.GetID())
113     segStatLogic.getParameterNode().SetParameter("ScalarVolume",
        ↪  outputVolumeNode.GetID())
114     # Compute statisitcs to establish whether there is a segment present
115     segStatLogic.computeStatistics()
116     stats = segStatLogic.getStatistics()
117     segment = stats["SegmentIDs"]
118     if "Segment_1" not in segment:
119       print('No glandular segment present on this slice')
120     else:
121       # Used to keep track of which iteration the loop is up to
122       itrCount = pixelsOut - 1
123       for i in range(pixelsOut*2):
124         # Expand margin of segment by a number of voxels (specified at
          ↪  top)
125         segmentEditorWidget.setActiveEffectByName("Margin")
126         effect = segmentEditorWidget.activeEffect()
127         effect.setParameter("MarginSizeMm", str(voxelSize*itrCount))
128         effect.self().onApply()
129         # Create first 1 pixel thick hollow segment
130         segmentEditorWidget.setActiveEffectByName("Hollow")
131         effect = segmentEditorWidget.activeEffect()
132         effect.setParameter("ShellMode", 'INSIDE_SURFACE')
133         effect.setParameter("ShellThicknessMm", str(voxelSize))
```

```
134         effect.self().onApply()
135         # Calculate mean of first pixel ring
136         segStatLogic.computeStatistics()
137         stats = segStatLogic.getStatistics()
138         segment = stats["SegmentIDs"]
139         mean =
            ↪  stats[segment[0],"ScalarVolumeSegmentStatisticsPlugin.mean"]
140         # Calculate number of voxels in current ring.
141         # In slices with a small quantity of gladular tissue the segments
            ↪  can completely erode.
142         voxelNo = stats[segment[0],"LabelmapSegmentStatisticsPlugin.voxel
            ↪  _count"]
143         # Set up Numpy array to store mean values
144         if voxelNo == 0:
145           print('No voxels left in glandular segment after ' + str(i -
              ↪  pixelsOut) + ' pixels inside edge on slice ' +
              ↪  str(sliceIndex))
146           # This slice will not contribute to total mean values
147           numpyMeanVals = np.zeros(shape=[pixelsOut*2])
148           # Keep track of how many slices have been skipped
149           skippedSlices += 1
150           break
151         elif itrCount == pixelsOut - 1:
152           # Create numpy array to store mean pixel values
153           numpyMeanVals = np.array([mean])
154         else:
155           # Insert mean values in numpy array
156           numpyMeanVals = np.append(numpyMeanVals, mean)
157         # Undo operation twice to return segment to original form
158         segmentEditorWidget.undo()
159         segmentEditorWidget.undo()
160         itrCount -= 1
161       # Add current value to running total
162       numpyMeanValsTotal += numpyMeanVals
163       # Clear temporary nodes used to isolate a slice
164       slicer.mrmlScene.RemoveNode(newSegment)
165       slicer.mrmlScene.RemoveNode(outputVolumeNode)
166       # Update slice number counter
167       resSliceNo += sliceSkip
168
169
170   # Clear temporary nodes used to isolate a slice
```

```
segmentEditorWidget = None
slicer.mrmlScene.RemoveNode(segmentEditorNode)

# Calculate mean edge values across all slices, taking into account
↪  skipped slices.
numpyMeanValsTotal /= ((resSliceNo/sliceSkip) - skippedSlices)
# Create sequential pixel numbers to plot mean edge values against
numpyXVals = np.arange(pixelsOut*2)
# Take derivative of edge spread function (ESF) to calculate point spread
↪  function (PSF)
dy = np.diff(numpyMeanValsTotal)
# Make offset x values to plot the PSF against
xpsf = np.linspace(0.5, len(dy)-0.5, len(dy))
# Set up Numpy array to store mean gladular values. These are put into an
↪  array to plot as a line with the ESF
numpyGlandularMeanVals = np.ones(shape=[(pixelsOut*2)])
numpyGlandularMeanVals *= sampleGlandularMean
# Set up Numpy array to store mean adipose values. "
↪                                                 "
numpyAdiposeMeanVals = np.ones(shape=[(pixelsOut*2)])
numpyAdiposeMeanVals *= sampleAdiposeMean
# Set up vtk array to store x values (number of pixel across the edge)
xVals = vtk.vtkIntArray()
xVals.SetName("Pixel Number")
# Set up other vtk arrays to put values into table
meanVals = vtk.vtkDoubleArray()
meanVals.SetName("Mean Pixel Value (MPV)")
#
gladularMeanVals = vtk.vtkDoubleArray()
gladularMeanVals.SetName("Glandular MPV")
#
adiposeMeanVals = vtk.vtkDoubleArray()
adiposeMeanVals.SetName("Adipose MPV")
#
psfvtk = vtk.vtkDoubleArray()
psfvtk.SetName("Point Spread Function")
#
xpsfvtk = vtk.vtkDoubleArray()
xpsfvtk.SetName("Pixel Number (PSF)")
# Convert numpy arrays to vtk arrays
for i in range((pixelsOut*2)-1):
  meanVals.InsertNextValue(numpyMeanValsTotal[i])
```

```
209   gladularMeanVals.InsertNextValue(numpyGlandularMeanVals[i])
210   adiposeMeanVals.InsertNextValue(numpyAdiposeMeanVals[i])
211   psfvtk.InsertNextValue(dy[i])
212   xpsfvtk.InsertNextValue(xpsf[i])
213   xVals.InsertNextValue(numpyXVals[i])
214
215
216 # Define Gaussian function to fit gaussian curve to edge gradient plot
217 def gaus(x,a,x0,sigma):
218     return a*np.exp(-(x-x0)**2/(2*sigma**2))
219
220
221 # Fit Gaussian curve to edge gradient plot
222 popt, _ = optimize.curve_fit(gaus, xpsf[pixelsOut-2:pixelsOut+1],
    ↪  dy[pixelsOut-2:pixelsOut+1])
223 # Create high resolution x array to plot the Gaussian curve against edge
    ↪  gradient
224 gausX = np.linspace(xpsf.min(), xpsf.max(), 100)
225 # Create Gaussian Curve Y values using Gaussian function
226 gausY = gaus(gausX, *popt)
227 # Create vtk arrays for plotting
228 gausXVTK = vtk.vtkDoubleArray()
229 gausXVTK.SetName('Gaussian x Values')
230 gausYVTK = vtk.vtkDoubleArray()
231 gausYVTK.SetName('Gaussian y Values')
232
233 # Convert numpy arrays to vtk arrays
234 for i in gausX:
235   gausXVTK.InsertNextValue(i)
236
237
238 for i in gausY:
239   gausYVTK.InsertNextValue(i)
240
241
242 # Create a table from result arrays
243 resultTableNode = slicer.mrmlScene.AddNewNodeByClass("vtkMRMLTableNode",
    ↪  "Edge Pixel Values")
244 resultTableNode.AddColumn(xVals)
245 resultTableNode.AddColumn(meanVals)
246 resultTableNode.AddColumn(gladularMeanVals)
247 resultTableNode.AddColumn(adiposeMeanVals)
```

```
248 # Create a table from result arrays
249 psfResultTableNode =
    ↪ slicer.mrmlScene.AddNewNodeByClass("vtkMRMLTableNode", "Point Spread
    ↪ Function (PSF)")
250 psfResultTableNode.AddColumn(xpsfvtk)
251 psfResultTableNode.AddColumn(psfvtk)
252 # Create a table for Gaussian fit curve
253 gausResultTableNode =
    ↪ slicer.mrmlScene.AddNewNodeByClass("vtkMRMLTableNode", "Point Spread
    ↪ Function (PSF)")
254 gausResultTableNode.AddColumn(gausXVTK)
255 gausResultTableNode.AddColumn(gausYVTK)
256 # Create plot series node edge means
257 plotSeriesNode1 =
    ↪ slicer.mrmlScene.AddNewNodeByClass("vtkMRMLPlotSeriesNode", "Pixel
    ↪ Values Plot")
258 plotSeriesNode1.SetAndObserveTableNodeID(resultTableNode.GetID())
259 plotSeriesNode1.SetXColumnName("Pixel Number")
260 plotSeriesNode1.SetYColumnName("Mean Pixel Value (MPV)")
261 plotSeriesNode1.SetPlotType(slicer.vtkMRMLPlotSeriesNode.PlotTypeLine)
262 plotSeriesNode1.SetUniqueColor()
263 # Create plot series node glandular means to plot as a line
264 plotSeriesNode2 =
    ↪ slicer.mrmlScene.AddNewNodeByClass("vtkMRMLPlotSeriesNode",
    ↪ "Glandular Plot")
265 plotSeriesNode2.SetAndObserveTableNodeID(resultTableNode.GetID())
266 plotSeriesNode2.SetXColumnName("Pixel Number")
267 plotSeriesNode2.SetYColumnName("Glandular MPV")
268 plotSeriesNode2.SetPlotType(slicer.vtkMRMLPlotSeriesNode.PlotTypeScatter)
269 plotSeriesNode2.SetUniqueColor()
270 # Create plot series node adipose means to plot as a line
271 plotSeriesNode3 =
    ↪ slicer.mrmlScene.AddNewNodeByClass("vtkMRMLPlotSeriesNode", "Adipose
    ↪ Plot")
272 plotSeriesNode3.SetAndObserveTableNodeID(resultTableNode.GetID())
273 plotSeriesNode3.SetXColumnName("Pixel Number")
274 plotSeriesNode3.SetYColumnName("Adipose MPV")
275 plotSeriesNode3.SetPlotType(slicer.vtkMRMLPlotSeriesNode.PlotTypeScatter)
276 plotSeriesNode3.SetUniqueColor()
277 # Create plot series PSF
```

```
278 plotSeriesNode4 =
    ↪ slicer.mrmlScene.AddNewNodeByClass("vtkMRMLPlotSeriesNode", "Point
    ↪ Spread Function")
279 plotSeriesNode4.SetAndObserveTableNodeID(psfResultTableNode.GetID())
280 plotSeriesNode4.SetXColumnName("Pixel Number (PSF)")
281 plotSeriesNode4.SetYColumnName("Point Spread Function")
282 plotSeriesNode4.SetPlotType(slicer.vtkMRMLPlotSeriesNode.PlotTypeScatter)
283 plotSeriesNode4.SetUniqueColor()
284 # Create plot series for Gaussian Curve
285 plotSeriesNode5 =
    ↪ slicer.mrmlScene.AddNewNodeByClass("vtkMRMLPlotSeriesNode", "Gaussian
    ↪ Fit")
286 plotSeriesNode5.SetAndObserveTableNodeID(gausResultTableNode.GetID())
287 plotSeriesNode5.SetXColumnName("Gaussian x Values")
288 plotSeriesNode5.SetYColumnName("Gaussian y Values")
289 plotSeriesNode5.SetPlotType(slicer.vtkMRMLPlotSeriesNode.PlotTypeScatter)
290 plotSeriesNode5.SetUniqueColor()
291 # Create plot chart node for edge profile
292 plotChartNode = slicer.mrmlScene.AddNewNodeByClass("vtkMRMLPlotChartNode")
293 plotChartNode.AddAndObservePlotSeriesNodeID(plotSeriesNode1.GetID())
294 plotChartNode.AddAndObservePlotSeriesNodeID(plotSeriesNode2.GetID())
295 plotChartNode.AddAndObservePlotSeriesNodeID(plotSeriesNode3.GetID())
296 plotChartNode.SetTitle('Edge Profile')
297 plotChartNode.SetXAxisTitle('Pixel Number')
298 plotChartNode.SetYAxisTitle('Mean Pixel Value')
299 # Create plot chart node
300 plotChartNode = slicer.mrmlScene.AddNewNodeByClass("vtkMRMLPlotChartNode")
301 plotChartNode.AddAndObservePlotSeriesNodeID(plotSeriesNode4.GetID())
302 plotChartNode.AddAndObservePlotSeriesNodeID(plotSeriesNode5.GetID())
303 plotChartNode.SetTitle('Edge Gradient')
304 plotChartNode.SetXAxisTitle('Pixel Number')
305 plotChartNode.SetYAxisTitle('Gradient')
306 # Switch to a layout that contains a plot view to create a plot widget
307 layoutManager = slicer.app.layoutManager()
308 layoutWithPlot =
    ↪ slicer.modules.plots.logic().GetLayoutWithPlot(layoutManager.layout)
309 layoutManager.setLayout(layoutWithPlot)
310 # Select chart in plot view
311 plotWidget = layoutManager.plotWidget(0)
312 plotViewNode = plotWidget.mrmlPlotViewNode()
313 plotViewNode.SetPlotChartNodeID(plotChartNode.GetID())
314 #
```

```
315 # Compute segment volumes
316 resultsTableNode = slicer.mrmlScene.AddNewNodeByClass('vtkMRMLTableNode')
317 segStatLogic.getParameterNode().SetParameter("Segmentation",
    ↪ sampleSegmentNode.GetID())
318 segStatLogic.getParameterNode().SetParameter("ScalarVolume",
    ↪ volumeNode.GetID())
319 segStatLogic.getParameterNode().SetParameter("LabelmapSegmentStatisticsPl
    ↪ ugin.enabled","False")
320 segStatLogic.getParameterNode().SetParameter("ScalarVolumeSegmentStatisti
    ↪ csPlugin.voxel_count.enabled","False")
321 segStatLogic.getParameterNode().SetParameter("ScalarVolumeSegmentStatisti
    ↪ csPlugin.volume_mm3.enabled","False")
322 segStatLogic.computeStatistics()
323 segStatLogic.exportToTable(resultsTableNode)
324 segStatLogic.showTable(resultsTableNode)
325 #
326 print("Minimum Threshold Used for Glandular Segment = " +
    ↪ str(thresholdMin))
327 print("Full Width at Half Maximum = " + str(popt[2]*2.355))
328 #
```

# References


[1] Breast Cancer Foundation New Zealand; 2021. Accessed: 05/03/2021. https://www.breastcancerfoundation.org.nz/breast-cancer/types-of-breast-cancer/pre-invasive.

[2] Southern Cross Medical Library; 2021. Accessed: 05/03/2021. https://www.southerncross.co.nz/group/medical-library/breast-cancer-symptoms-diagnosis-treatment.

[3] Tortora G, Grabowksi S. Principles of anatomy and physiology, ed 12. Wiley; 2010.

[4] Centre for Disease Control and Prevention; 2021. Accessed: 07/03/2021. https://www.cdc.gov/cancer/breast/basic_info/treatment.htm.

[5] Sung H, Ferlay J, Siegel RL, Laversanne M, Soerjomataram I, Jemal A, et al. Global cancer statistics 2020: GLOBOCAN estimates of incidence and mortality worldwide for 36 cancers in 185 countries. CA: A Cancer Journal for Clinicians. 2021.

[6] Walters S, Maringe C, Butler J, Rachet B, Barrett-Lee P, Bergh J, et al. Breast cancer survival and stage at diagnosis in Australia, Canada, Denmark, Norway, Sweden and the UK, 2000-2007: a population-based study. British Journal of Cancer. 2013;108(5):1195–1208.

[7] Mandelblatt J, Van Ravesteyn N, Schechter C, Chang Y, Huang AT, Near AM, et al. Which strategies reduce breast cancer mortality most? Collaborative modeling of optimal screening, treatment, and obesity prevention. Cancer. 2013;119(14):2541–2548.

[8] Centre for Disease Control and Prevention; 2021. Accessed: 07/03/2021. https://www.cdc.gov/cancer/breast/basic_info/screening.htm.

[9] Shapiro S, Coleman EA, Broeders M, Codd M, de Koning H, Fracheboud J, et al. Breast cancer screening programmes in 22 countries: current policies, administration and guidelines. International Journal of Epidemiology. 1998;27(5):735–742.

[10] Breast Screen Aotearoa; 2021. Accessed: 08/03/2021. https://www.timetoscreen.nz/breast-screening/having-a-mammogram/about-the-programme/.

[11] IARC. Breast Cancer Screening. IARC Handbooks of Cancer Prevention. World Health Organization; 2016.

[12] Dance D, Christofides S, Maidment A. Diagnostic radiology physics: a handbook for teachers and students. Vienna: International Atomic Energy Agency (IAEA); 2014.

[13] ICRP. The 2007 Recommendations of the International Commission on Radiological Protection. ICRP Publication 103. Annals of the ICRP 37 (2-4). 2007.

[14] Young K, Wallis M, Ramsdale M. Mammographic film density and detection of small breast cancers. Clinical Radiology. 1994;49(7):461–465.

[15] Bushberg J, Seibert A, Leidholdt E, Boone J. The essential physics of medical imaging; 3rd ed. Lippincott Williams and Wilkins; 2012.

[16] Whelehan P, Evans A, Wells M, MacGillivray S. The effect of mammography pain on repeat participation in breast cancer screening: a systematic review. The Breast. 2013;22(4):389–394.

[17] Fischmann A, Siegmann K, Wersebe A, Claussen C, Muller-Schimpfle M. Comparison of full-field digital mammography and film–screen mammography: image quality and lesion detection. The British Journal of Radiology. 2005;78(928):312–315.

[18] Smith A. Fundamentals of digital mammography: physics, technology and practical considerations. Radiology management. 2003;25(5):18—24, 26—31.

[19] Hendrick R, Pisano E, Averbukh A, Moran C, Berns E, Yaffe M, et al. Comparison of acquisition parameters and breast dose in digital mammography and screen-film mammography in the American College of Radiology Imaging Network digital mammographic imaging screening trial. American Journal of Roentgenology. 2010;194(2):362–369.

[20] Yaffe M, Bloomquist A, Hunter D, Mawdsley G, Chiarelli A, Muradali D, et al. Comparative performance of modern digital mammography systems in a large breast screening program. Medical Physics. 2013;40(12):121915.

[21] Chiarelli A, Edwards S, Prummel M, Muradali D, Majpruz V, Done S, et al. Digital compared with screen-film mammography: performance measures in concurrent cohorts within an organized breast screening program. Radiology. 2013;268(3):684–693.

[22] BreastScreen Aotearoa Now Fully Digital; 2021. Accessed: 19/03/2021. https://www.nsu.govt.nz/news/screening-matters-issue-44-february-2014/breastscreen-aotearoa-now-fully-digital.

[23] Bluekens AM, Holland R, Karssemeijer N, Broeders M, den Heeten G. Comparison of digital screening mammography and screen-film mammography in the early detection of clinically relevant cancers: a multicenter study. Radiology. 2012;265(3):707–714.

[24] Pisano E, Yaffe M. Digital mammography. Radiology. 2005;234(2):353–362.

[25] Fischer U, Baum F, Obenauer S, Luftner-Nagel S, Von Heyden D, Vosshenrich R, et al. Comparative study in patients with microcalcifications: full-field digital mammography vs screen-film mammography. European radiology. 2002;12(11):2679–2683.

[26] Hambly N, McNicholas M, Phelan N, Hargaden G, O'Doherty A, Flanagan F. Comparison of digital mammography and screen-film mammography in breast cancer screening: a review in the Irish breast screening program. American Journal of Roentgenology. 2009;193(4):1010–1018.

[27] Jin J. Breast cancer screening: benefits and harms. JAMA. 2014;312(23):2585–2585.

[28] Pace L, Keating N. A systematic assessment of benefits and risks to guide breast cancer screening decisions. JAMA. 2014;311(13):1327–1335.

[29] Gennaro G, Bernardi D, Houssami N. Radiation dose with digital breast tomosynthesis compared to digital mammography: per-view analysis. European Radiology. 2018;28(2):573–581.

[30] Sankatsing V, van Ravesteyn N, Juraniec K. Cost-effectiveness of digital breast tomosynthesis in the Dutch breast cancer screening program: a probabilistic sensitivity analysis. Quantifying and Improving Outcomes of Breast Cancer Screening. 2021:161.

[31] Brem R, Lenihan M, Lieberman J, Torrente J. Screening breast ultrasound: past, present, and future. American Journal of Roentgenology. 2015;204(2):234–240.

[32] Smith J, Andreopoulou E. An overview of the status of imaging screening technology for breast cancer. Annals of Oncology. 2004;15:i18–i26.

[33] NSU. Position statement addressing the use of ultrasound as a breast cancer screening tool; 2014. Accessed: 28/03/2021. https://www.nsu.govt.nz/system/files/page/position-statement-addressing-the-use-of-ultrasound-as-a-breast-cancer-tool.pdf.

[34] ASBS. Consensus Guideline on Diagnostic and Screening Magnetic Resonance Imaging of the Breast; 2014. Accessed: 31/03/2021. https://www.breastsurgeons.org/docs/statements/Consensus-Guideline-on-Diagnostic-and-Screening-Magnetic-Resonance-Imaging-of-the-Breast.pdf.

[35] ACS. American Cancer Society Recommendations for the Early Detection of Breast Cancer; 2020. Accessed: 31/03/2021. https://www.cancer.org/cancer/breast-cancer/screening-tests-and-early-detection/american-cancer-society-recommendations-for-the-early-detection-of-breast-cancer.html.

[36] Warner E, Messersmith H, Causer P, Eisen A, Shumak R, Plewes D. Systematic review: using magnetic resonance imaging to screen women at high risk for breast cancer. Annals of Internal Medicine. 2008;148(9):671–679.

[37] Phi XA, Houssami N, Obdeijn IM, Warner E, Sardanelli F, Leach M, et al. Magnetic Resonance Imaging Improves Breast Screening Sensitivity in BRCA Mutation Carriers Age>= 50 Years: Evidence From an Individual Patient Data Meta-Analysis. Journal of clinical oncology: official journal of the American Society of Clinical Oncology. 2015;33(4):349–356.

[38] NBCTSWG. Standards of Service Provision for Breast Cancer Patients in New Zealand - Provisional. Wellington: Ministry of Health; 2013. Available from: https://cancerhub.net/index.php/standards-of-service-provision-for-breast-cancer-patients-in-new-zealand-provisional/.

[39] Boone J, Kwan A, Yang K, Burkett G, Lindfors K, Nelson T. Computed tomography for imaging the breast. Journal of Mammary Gland Biology and Neoplasia. 2006;11(2):103–111.

[40] Sarno A, Mettivier G, Russo P. Dedicated breast computed tomography: basic aspects. Medical Physics. 2015;42(6 Part 1):2786–2804.

[41] Vreugdenburg T, Willis C, Mundy L, Hiller J. A systematic review of elastography, electrical impedance scanning, and digital infrared thermography for breast cancer screening and diagnosis. Breast Cancer Research and Treatment. 2013;137(3):665–676.

[42] NSU. Position statement: The use of thermography as a breast cancer screening or diagnostic tool; 2010. Accessed: 01/04/2021. https://www.nsu.govt.nz/system/files/page/thermography_position_statement_june16.pdf.

[43] Hendrick R. Radiation doses and cancer risks from breast imaging studies. Radiology. 2010;257(1):246–253.

[44] Berg WA, Weinberg IN, Narayanan D, Lobrano ME, Ross E, Amodei L, et al. High-resolution fluorodeoxyglucose positron emission tomography with compression ("positron emission mammography") is highly accurate in depicting primary breast cancer. The Breast. 2006;12(4):309–323.

[45] Barton MB, Harris R, Fletcher SW. Does this patient have breast cancer?: The screening clinical breast examination: should it be done? How? JAMA. 1999;282(13):1270–1280.

[46] Röntgen WC. Ueber eine neue Art von Strahlen. Gesellschaft; 1895.

[47] Serway R, Jewett J. Physics for Scientists and Engineers 6th edition. Thomson Brookes/Cole; 2004.

[48] Paganin D. Coherent X-ray optics. Oxford University Press; 2006.

[49] How does the Australian Synchrotron Work?; 2021. Accessed: 06/04/2021. http://archive.synchrotron.org.au/about-us/our-facilities/accelerator-physics/how-does-the-australian-synchrotron-work.

[50] Gureyev T, Nesterets YI, Baran P, Taba S, Mayo S, Thompson D, et al. Propagation-based x-ray phase-contrast tomography of mastectomy samples using synchrotron radiation. Medical Physics. 2019;46(12):5478–5487.

[51] Hausermann D, Hall C, Maksimenko A, Campbell C. The imaging and medical beam line at the Australian Synchrotron. In: AIP Conference Proceedings. vol. 1266. American Institute of Physics; 2010. p. 3–9.

[52] Gureyev T, Baran P, Pacile S, Nesterets Y, Mayo S, Dimmock M, et al. Synchrotron-Based X-ray Phase-Contrast Tomography for Breast Cancer Imaging. Microscopy and Microanalysis. 2018;24(S2):144–145.

[53] Van der Veen F, Pfeiffer F. Coherent x-ray scattering. Journal of Physics: Condensed Matter. 2004;16(28):5003.

[54] Bravin A, Coan P, Suortti P. X-ray phase-contrast imaging: from pre-clinical applications towards clinics. Physics in Medicine & Biology. 2012;58(1):R1.

[55] Murrie R, Stevenson A, Morgan K, Fouras A, Paganin D, Siu K. Feasibility study of propagation-based phase-contrast X-ray lung imaging on the Imaging and Medical beamline at the Australian Synchrotron. Journal of Synchrotron Radiation. 2014;21(2):430–445.

[56] Maxwell JC. III. On physical lines of force. The London, Edinburgh, and Dublin Philosophical Magazine and Journal of Science. 1862;23(151):12–24.

[57] Pelliccia D, Kitchen M, Morgan K. Theory of X-ray Phase Contrast Imaging. In: Handbook of X-ray Imaging: Physics and Technology. CRC Press; 2018. p. 971–997.

[58] Podgoršak EB. Radiation physics for medical physicists, Third Edition. Springer; 2006.

[59] Pacilè S, Baran P, Dullin C, Dimmock M, Lockie D, Missbach-Guntner J, et al. Advantages of breast cancer visualization and characterization using synchrotron radiation phase-contrast tomography. Journal of Synchrotron Radiation. 2018;25(5):1460–1466.

[60] Gureyev T. X-ray complex refraction coefficient; 2021. Accessed: 22/04/2021. http://ts-imaging.science.unimelb.edu.au/Services/Simple/ICUtilXdata.aspx.

[61] Auweter S, Herzen J, Willner M, Grandl S, Scherer K, Bamberg F, et al. X-ray phase-contrast imaging of the breast—advances towards clinical implementation. The British journal of radiology. 2014;87(1034):20130606.

[62] Wilkins S, Gureyev TE, Gao D, Pogany A, Stevenson A. Phase-contrast imaging using polychromatic hard X-rays. Nature. 1996;384(6607):335–338.

[63] Schaff F, Morgan K, Pollock J, Croton L, Hooper S, Kitchen M. Material decomposition using spectral propagation-based phase-contrast x-ray imaging. IEEE Transactions on Medical Imaging. 2020;39(12):3891–3899.

[64] Paganin D, Pelliccia D. Tutorials on X-ray phase contrast imaging: Some fundamentals and some conjectures on future developments. arXiv preprint arXiv:190200364. 2019.

[65] Gureyev T, Mayo S, Myers D, Nesterets Y, Paganin D, Pogany A, et al. Refracting Röntgen's rays: propagation-based x-ray phase contrast for biomedical imaging. Journal of Applied Physics. 2009;105(10):102005.

[66] Pavlov K, Gureyev T, Paganin D, Nesterets Y, Morgan M, Lewis R. Linear systems with slowly varying transfer functions and their application to x-ray phase-contrast imaging. Journal of Physics D: Applied Physics. 2004;37(19):2746.

[67] Teague M. Deterministic phase retrieval: a Green's function solution. JOSA. 1983;73(11):1434–1441.

[68] Diemoz P, Bravin A, Coan P. Theoretical comparison of three X-ray phase-contrast imaging techniques: propagation-based imaging, analyzer-based imaging and grating interferometry. Optics Express. 2012;20(3):2789–2805.

[69] Zuo C, Li J, Sun J, Fan Y, Zhang J, Lu L, et al. Transport of intensity equation: a tutorial. Optics and Lasers in Engineering. 2020:106187.

[70] Bonse U, Hart M. An X-ray interferometer. Applied Physics Letters. 1965;6(8):155–156.

[71] Bonse U, Hart M. An X-ray interferometer with long separated interfering beam paths. Applied Physics Letters. 1965;7(4):99–100.

[72] Momose A, Fukuda J. Phase-contrast radiographs of nonstained rat cerebellar specimen. Medical Physics. 1995;22(4):375–379.

[73] Momose A, Takeda T, Itai Y, Hirano K. Phase–contrast X–ray computed tomography for observing biological soft tissues. Nature Medicine. 1996;2(4):473–475.

[74] Wilkins S, Nesterets YI, Gureyev T, Mayo S, Pogany A, Stevenson A. On the evolution and relative merits of hard X-ray phase-contrast imaging methods. Philosophical Transactions of the Royal Society A: Mathematical, Physical and Engineering Sciences. 2014;372(2010):20130021.

[75] Ida N, Meyendorf N. Handbook of advanced nondestructive evaluation. Springer International Publishing; 2019.

[76] Chapman D, Thomlinson W, Johnston R, Washburn D, Pisano E, Gmür N, et al. Diffraction enhanced x-ray imaging. Physics in Medicine & Biology. 1997;42(11):2015.

[77] Scherer K, Braig E, Ehn S, Schock J, Wolf J, Birnbacher L, et al. Improved diagnostics by assessing the micromorphology of breast calcifications via x-ray dark-field radiography. Scientific Reports. 2016;6(1):1–11.

[78] Arfelli F, Astolfo A, Rigon L, Menk RH. A Gaussian extension for diffraction enhanced imaging. Scientific Reports. 2018;8(1):1–14.

[79] Talbot H. LXXVI. Facts relating to optical science. No. IV. The London, Edinburgh, and Dublin Philosophical Magazine and Journal of Science. 1836;9(56):401–407.

[80] Weitkamp T, Diaz A, David C, Pfeiffer F, Stampanoni M, Cloetens P, et al. X-ray phase imaging with a grating interferometer. Optics Express. 2005;13(16):6296–6304.

[81] Born M, Wolf E. Principles of optics: electromagnetic theory of propagation, interference and diffraction of light. Elsevier; 2013.

[82] Pfeiffer F, Weitkamp T, Bunk O, David C. Phase retrieval and differential phase-contrast imaging with low-brilliance X-ray sources. Nature Physics. 2006;2(4):258–261.

[83] Olivo A, Speller R. Experimental validation of a simple model capable of predicting the phase contrast imaging capabilities of any x-ray imaging system. Physics in Medicine & Biology. 2006;51(12):3015.

[84] O'Connell D, Morgan K, Ruben G, Schaff F, Croton L, Buckley G, et al. Photon-counting, energy-resolving and super-resolution phase contrast X-ray imaging using an integrating detector. Optics Express. 2020;28(5):7080–7094.

[85] MARS Bioimaging - What is Spectral CT?; 2021. Accessed: 23/04/2021. `https://www.marsbioimaging.com/spectral-ct/`.

[86] Nesterets Y, Gureyev T. Noise propagation in x-ray phase-contrast imaging and computed tomography. Journal of Physics D: Applied Physics. 2014;47(10):105402.

[87] Paganin D, Mayo S, Gureyev T, Miller P, Wilkins S. Simultaneous phase and amplitude extraction from a single defocused image of a homogeneous object. Journal of Microscopy. 2002;206(1):33–40.

[88] Kitchen M, Buckley G, Gureyev T, Wallace M, Andres-Thio N, Uesugi K, et al. CT dose reduction factors in the thousands using X-ray phase contrast. Scientific Reports. 2017;7(1):1–9.

[89] Gureyev T, Mayo S, Nesterets Y, Mohammadi S, Lockie D, Menk R, et al. Investigation of the imaging quality of synchrotron-based phase-contrast mammographic tomography. Journal of Physics D: Applied Physics. 2014;47(36):365401.

[90] Pacilè S, Dullin C, Baran P, Tonutti M, Perske C, Fischer U, et al. Free propagation phase-contrast breast CT provides higher image quality than cone-beam breast-CT at low radiation doses: a feasibility study on human mastectomies. Scientific Reports. 2019;9(1):1–7.

[91] Nesterets Y, Gureyev T, Mayo S, Stevenson A, Thompson D, Brown J, et al. A feasibility study of X-ray phase-contrast mammographic tomography at the Imaging and Medical beamline of the Australian Synchrotron. Journal of Synchrotron Radiation. 2015;22(6):1509–1523.

[92] Tapiovaara M. Relationships between physical measurements and user evaluation of image quality in medical radiology–a review. Citeseer; 2006.

[93] ICRU Report 54 Medical Imaging - the assessment of image quality. International Commission on Radiation Units and Measurement; 1996.

[94] Dobbins J. Image quality metrics for digital systems. Handbook of medical imaging. 2000;1:161–222.

[95] Lee J, Nishikawa R, Reiser I, Zuley M, Boone J. Lack of agreement between radiologists: implications for image-based model observers. Journal of Medical Imaging. 2017;4(2):025502.

[96] Tingberg A, Bath M, Hakansson M, Medin J, Sandborg M, Alm-Carlsson G, et al. Comparison of two methods for evaluation of image quality of lumbar spine radiographs. In: Medical Imaging 2004: Image Perception, Observer Performance, and Technology Assessment. vol. 5372. International Society for Optics and Photonics; 2004. p. 251–262.

[97] Taba S, Arhatari B, Nesterets Y, Gadomkar Z, Mayo S, Thompson D, et al. Propagation-based phase-contrast CT of the breast demonstrates higher quality than conventional absorption-based CT even at lower radiation dose. Academic Radiology. 2021;28(1):e20–e26.

[98] Aminzadeh A, Arhatari B, Maksimenko A, Hall C, Hausermann D, Peele A, et al. Imaging breast microcalcifications using dark field signal in propagation-based phase-contrast tomography. In: Applied Sciences. vol. 11; 2021. .

[99] Cowen A, Launders J, Jadav M, Brettle D. Visibility of microcalcifications in computed and screen-film mammography. Physics in Medicine & Biology. 1997;42(8):1533.

[100] Samei E, Flynn M, Reimann D. A method for measuring the presampled MTF of digital radiographic systems using an edge test device. Medical Physics. 1998;25(1):102–113.

[101] Gureyev T, Nesterets Y, Ternovski D, Thompson D, Wilkins S, Stevenson A, et al. Toolbox for advanced X-ray image processing. In: Advances in Computational Methods for X-Ray Optics II. vol. 8141. International Society for Optics and Photonics; 2011. p. 81410B.

[102] Gureyev T, Nesterets Y, De Hoog F, Schmalz G, Mayo S, Mohammadi S, et al. Duality between noise and spatial resolution in linear systems. Optics Express. 2014;22(8):9087–9094.

[103] Gureyev T, Nesterets Y, De Hoog F. Spatial resolution, signal-to-noise and information capacity of linear imaging systems. Optics Express. 2016;24(15):17168–17182.

[104] Yalcin A, Olgar T, Sancak T, Atac GK, Akyar S. Correlation between physical measurements and observer evaluations of image quality in digital chest radiography. Medical Physics. 2020;47(9):3935–3944.

[105] Lin Y, Luo H, Dobbins III JT, Page McAdams H, Wang X, Sehnert WJ, et al. An image-based technique to assess the perceptual quality of clinical chest radiographs. Medical Physics. 2012;39(11):7019–7031.

[106] Samei E, Lin Y, Choudhury KR, Page McAdams H. Automated characterization of perceptual quality of clinical chest radiographs: validation and calibration to observer preference. Medical Physics. 2014;41(11):111918.

[107] Chow L, Rajagopal H. Modified-BRISQUE as no reference image quality assessment for structural MR images. Magnetic Resonance Imaging. 2017;43:74–87.

[108] Buytaert D, Taeymans Y, De Wolf D, Bacher K. Evaluation of a no-reference image quality metric for projection X-ray imaging using a 3D printed patient-specific phantom. Physica Medica. 2021;89:29–40.

[109] Baran P, Pacilè S, Nesterets YI, Mayo S, Dullin C, Dreossi D, et al. Optimization of propagation-based x-ray phase-contrast tomography for breast cancer imaging. Physics in Medicine & Biology. 2017;62(6):2315.

[110] Taba S, Baran P, Lewis S, Heard R, Pacile S, Nesterets Y, et al. Toward improving breast cancer imaging: radiological assessment of propagation-based phase-contrast CT technology. Academic Radiology. 2019;26(6):e79–e89.

[111] Richard Hammerstein G, Miller DW, White DR, Ellen Masterson M, Woodard HQ, Laughlin JS. Absorbed radiation dose in mammography. Radiology. 1979;130(2):485–491.

[112] Gureyev T, Nesterets Y, Kozlov A, Paganin D, Quiney H. On the "unreasonable" effectiveness of transport of intensity imaging and optical deconvolution. JOSA A. 2017;34(12):2251–2260.

[113] Bath M, Mansson L. Visual grading characteristics (VGC) analysis: a non-parametric rank-invariant statistical method for image quality evaluation. The British Journal of Radiology. 2007;80(951):169–176.

[114] Gureyev T, Mohammadi S, Nesterets Y, Dullin C, Tromba G. Accuracy and precision of reconstruction of complex refractive index in near-field single-distance propagation-based phase-contrast tomography. Journal of Applied Physics. 2013;114(14):144906.

[115] Gureyev T; 2021. Personal communication.

[116] Cunningham IA, Shaw R. Signal-to-noise optimization of medical imaging systems. JOSA A. 1999;16(3):621–632.

[117] Fedorov A, Beichel R, Kalpathy-Cramer J, Finet J, Fillion-Robin JC, Pujol S, et al. 3D Slicer as an image computing platform for the Quantitative Imaging Network. Magnetic Resonance Imaging. 2012;30(9):1323–1341.

[118] Gureyev T, Nesterets Y, Stevenson A, Miller P, Pogany A, Wilkins S. Some simple rules for contrast, signal-to-noise and resolution in in-line x-ray phase-contrast imaging. Optics Express. 2008;16(5):3223–3241.

[119] Graphpad Prism, version 9.2.0 for Windows;. Available from: www.graphpad.com.

[120] Graphpad Help: Choosing a normality test; 2022. Accessed: 25/01/2022. https://www.graphpad.com/guides/prism/latest/statistics/stat_choosing_a_normality_test.htm.

[121] D'Agostino R, Pearson ES. Tests for departure from normality. Empirical results for the distributions of $b^2$ and $\sqrt{b}$. Biometrika. 1973;60(3):613–622.

[122] Graphpad Help: Interpreting results: Normality Tests; 2022. Accessed: 18/02/2022. https://www.graphpad.com/guides/prism/latest/statistics/stat_interpreting_results_normality.htm.

[123] Graphpad Help: Interpreting results: Correlation; 2022. Accessed: 25/01/2022. https://www.graphpad.com/guides/prism/latest/statistics/stat_interpreting_results_correlati.htm.

[124] Gureyev T, Kozlov A, Paganin D, Nesterets Y, Quiney H. Noise-resolution uncertainty principle in classical and quantum systems. Scientific Reports. 2020;10(1):1–11.

[125] Dougherty G. Computerized evaluation of mammographic image quality using phantom images. Computerized Medical Imaging and Graphics. 1998;22(5):365–373.

[126] Sandborg M, Tingberg A, Dance D, Lanhede B, Almén A, McVey G, et al. Demonstration of correlations between clinical and physical image quality measures in chest and lumbar spine screen–film radiography. The British Journal of Radiology. 2001;74(882):520–528.

[127] Schindelin J, Arganda-Carreras I, Frise E, Kaynig V, Longair M, Pietzsch T, et al. Fiji: an open-source platform for biological-image analysis. Nature Methods. 2012;9(7):676–682.